UNIVERSITY OF LONDON THESIS

Degree phd Year 2007 Name of Author HERVE BORRION

Study of Processing Techniques for Radar Non-Cooperative Target Recognition

A thesis presented to the University of London
for the degree of Doctor of Philosophy

Hervé Borrion

■ Department of Electronic & Electrical Engineering ■
■ University College London ■ ■ September 2006 ■

ProQuest LLC
789 East Eisenhower Parkway
P.O. Box 1346
Ann Arbor, MI 48106-1346

ABSTRACT

Radar is a powerful tool for detecting and tracking airborne targets such as aircraft and missiles by day and night. Nowadays, it is seen as a genuine solution to the problem of target recognition. Recent events showed that cooperative means of identification such as the IFF transponders carried by most aircraft are not entirely reliable and can be switched off by terrorists. For this reason, it is important that target identification be obtained through measurements and reconnaissance based on non-cooperative techniques.

In practice, recognition is achieved by comparing the electromagnetic signature of a target to a set of others previously collected and stored in a library. Such signatures generally represent the targets reflectivity as a function of space. A common representation is known as one-dimensional high-resolution range-profile (HRRP) and can be described as the projection of the reflectivity along the direction of propagation of the wave. When the measured signature matches a template, the target is identified. The main drawback of this technique is that signatures greatly vary with aspect-angle so that measurements must be made for many angles and in three dimensions. This implies a potentially large cost as large datasets must be created, stored and processed. Besides, any modification of the target structure may yield incorrect classification results.

Instead, other processing techniques exist that rely on recent mathematical algorithms. These techniques can be used to extract target features directly from the radar data. Because of the direct relation with target geometry, these feature-based methods seem to be suitable candidates for reducing the need of large databases. However, their performances and their domains of validity are not known. This is especially true when it comes to real targets for at least three reasons. First, the performance of the methods varies with the signal-to-noise ratio. Second, man-made targets are often more complex than just a set of independent theoretical point-like scatterers. Third, these targets are made up of a large number of scattering elements so that mathematical assumptions are not met. In conclusion, the physical correctness of the computational models are questionable.

This thesis investigates the processing techniques that can be used for non-cooperative target recognition. It demonstrates that the scattering-centre extraction is not suitable for the model-based approach. In contrast, it shows that the technique can be used with the feature-based approach. In particular, it investigates the recognition when achieved directly in the z-domain and proposes a novel algorithm that exploits the information already in the database for identifying the signal features that corresponds to physical scatterers on the target. Experiments involving real targets show that the technique can enhance the classification performance and therefore could be used for non-cooperative target recognition.

ACKNOWLEDGEMENTS

Prior to acknowledging the people directly related to this work, I would like to thank Dr Philippe Guimbal and Pascal Balleyguier from CEA who shared with me their passion for Research, and Dr Florent Christophe from ONERA, who introduced me to the field of radar signal processing during my Master's degree at the Ecole Nationale Supérieure d'Aéronautique et de l'Espace in Toulouse.

The work presented in this thesis has been carried out under an EPSRC[1] CASE award sponsored by former company AMS now divided between BAE Systems Insyte and SELEX.

I would like to express my gratitude to my supervisors, Professor Hugh Griffiths and Professor Christopher Baker from University College London (UK), my industrial partners and advisers Dr Peter Tait and Dr David Money from BAE System Insyte (UK) and Professor Mike Inggs, my host at the University of Cape Town (South Africa).

I am deeply indebted to the people who helped me complete this work by supplying me with radar data including Dr Emanuel Radoi from ENSIETA (France), Professor Victor Chen from the US Naval Research Laboratory (USA), Professor Anthony Gillespie from DSTL (UK), Dr John Chadwick and Dr Craig Parish from QinetiQ Malvern (UK), and Dr Francois Anderson from CSIR (South Africa).

I would like to thank Professor Alfonso Farina from Selex (Italy) and Professor Ralph Benjamin from University College London and University of Bristol (UK) for their advice and their interest in my projet.

I would also like to thank the students and staff of the UCL radar group and UCT radar remote sensing group. Finally, I would like to thank Dr Richard Bullock for his help with my English.

[1]Engineering and Physical Sciences Research Council

Contents

List of Figures

List of Acronyms

AIC	Akaike Information Criterion
AR	Autoregressive
ATR	Automatic Target Recognition
AWGN	Additive White Gaussian Noise
CSIR	Centre for Scientific and Industrial Research
DFT	Discrete Fourier Transform
EM	Electro-Magnetic
ENSIETA	Ecole Nationale Supérieure des Ingénieurs des Etudes et Techniques d'Armement
FPE	Forward Prediction Error
FFT	Fast Fourier Transform
FM	Frequency Modulation
GE	Generalised Eigen-Value
GSM	Global System for Mobile Communications
GPOF	Generalised Pencil of Function
GPS	Global Positioning System
GTD	Geometrical Theory of Diffraction
HRR	High-Resolution Radar
HRRP	High-Resolution Range-Profile
IEE	The Institution of Electrical Engineers
IEEE	The Institute of Electrical and Electronics Engineers
IET	The Institution of Engineering and Technology
IFFT	Inverse Fast Fourier Transform
IFF	Identification Friend or Foe
IQ	In-phase and Quadrature Modulation
ISAR	Inverse Synthetic Aperture Radar
JEM	Jet Engine Modulation
LFM	Linear Frequency Modulation
LP	Linear Prediction
LLS	Linear Least-Squares
MAUCAZ	Matching Algorithm Using Clustering Approach in the Z-plane
MDL	Minimum Description Length
MEM	Maximum Entropy Method

MUSIC	Multiple Signal Classification
NCTR	Non-Cooperative Target Recognition
NLLS	Non-Linear Least-Squares
PO	Physical Optics
PRF	Pulse Repetition Frequency
PRI	Pulse Repetition Interval
PSD	Power Spectral Density
RADAR	Radio Detection and Ranging
RCM	Range Cell Migration
RCS	Radar-Cross-Section
RRCS	Rotational Range Cell Migration
SAR	Synthetic Aperture Radar
SED	Sliding Euclidian Distance
SNR	Signal-to-Noise Ratio
SRR	Signal-to-Residue Ratio
SSR	Secondary Surveillance Radar
SVD	Singular-Value Decomposition
TLS	Total Least-Squares
TRCM	Translational Range Cell Migration
UWB	Ultra-Wide Bandwidth
VHF	Very High Frequency

List of Symbols

$\hat{\bullet}$	Estimated value
$\tilde{\bullet}$	Reference value
α	Damping factor
δ	Dirac function
$\delta\theta$	Aperture (rad)
$\Delta\rho$	Pole magnitude error
$\Delta\theta$	Angular step (rad)
$\Delta\theta_h$	Angle between half-power points (rad)
ΔB	Pulse bandwidth (Hz)
Δf	Frequency step (Hz)
Δr	Range resolution (m)
Δr_c	Cross-range resolution (m)
ΔR	Distance between scatterers (m)
γ	Chirp rate ($Hz.s^{-1}$)
ζ	Output of the correlation filter
η	Initial noise
θ	Aspect-angle (rad)
Θ	Pole angle error (rad)
λ	Wavelength (m)
λ_i	Singular-value associated with the i^{th} scattering centre
ρ	Pole magnitude
σ	Radar-Cross-Section (m^2)
ς	Reflectivity function
Σ	Matrix of Singular-values
Σ_s	Matrix of Singular-values associated with the signal sub-space
Σ_n	Matrix of Singular-values associated with the noise sub-space
τ	Pulse duration (s)
τ_s	Sampling interval (s)
φ	Phase angle (rad)
ϕ	Phase modulation ($rad.s^{-1}$)
$\Phi(t)$	Instantaneous frequency (rad)
ω	Rotation-vector magnitude ($rad.s^{-1}$)
ω_0	Carrier frequency ($rad.s^{-1}$)

a	Pole amplitude
a	Signal enveloppe
$\mathcal{A}$	Forward prediction error polynomial
A	Amplitude
A	Projection matrix
B	Bandwidth (Hz)
B_{eff}	Effective bandwidth (Hz)
c	Speed of light $(m.s^{-1})$
c_1	Frequency domain dampling filter
c_2	Pulse matched filter
c_q	Autoregressive coefficient
$\hat{C}$	Vector containing the autoregressive coefficients
d	Distance of the scatterer to the radar (m)
d_ϵ	Elliptic distance between two poles
d_m	One-way distance between the radar and the m^{th} scatterer
d_z	Z-plane distance between two poles
d_{Ch}	Chebyshev distance between two sets of poles
d_{CB}	City-block distance between two sets of poles
d_E	Euclidian distance between two poles
d_{Eu}	Euclidian distance between two sets of poles
d_S	Surface element $(m.^2)$
D	Target dimension (m)
D_A	Principal length of the antenna (m)
D_{Ch}	Distance between two sets of poles
D_T	Principal length of the target (m)
e	Residue
E_i	Incident EM field $(V.m^{-1})$
E_s	Scatterered EM field $(V.m^{-1})$
f	Frequency (Hz)
f_0	Initial frequency (Hz)
f_c	Central frequency (Hz)
f_n	Frequency at index n (Hz)
f_D	Doppler frequency (Hz)
G	Green's function
H	Hankel matrix
H	Magnetic field $(A.m^{-1})$
H_{go}	Magnetic field based on Geometrical Optics $(A.m^{-1})$
H_{inc}	Magnetic field incident to the target $(A.m^{-1})$
H_{po}	Magnetic field based on Physical Optics $(A.m^{-1})$
H_{scatt}	Magnetic field scattered by the target $(A.m^{-1})$
I	Identity matrix
$\mathcal{J}$	Induced current density $(A.m^{-2})$

k	Wavenumber $(rad.m^{-1})$
K	Number of clusters employed for MAUCAZ
L	Hankel matrix width
M	Model order
M	Number of poles selected in the test pattern
M'	Number of poles selected in the template pattern
$M(n)$	Model
n	Frequency index
$\hat{n}$	Surface vector
N	Number of samples
N'	Number of samples after model prediction
N_{arr}	Number of arrangements of pole-cluster
N_{comb}	Number of combinations of pole-cluster
p	Pole
P	Number of point-scatterers
P	Number of poles per pattern for MAUCAZ
$\mathcal{P}$	Power spectrum
r_m	Range of the m^{th} scatterer relative to R_0 (m)
R	Range of the target (m)
R_0	Starting range of the imaged window (m)
R_m	Cross-correlation function
R_{ss}	Autocorrelation matrix of the signal
$R_{unambiguous}$	Length of the unambiguous range window (m)
R_{uu}	Autocorrelation matrix of the noise
R_{xx}	Autocorrelation matrix of the corrupted signal
s	Deterministic signal
s_b	Baseband signal
S	Fourier transform of s
t	Time (s)
t_m	Propagation time associated with the m^{th} scatterer(s)
T	Signal duration (s)
$\mathcal{T}$	Translation operator
u	Noise
$\vec{u}$	Column of the left singular matrix
U	Left singular matrix
$\vec{v}$	Column of the right singular matrix
v_m	Speed of the m^{th} scatterer $(m.s^{-1})$
V	Right singular matrix
w_m	Output of the mixer
w_r	Received waveform
w_t	Transmitted waveform
x	Received signal
$\vec{x}$	Unit vector
$\vec{x}$	Space vector
$\hat{X}$	Ouput vector of the autoregressive process
$\vec{y}$	Unit vector
z	Pole

Chapter 1

INTRODUCTION

1.1 Background

1.1.1 Foreword

Throughout this Chapter, the reader will be progressively introduced to a scientific problem that continues to animate a large part of the radar community, that is the capability to remotely determine the physical properties of a system, such as an aircraft, and classify it as such. Starting with the basic principle used by radar sensors for detecting targets, the chapter progresses towards the more complex use of radar systems for achieving target-recognition. Based on early and more recent research, this chapter introduces the problem of interest and the subject of this thesis.

1.1.2 Radar for remote sensing

To start with, let us consider that a system is defined by a set of unique elements that can be observed, described, classified, distinguished and ultimately identified through their properties. Applied Physics is regarded as a branch of the Sciences that attempts to estimate these properties with the highest accuracy permitted by the instrumentation. The properties of a system are estimated through physical quantities that can be described in various dimensions, usually the four-dimensional space-time first postulated by the Lithuanian mathematician Hermann Minkowski. Engineers are very familiar with physical quantities such as temperature, pressure, volume and, in the case of radar engineers, with reflectivity. When their values are not known *a priori*, they are determined by measurements using sensors. The association of accurate estimates and a good knowledge of the physical laws that describe the relations between physical variables is essential to accurately estimate the system properties.

The inverse problem is a classic subject in topics involving objects that are located at great distance from the observer. For these situations where an observer cannot directly get the information about a designated object, remote sensors can be used, for example, to measure the radiation emitted by the object. Different sensors apply to different types of radiation. Such systems can be found in an increasing number of modern applications including aircraft-tracking for air traffic control, speed estimation for law enforcement, cloud and rain density imaging for atmospheric physics, ice-interferometry for environmental studies, plankton density imaging for geo-resources management and ground mapping for military intelligence and many others. It is worth noticing that all these applications can be treated with instruments measuring the energy of the electromagnetic field in the microwave band although it is not a wholly complete analysis by measurement.

Since the French scientist Pierre David successfully detected an aircraft in 1934, all sorts of radar systems have demonstrated their suitability for both military and civil needs. They are relatively non-invasive sensors that can operate remotely with any weather in night and day conditions and over wide regions. These characteristics make radar a high-performance sensor for detecting and locating long-range passive targets even through clouds and rain. Modern coherent radars offer the ability to partially shape the transmitted electromagnetic field in space, time, frequency and polarisation. By enlarging the information content of the measurement, this capability is used to estimate the solution of the inverse problem. Here it is the characterisation of the target reflectivity in space. One hundred years of evolution of techniques and technology have enabled finer and more accurate estimation but, interestingly, the resulting solution still remains expressed as an image of the surface reflectivity in several dimensions.

1.1.3 Early radars

In 1865, the Scottish physicist James Maxwell developed the theory of Electromagnetism. Twenty-four years later, the German Heinrich Hertz demonstrated experimentally that electrically conducting surfaces reflect electromagnetic waves. These were fundamental milestones for the invention of radar. However, the history of RAdio Detecting And Ranging (RADAR) [48] began really in 1900 when the Serbian-American engineer Nikola Tesla mentioned the possibility of employing radio-waves for measuring the movement of distant objects. In 1904, another German named Christian Hülsmeyer transformed these words into a transmitter-receiver system for remotely detecting ships. He named it a "telemobiloscope". The patent for this anti-collision device credits Hülsmeyer as the inventor of radar. Although demonstrations were made publicly, the military potential of this device was not realised until the First World War. At that time,

a third German named Richard Scherl proposed to build a system based on electromagnetic waves to detect enemy targets in darkness. Until then, the techniques for detecting aircraft included visual sighting and a binaural sensitive sound locator initially used by the French and known as the "Claude Orthophone". Later improvements enabled this passive acoustic aircraft-detector to have an accuracy of two degrees in azimuth. These were rudimentary techniques with a poor maximum range of detection.

During and after the First World War, an increasing interest was shown for detection systems in the USA. Dr Albert Hoyt Taylor and his assistant Leo Clifford Young discovered during VHF propagation experiments that radio beams could be used for the radio detection of enemy vessels passing between two destroyers. In Germany, Hans Dominik followed Scherl's recommendations and started experiments in 1916 with a 10 cm wavelength apparatus that he built at Siemens and Halske. Despite slow progress and poor interest, radar systems were not only left to the imagination of science-fiction authors like Hugo Gernsback [15]. The strategic importance of airplanes in the First World War rapidly convinced many nations to investigate new technologies for aircraft detection. The principal systems that were not acoustic-based relied on the detection of electromagnetic waves of either infra-red radiation generated by the aircraft engine or radio-waves generated by the ignition system. Radar research was also subsequently allocated large budgets for this purpose in the 1930s. Innovations followed and the summer of 1934 saw the first successful tests happening in France in July and Russia in August. Success in Germany, Great Britain, USA, Japan, the Netherlands, Italy and Hungary followed quickly after. By the beginning of the Second World War, radar systems were manufactured by many nations.

From a military perspective one considers that the earlier the detection of the enemy, the greater the advantage. For this reason, radars were soon associated with aviation. During the war, most radars were designed to detect and track aircraft. For this task, a radar must have short-wavelength and high-power. However, meeting both requirements was a real technological challenge. The vacuum-tube technology used in the early radars could not transmit the power needed in the micro-wave band. Many nations worked on different alternatives to the existing system. Various versions of the cavity magnetron had been developed but history mainly remembers the designs of the British pair Randall and Boot who made possible the construction of the cavity-magnetron which, in April 1940, could generate a peak-power value of $500W$. This device, which was inspired by the work of Prof Albert Hull, is not an amplifier but a high-power valve oscillator itself. It was a decisive step for producing focused beams and enabling tracking of targets at long range.

For many applications including air traffic control, the radar performance is partly associated with the maximum range at which a target can be detected. The maximum range is limited by several factors including the power transmitted and the losses due to radar equipment, target's reflectivity and medium of propagation. Based on the simple expression of the radar range equation, research teams concentrated their effort on the design of a device which can transmit high-power micro-waves. Winning this technological challenge has been essential to the development of modern radars. The successful design of the magnetron enabled long range detection but the discrimination of targets that were closely spaced remained a major problem. Similarly, fine description of the target was not made possible by these early systems.

1.1.4 Radar resolution

A problem quickly faced by radar-engineers was spatial resolution of targets. Radar spatial-resolution is often described as the minimum separation between two objects that can be discriminated. Established by the English physicist John Strutt, third Baron Rayleigh, in the 19^{th} century, the Rayleigh Criterion specifies this distance so that the intersection of the returns from two identical point-scatterers is 9 dB below their maximum value. High-resolution radar systems have thus the ability to distinguish between closely spaced targets. Such resolution enables detailed information to be exploited for many applications including target imaging and non-cooperative target recognition (NCTR). However, it is important to understand that in order to achieve what radar operators call "target resolution", one needs to achieve the resolution of peaks of the probability density function of the reflectivity expressed in a given space. Distinguishing between these very close definitions may require extremely high resolution. For the latter, the resolution can vary rapidly with the space chosen to image the reflectivity. For high-resolution imaging, these differences cannot be neglected.

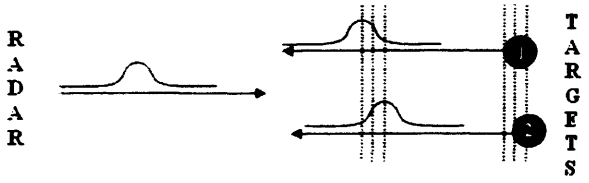

Figure 1.1: Pulse reflected by two point-scatterers located at different distances to the radar

The separation of targets illuminated by a radar depends upon the ability to isolate their returns. Figure 1.1 represents the radar returns of two closely

spaced targets. Due to the two-way propagation of the transmitted field, the separation between the returns corresponds to twice the separation between the targets. Figure 1.2 represents the pulses received by the radar when the separation between targets is as described by the Rayleigh criterion.

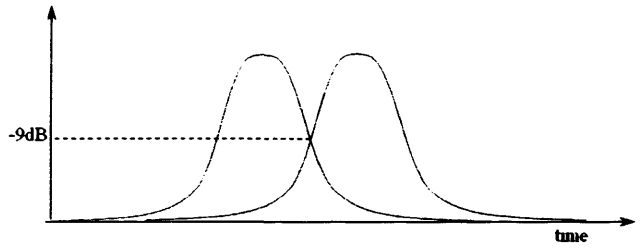

Figure 1.2: Rayleigh criterion: limit of resolution for two point-scatterers

High-resolution radar systems conventionally transmit electromagnetic waves characterised by small duration and small beam-width. Small beamwidth creates high azimuth-resolution but requires high frequencies and large apertures. However, when the targets are aligned with the radar, they lie within the same beam. In this case, the return must be isolated in time. The transmission of short-pulses allows target separation through separation of the returns. Basically, a target illuminated by a radar pulse typically produces an echo. For two targets aligned with the radar, the two returns may overlap if the distance between them is not large enough with respect to the transmitted pulse-width. For this reason, the first solution to improve the range resolution had been to transmit pulses with small time extent, equivalently large bandwidth. Equation 1.1 describes the relation between bandwidth (B) and nominal range-resolution Δr for a simple pulse.

$$\Delta r = \frac{c}{2B} \tag{1.1}$$

where c is the speed of light in the medium of propagation.

At this stage, it is important to understand how high-resolution can enhance the performance of a radar. For this, let us consider the main applications of interest: detection, characterisation and classification of targets.

- Detection of targets in a given spatial region is achieved by observing a variation of reflectivity through time as it traduces the target entering into the region. Independent targets that are closely spaced may appear like a single one if the resolution is not good enough. For instance, a Doppler radar with virtually no range resolution would not be able to distinguish between two targets aligned with the radar and

flying at the same speed. This example shows that decisions based on low-resolution images may have disastrous consequences *e.g.* in the case of air traffic control or military radars. Improving the resolution enables the peaks of reflectivity to be narrowed down to a time-width which potentially yields detection of individual targets. Resolving targets in space does not necessarily require expressing the reflectivity in space though.

- Characterization of a scene in space is in general achieved by imaging the probability density function of the material reflectivity in space. High-resolution representations of the target reflectivity in space can enable differentiation of contributing scatterers to be made on a sub-target scale by revealing fine details on its surface, similar to an photograph, *i.e.* the target is resolved into multiple scatterers. For most applications of interest here, this representation is expected to provide enough information and in a form that is easily exploitable by humans. However, imaging accurately the reflectivity in the spatial domain implies using a correct time-to-space imaging operator, which may be very difficult to implement in practice. For instance, complex scattering effects similar to optical effects may cause ambiguous functions to be incorrectly projected from time to an N-dimensional space. The result is an unfocussed image of the target reflectivity and presence of artefacts. In practice, a radar-image is the representation of the probability function of the reflectivity of a target projected on a space that is directly characterised by the scattering model used. The accuracy of the imaging technique in space is thus directly limited by the ability to solve the inverse problem itself. This makes imaging techniques very difficult to improve in practice.

- Classification can be seen as the division of measurements into subsets. The criteria leading to groups of targets sharing structural features are used to infer structural features of unknown targets from their signatures. For instance, one-dimensional representations of the target reflectivity, known as high-resolution range-profiles can be used to classify targets. Signatures exhibiting similar range-extents could be generated by targets showing similar length. In a similar way the distribution of the energy on range profiles traduces the spatial distribution of the reflectivity. This fact is also exploited to classify targets. However, in both cases the classification is obviously highly dependent upon the target aspect-angle. Depending on the class size, an unknown target would be characterised with greater or lesser precision. The assignation of a signature to a class that has one element only is called recognition. Although classification is not directly used to locate targets, the two problems are closely connected. Considering

that the reflectivity density function can be accurately extracted in any space, high-resolution can create the level of information needed to improve classification. Classification techniques could thus exploit discriminatory information to achieve target recognition. On the other hand, highly-detailed signatures exhibiting artefacts could yield mis-recognition.

Figure 1.3: M47 tanks - comparison of radar images for 1 m, 1 ft, 4 $inch$ resolutions, from Sandia National Laboratories [1].

Fig 1.3 presents images of the same scene for different resolutions[1]. Tanks can be recognised on the 4-inch resolution image (right) mainly because the gun-barrels pointing sideways can be distinguished. This illustrates the idea that recognition has reliance on resolution.

1.1.5 High range resolution radar

Since the early radars, high range-resolution has been synonymous with large bandwidth. The problem has been mainly tackled by creating hardware and waveforms that enable transmission and reception of such signals. The spark transmitter, an oscillatory circuit connected to a resistance (i.e. spark-gap) is probably the first element that enabled ultra-wide band (UWB) communication. Such devices have been realised by Sir John Flemming at University College London for Guglielmo Marconi at the beginning of the twentieth century. Abandoned by the radio-community because of the broad-band interferences that were generated during the discharge, UWB technology was reconsidered in the 1960s when Ross [43] successfully attempted to characterise linear time-invariant systems by their impulse-responses.

Directly benefiting from the development of UWB technology, radar range-resolution improved significantly making possible the separation of target-components in the 1970s. For radar systems, the idea of transmitting very

[1]Resolution are for original pictures prior to downsampling for www viewing

large bandwidths for achieving high range-resolution is attractive. However, the implementation of such systems was not straightforward. Initially, simple pulses of small duration were used to achieve the desired bandwidth. However, the short pulse duration directly affected the signal-to-noise ratio. Later pulse-compression was invented. This method creates a signal with high bandwidth by modulating a pulse. Large bandwidths are achieved with relatively long pulses in this case. Other waveforms known as step-frequency waveforms can be used. They consist in artificially synthesising a bandwidth by coherently processing narrow-band pulses whose central frequency is linearly shifted. Coherent radars are now widely used. These radar systems exploit the phase and amplitude of the received and transmitted signals. Their comparison reveals information related to a target's reflectivity including strength and distance to the radar.

Enlarging the bandwidth enables the signal to support more information. In order to extract this information, several techniques can be used. They depend upon the transmitted waveform and include the Inverse Fourier Transform, cross-correlation, and some rather complicated techniques which rely on *a priori* knowledge. Basically, these techniques assume that the wave-path is direct. They consider thus that the time between the transmission and the reception of echoes is directly proportional to the radar-target distance. Through comparison of the phases, the received signal provides useful information that can be used for estimating the range to the target. These techniques are presented in more detail in Chapter 2.

High-resolution techniques in general are employed to produce images of the scene reflectivity. For this, the measured signal is often decomposed using a basis of elementary signals that are directly related to variables of time and indirectly to variables of space. For instance, range-imaging is a description of the target reflectivity using functions that can be described as a function of time-delay or equivalently range. The well known Fourier Transform relies on a series of complex exponentials to decompose the signal into an orthogonal basis of elementary signals where each Fourier value relates to the reflectivity of the target at a given range-cell in space. The image obtained provides a visual estimation of the power attributed to each elementary signal. Although the Fourier Transform is a robust method, it suffers from poor resolution due to the limited extent of the bandwidth and to high side-lobes masking returns from other targets.

As seen in figure 1.3, radar images may enable visual recognition to be done similarly to optical images. They show the reflectivity of the target surface in one or more dimensions. In order to express this image in space, it is assumed that the target is composed of independent point-scatterers. It

follows that images can only be the spatial representations of the reflectivity of targets composed by non-interacting scatterers whose impulse responses are described by the point-scatterer model. For most targets this assumption is obviously incorrect, and therefore high-resolution images should be regarded as approximations modified by artefacts.

1.1.6 Current issues

There are several issues that must be addressed in order to achieve high-resolution images. Large bandwidths and small beamwidths are basic requirements but the overall performance depends also upon the processing techniques. The principal limitations are due to both technical and theoretical reasons. First the wide-band radar signals are threatened by interferences from an increasing number of communication devices and by new regulations regarding the allocation of the electromagnetic spectrum. Second, the level of resolution obtained now makes images very sensitive to incorrect assumptions or approximations. The conventional theory was suitable for the early radars; now it causes obvious artefacts on images. Amongst these approximations lies the foundation of most modern radar processing techniques: the point-scatterer model, which is described in the following chapter.

The increasing presence of communication devices in the bands where radars operate is a major source of electromagnetic interferences. Since the 1990s, wireless technology such as cellular telephony, messaging and wireless local area networks invaded people's lives. It is not rare to see individuals with virtually no technical knowledge using terms such as GPS, GSM, 3G, Wi-Fi and Bluetooth. Most of the recent communication technologies spread low power signals thinly over a wide range of frequencies. They are said to be "ultra-wide band". However, it is only recently that a unique and definitive definition for these words have been given. The FCC and the International Telecommunication Union - Radiocommunication Sector and the Federal Communication Commission agree define the UWB in terms of transmission from an antenna for which the emitted signal bandwidth exceeds the lesser of 500 MHz or 20% of the centre frequency. In the band $3.1 - 10.6\ GHz$, high range-resolution radars can interfere with such digital communication systems. Similarly, radars can suffer from other UWB devices including other radars operating on adjacent bands.

In order to allow co-existence of the existing users and to accommodate new ones, the philosophy adopted worldwide calls for an optimisation of the allocation scheme. The reallocation of the spectrum occurs at the time of progressive liberalisation of the spectrum, making the reallocation of new customers a political priority driven by strong economic interests. For this reason, the modification is expected to affect the electromagnetic spectrum

currently allocated to remote sensing devices. It is therefore necessary to create processing techniques that are both efficient and flexible in terms of bandwidth requirements. In 2004, the British regulator Ofcom released a report concerning the "study of techniques for improving radar spectrum utilisation" [3]. The report recommends that three technologies, rapidly tunable filters, ultra-narrow band radar and waveform design, have the potential to reduce the current occupied band. The following can be found in the conclusion: "ultra narrow band solution has the greatest potential to improve spectrum utilisation in the long term. However, it is an immature technology therefore further investigation is recommended to help understand the advantages and constraints of this solution". In this context, this thesis presents a study of techniques for achieving high-resolution images and high-performance classification from narrow-band waveforms.

Bandwidths have reached an ultra-wide scale and their extension is no longer an option. In addition, the crowded electromagnetic spectrum calls for a reduction of the current bandwidth used. Nevertheless, increasing the bandwidth extent is not the only option for improving the range-resolution. Processing techniques have to be taken into account too. High-resolution images show that the approximations used to retrieve the information have become the main source of limitation of resolution. Images suffer from defocussing, shadowing and artefact problems. The techniques used to correct these problems have shown some encouraging results for simple targets but remain inadequate for dealing with complex man-made targets.

Methods for improving the effective resolution have been through tackling the problem in various ways including compensation of noise, clutter or motion. They utilise assumptions that are not entirely realistic though. First, most are based on the assumption that the wave-path between a scatterer and the radar antenna is direct. This does not suit the targets characterised by various interacting scatterers creating multi-path or shadowing. Second, these techniques are based on the impulse-response of point scatterers. Variability related to radiation pattern, interaction between scatterers and complex scattering mechanism makes them extremely sensitive to aspect-angle. Multi-path, surface-waves and resonances can not be neglected without significantly affecting the quality of high-resolution images. Third, the use of ultra-wide band brings the idea that close scatterers could be resolved. When applying this to a continuous structure such as an aircraft, the definition of the scatterers is somehow left to engineers. It appears that improving the resolution would imply searching for scatterers with impulse-responses defined *a priori*. Clearly this may not always be the case.

Methods based on *a priori* knowledge of the scattering filter impulse-response produces interesting results but they remain theoretical achievements since this function is in general unknown. Testing all possible values should not be considered as a practical option. One could consider utilising a set of tuned filters, each corresponding to the generic impulse response of a given type of scatterer (*e.g.* cone, plate, trihedral, etc). As the set of basic geometry is finite, so is the set of generic impulse-responses. The matched-filters could be regarded as a tuned version of generic matched-filters associated with generic geometries. The resolution would depend on the ability to estimate an accurate set of generic matched-filters and to individually tune each of them. Any information improving the models would certainly improve the resolution. In practice, the correct set of filters would certainly be an association of filters associated with sub-targets themselves, compounds of sub-targets and probably correcting terms. However, the non-orthogonality of the individual filters makes the problem relatively complex.

In summary, the background of this study starts with a simple fact: the need for high-quality images and useful information has increased the requirements imposed on current radar systems and processing techniques. The traditional bandwidth enlargement is no longer the favoured option for enhancing range-resolution. First, increasing the bandwidth reveals the error of approximations through image-artefacts. Such images are difficult to compensate and the overall information may not be exploitable. Second, methods that can create such enhanced information must be designed to suit tomorrow's spectrum allocation scheme, that is, by using smaller bandwidths. It is not surprising that achieving high-resolution images under such conditions continues to drive a large part of research in radar. Based on the latest research publications, it appears that resolution enhancement should be attacked through creating processing techniques rather than transmitting larger bandwidths. Methods have been proposed for processing radar signals by Gabriel [14], Cuomo *et al.* [12], Moore *et al.* [32] and by Suwa *et al.* [47]. This document contributes to this research stream by offering a critical analysis of the modelling techniques designed to resolve closely-spaced components of man-made targets from narrow-band radar signals.

1.2 Thesis

1.2.1 Problem addressed

Aircraft flying above a certain altitude are required to be equipped with an electronic transponder whose mission is to report altitude and to provide its identity to civilian or military air traffic control. This system, initially called Identification Friend or Foe (IFF) is known also now as Secondary Surveillance Radar (SSR). It is a key element to determine the intent of an aircraft. Although such cooperative systems provide accurate information, one should not rely exclusively on them as serious problems may arise when they are switched off or malfunction. Non-operating IFF systems have been the source of several mistakes during the last decades. For example, a British aircraft was shot down by a US PAC-2 Patriot Missile in Iraq in 2003. The investigation report concluded that the fighter was mistaken for an enemy aircraft after a failure of the IFF systems. Similar events have highlighted the need for alternatives to cooperative systems of identification.

In many nations, budgets for research on non-cooperative target recognition have subsequently risen and scientists have now been looking at this problem from different angles. Radar appears as a unique sensor that could provide valuable information for achieving automatic target recognition in any conditions. The direction taken globally is focussed on using powerful processing tools for identifying aircraft based on some kind of *a priori* knowledge. Radar measurements can provide an image of the reflectivity of a target. Because such signatures depend upon the target structure, an unknown target can be identified by comparing its signature with templates previously generated and stored in a database. Behind the expression "non-cooperative target recognition" is the idea that targets that are non actively participating could be identified. This implies that both the techniques for producing the signature and the classification techniques must be able to perform in spite of these constraints.

Recognition implies that some information be extracted from measurements and compared with other sources of information. In practice, a radar would measure the electromagnetic signature of an unknown aircraft and compare it with templates in library. Amongst the techniques used for classification of air-targets are Jet-Engine Modulation (JEM), one-dimensional range profile, Synthetic Aperture Radar (SAR) images and Inverse Synthetic Aperture Radar (ISAR) images, and tomographic images.

- Jet Engine Modulation exploits the temporal variation of the radiation coming from the rotating parts of a target. They can be propellers, helicopter blades or compressor blades located inside a jet-engine. The

technique is now mature but the performance does depend upon the target orientation. For a jet-aircraft, the technique relies on the fact that the inside structures of the engines are visible. Depending on the aircraft trajectory, this may not be true. Moreover, it can be difficult to classify aircraft whose rotors have different frequencies of rotation.

- One dimensional range profiles are often described as the projection of the target reflectivity on the line of sight. They can be obtained with a single high-resolution radar and they only require limited time on target. These images are thus very easy to generate but the projection of the scatterers' reflectivity on a single axis inevitably yields no cross-range resolution. As a general rule, the amount of information that can be exploited increases with the dimensions of the images. One-dimensional range profiles may not provide enough information for discriminating between targets that have very similar reflectivity in range unless the resolution is high.

- Inverse Synthetic Aperture Radar images are two-dimensional images of the target reflectivity. The techniques used exploit the Doppler effect associated with the target rotation to distribute the energy in the cross-range direction. Despite removing some ambiguities, these techniques are not ideal for NCTR. First they require a long time on target. Second they can only perform with rotating targets so that a typical enemy target flying towards the radar cannot be imaged in two dimensions. Third, imaging requires various pre-processing including motion-compensation. Because the accuracy of the results depends upon the assumptions related to the target-motion and interdependencies which exist between scatterers, the quality of the images is variable. For all these reasons, analysing ISAR images is not trivial and their exploitation for NCTR may not be straightforward.

- Tomographic images such as those used for medical imaging are two-dimensional images reconstructed from successive projections of one-dimensional range profiles measured for various aspect-angles. These images have the potential for NCTR but they can be very difficult to create since the position of the centre of rotation must be estimated. Similar to a magnetic-resonance-imaging scanner, a radar network can be used to illuminate non-rotating targets but a multi-static system is demanding in terms of implementation.

The type of signature to be exploited is important for NCTR. Its choice should be driven by the amount of information that can be exploited as well as operational constraints. The one-dimensional radar image known as range-profile appears as a very promising support of information. It fits the

idea of fully non-cooperative systems as it can be obtained without significant constraints on the target motion. In addition, its small size makes it a cost-efficient solution in terms of processing and storage. It is important for achieving accurate classification that the support of information be simple to avoid large computation times. Because a range profile is obtained from very little processing, it is also less sensitive to incorrect assumptions and approximations than a multi-dimensional image. The main drawback is the relatively small information content that could be directly exploited for NCTR. By comparison, it provides less information than a two-dimensional image of similar resolution.

In order to increase the amount of discriminating information provided by range profiles, it is proposed to enhance the range-resolution, in other words to improve the ability of the radar to distinguish between scatterers that are distributed in the direction of propagation. The enhanced level of description could enable accurate recognition to be achieved by separating scatterers. When it comes to distinguishing between the elements of an aircraft, a sub-meter resolution is needed which requires transmission of wide-band signals. For instance, resolving scatterers that are separated by 20 cm in range would require a bandwidth on the order of 1 GHz.

Technology and waveforms have been continuously enhanced and resolution subsequently progressed according to the relation between bandwidth and range-resolution. However, improving the range-resolution is not straightforward anymore:

- The increasing presence of wireless communication devices in the bands where radars operate is a growing threat on wide-band radar signals. Interferences from others devices and new regulations are likely to reduce the effective bandwidth that can be used for radar imaging. It is therefore important that new imaging techniques fit within the scheme of spectrum allocation. That could imply using bandwidths that are not contiguous in time or frequency.

- For low-resolution and high-frequency waveforms, the impulse-response of the scatterers are approximated by a point-like function. This approximation is not suitable when the size of the components or their inter-spacing distances are on the order of the wavelength or the resolution cell. Increasing the bandwidth and conserving the same scattering model of point-scatterers for scatterers with different characteristics is obviously another major source of limitation. The radar theory based on point-like impulse responses may not be the most appropriate one for dealing with such scatterers.

Signal and image processing have been receiving extensive attention from researchers in astronomy, geophysics, medical imaging and military applications. The introduction of ***a priori*** information in the processing techniques enabled the resolution to be improved beyond the Rayleigh limit. Such techniques includes Prony, Multiple Signal Classification (MUSIC), root-MUSIC, Matrix Pencil, Esprit. A description of these methods would not be very appropriate here but it is worth saying that several decades of research in these fields has yielded a large body of literature which can be effectively exploited for improving the spatial resolution of range profiles.

There exists an important issue that arises from the enhancement of the range-resolution. Because the improved signature provides a finer description, it also becomes more sensitive to target motion and aspect-angle. When the target is translating, migration of scatterers in range must be taken into account. Similarly, the angle at which the target is seen by the radar is a great source of variability. A target rotation of one degree generally yields a very different signature. For this reason, creating translation and rotation invariant techniques are essential. To do so, one must take into account that measuring, storing and comparing signatures has a cost. For operational purposes, it is important that the size of the database gathering the signatures remains small. It follows that a recognition technique based on the signatures from perspectives covering 360 degrees at very close angular intervals is not an attractive solution. In contrast it is desired that only a few templates could enable target recognition from all aspect-angles. Ultimately, it must be considered that range profiles may not be available for building a library. For instance, signatures of enemy-aircraft or aircraft that have payload attached to the external structure are often unavailable. In this case, it is desired to rely on the backscattering from the parts of the aircraft that are consistent in time.

In order to reduce the cost inherent in the variability of the signature, engineers have been looking at techniques exploiting features rather than comparing the signatures directly. In the last few years, research on NCTR has explored various solutions. They achieve size-reduction by using discrete scattering-models, signature prediction by using electromagnetic prediction codes [16] and 3D-reconstructions of the positions of the principal scatterers by tracking their position over a given period [31]. A common idea characterises these techniques: the use of ***a priori*** knowledge enables selected information to be used by cost-efficient classification techniques for accurately achieving target recognition but the technique would need to be studied further before conclusions could be really drawn.

Hence, the general problem posed can be summarised as follow. Is it possible to create a technique that relies on radar range-profiles with improved resolution to achieve accurate target-recognition with limited bandwidth? If the answer is positive, such a system could then constitute an alternative to current IFF systems that are subject to malfunctions, interference and hijacking. In order to fit regulations and operational constraints, it must meet the following requirements:

- dedicated to aircraft-recognition
- fully based on non-cooperative methods
- low-sensitivity to aspect-angle
- accurate discrimination between similar targets
- no reliance on wide-band signals
- low cost
- first step towards recognition based on schematics

The direction taken in this work is motivated by the idea that enhanced resolution yields improved information that can be exploited for radar imaging and non-cooperative target recognition. However achieving high range-resolution without using wide-band signals is not straightforward. In order to compensate for the reduction of the support of information, the approach chosen introduces *a priori* knowledge in the form of a scattering model. It is assumed that a generic model describing the principal scattering mechanisms happening on an aircraft could approximate the backscattered signal. Based on this, the problem consists of extracting the model-parameters from measured narrow-band waveforms. For this, one needs processing techniques that can employ measurements that may not be contiguous in time, frequency or space. This approach which does not require transmission of wide bandwidths is supported by the 2004-report of Ofcom related to bandwidth optimisation: "radars using ultra-narrow band waveforms would have a great potential for reducing spectrum utilisation in the long term".

In 1997, an article entitled "ultra-wide-band coherent processing of sparse subbands" [12] was published in the Lincoln Laboratory Journal, MIT. The authors give a detailed description of a technique that is used to interpolate radar signals that are sparsely distributed in frequency. Using simulated and real targets, the authors show that it is possible to predict the spectrum of the radar signal for one sub-band, by using the information contained in another one. This enables them to artificially build a continuous wide-bandwidth that can be used to enhance the range-profiles and resolve

more scatterers than with traditional techniques. The article concludes by listing elements that would require further investigation in order to determine the limits of the method. On the basis of the results presented, this technique would be suitable for building the high-resolution range profiles needed for achieving non-cooperative target recognition. However, there are many issues that need to be assessed before drawing any conclusion.

The idea of high resolution achieved with narrow-band signals is somehow opposite to signal theory. Here the usual rule is modified by the introduction of *a priori* information. The potential of such a method in terms of applications as well as the unconventional nature of the principle used should have triggered similar research from other scientists throughout the world. Despite presenting the algorithm in detail and showing very promising results, this article has actually inspired very few publications. It appears that the authors themselves did not publish any additional results and several attempts to obtain more information from the Lincoln Laboratory have been unsuccessful. The excellent results presented in the article invite the following question: how well can the information carried by a simple scattering model replace those contained in a signal over several GigaHertz of bandwidth?

1.2.2 Approach

The approach chosen for investigating the potential of the scattering model for building high-resolution range-profiles from narrow-band signals that could be used for non-cooperative target recognition is directly inspired by the article mentioned above. The processing technique is implemented and tested by comparing the results obtained with simulated signals similar to that used in the article. As the results are similarly good, the processing technique is then applied to a signal backscatterered by a real and more complex target. The dataset supplied by an independent source (Dr Victor Chen - Naval Research Laboratory - USA) allows us to demonstrate the potential of this algorithm for radar imaging a real Boeing-727 aircraft. The model obtained is accurate accross the modelling band but attempts to predict the radar signal across a missing band fail. This suggests that the estimated model is not a physically accurate representation of the scattering mechanisms that characterise this aircraft in the missing band. More generally, because of the assumed continuity of the scattering process in frequency, this result constitutes a basis for challenging the capability of the algorithm to perform with complex targets.

In order to identify the source of this error and to determine its cause, joint analysis on simple targets are carried out with both simulated and real signals. To reduce the complexity of analysing results obtained with signals

from moving complex targets in open space, new experiments are performed in a highly controlled environment. For such analysis, one considers the factors related to the target, the signal transmitted and the method. They are in high number in the case of a complex moving target. By using simple targets, the number of varying parameters is reduced to those needed for the sake of the analysis. This approach enables the conclusion to be drawn regardless of the quality of motion-compensation, presence of clutter, interfering sources or other sources of corruption of the signals.

First, a sensitivity analysis is conducted and the model parameter for which the extrapolation is most sensitive is identified. Second, a series of tests enable the factor causing incorrect estimation of the model-parameters to be determined. It is shown that the deficiency of the model imposed by the complexity of the target and the relatively poor quality of the received signal is responsible for incorrect modelling that makes the prediction of the spectrum highly inaccurate. This forms the hypothesis explaining the poor results obtained with the Boeing 727. Once the analysis is completed and the thesis supported by the various experimental results, the case of the Boeing 727 initially studied is reviewed to verify the validity of the thesis. The study is then completed by comparing classification results obtained with signals from real scaled aircraft and their extrapolated versions. Finally, a new classification technique is proposed. It is designed to be less sensitive to the parameters that are considered to be the cause of modelling error. For this reason, the classification results can be used to some extent to judge the relevance of the thesis.

1.2.3 Outline

In Chapter 2, the basic theory behind high-resolution radar imaging of airborne targets is presented. Starting with the principle of electromagnetism the chapter moves quickly to the principle of radar ranging and to ISAR imaging. The importance of bandwidth is highlighted throughout using examples involving different high-resolution waveforms.

In Chapter 3, the technique that is proposed in the article entitled "ultra-wide-band coherent processing of sparse subbands" and published in the Lincoln Laboratory Journal, is described in detail. The different stages of the techniques are described and explained using references to other articles. The capability of the technique for enhancing range resolution of simple targets that is presented in the article is illustrated with simulated signals.

In Chapter 4, the modelling technique is studied extensively using real and simulated signals. The sensitivity of the model to its own parameters is assessed in depth. Once the most sensitive parameters are identified, the risk

associated with each stage of the technique is analysed and potential causes of error identified. The study concludes by showing why the estimated model may not always be a physically accurate representation of the scattering mechanisms that characterise an aircraft. The assertion is supported by experiments using data from simulated scatterers, sphere on turntable and flying aircraft.

In Chapter 5, the proposed use of the model-parameter estimates to create a novel feature-based classification technique circumvents the conclusion of the fourth chapter. The alternative proposed with a different technique of classification, MAUCAZ, is designed to enable target classification based on the physically accurate elements of the model. Under certain conditions, the tests carried out with scaled aircraft show unrivalled performance.

In the last part of this thesis, the results obtained are summarised and a conclusion on the capability of the processing technique studied is drawn. Issues such are bandwidth extrapolation and target classification are especially considered. Finally, a series of future work are suggested. They are seen at this stage as the natural continuation of this work.

1.2.4 Publications and communications

Demonstrating that bandwidth extrapolation is limited by the poor accuracy of the scattering-centre model, and detecting the sources of error have required the investigation of the scattering-centre extraction technique. A number of results that are not directly related to the conclusion of this thesis have also been presented during various occasions at Rome Labs (USA), Naval Research Labs (USA), SELEX-Rome (Italy), BAE-Systems (UK), QinetiQ (UK) and ENSIETA (France).

The following publications have already resulted from this work:

[1] H. Borrion, H. Griffiths, and C. Baker, Sparse sub-band processing for ultra high resolution, Naval Research Labs, Washington, 2004 (unrefeered conference paper)

[2] H. Borrion, P. Tait, D. Money, C. Baker and H. Griffiths, Scattering centres extraction by sparse subband processing, Second Annual Tri-Service Waveform Diversity Workshop, Rome, NY, 2004 (unrefeered conference paper)

[3] H. Borrion, H. Griffiths, P. Tait, D. Money and C. Baker, Scattering centre extraction for extended targets, Radar 2005, IEEE Int. Conf., Wash-

ington, 2005, DOI: 10.1109/RADAR.2005.1435.814

[4] H. Borrion, H. Griffiths, P. Tait, D. Money and C. Baker, One-dimensional model-based approach for ISAR imaging, Geoscience and Remote Sensing Symposium 2005, IGARSS-2005 Proc., IEEE Int. Conf., Seoul, 2005, DOI: 10.1109/IGARSS.20051526170

[5] H. Borrion, H. Griffiths, P. Tait, D. Money and C. Baker, One-dimensional model-based approach for ISAR imaging (2), Geoscience and Remote Sensing Symposium 2006, IGARSS-2006 Proc., IEEE Int. Conf., Denver, 2006,

In addition, a number of publications are currently being written by the candidate.

Chapter 2

HIGH RESOLUTION RADAR

2.1 Introduction

This chapter introduces the theory behind radar imaging of airborne targets. Starting with the basic principles of electromagnetics, the first section then presents elementary techniques that extract the target reflectivity from the signal at the receiver. They involve the Fourier-transform and matched-filtering of high-resolution waveforms. Most problems are addressed in the time-domain at this stage of the processing. This chapter then presents the various assumptions that relate the target or scatterer location and the propagation-time in order to introduce the spatial domains: range and cross-range. The second section is concerned with high-resolution waveforms. Because they convey the information about the target, waveforms have a great importance and, of course, high range-resolution techniques rely on wide-band waveforms. The latter include short pulses, compressed pulses and synthetic bandwidth. The last part of this chapter uses turntable measurements as an example for approaching radar imaging in one and two dimensions. The techniques reviewed to achieve high-resolution radar-images include high-resolution range-profiles and inverse synthetic-aperture-radar imaging. This chapter concludes by examining the main sources of limitations found in the radar images.

2.2 Radar principle

2.2.1 Introduction

Radar generates electromagnetic waves that propagate in the air. When the transmitted wave encounters a target, it interacts with it by inducing currents on the surface and creating a scattered field. The quantity of energy at the receiver depends upon many target features including reflectivity and range to the target.

A branch of radar research attempts to estimate the reflectivity of the illuminated scene from the received signal. Scientists focus on four areas: transmission, interaction, reception and finally information retrieval through work on waveform-design and inversion techniques. Based on the constraints imposed by the physical mechanisms, the research described in this thesis contributes to the information retrieval through enhancement of the processing techniques.

If the physics of scattering is considered then the description of reflectivity in time can be obtained from the temporal variation of the received signal. Advanced radar provides high performance which allows engineers to work with phase as well as amplitude. This technology associated with advanced processing techniques enables accurate description of the target reflectivity in time.

By obtaining accurate relations between time of propagation and spatial location of the scatterers, it is possible to image the reflectivity from time to space. Correct estimates of the location and strength of the scatterers can thus be obtained by applying inversion techniques to a set of radar measurements. These are a valuable source of information for applications such as target recognition.

This section presents an overview of the basic radar principles and the techniques used to extract the reflectivity as a function of space. It starts with the radar-cross-section and moves on to processing techniques for building images of the reflectivity in the time domain or in the frequency domain.

2.2.2 Radar cross section

Introduction

In general, the received signal is considered as originating from the reflection of the transmitted signal from scatterers located along the line of sight. Although convenient, reflection is a simplistic way for characterising the interactions between waves and targets. In fact, an object present in an incident electromagnetic field anisotropically disperses some of the energy in all directions. This dispersal, called scattering, can be the result of very complex mechanisms. In their work, engineers use the radar-cross-section (RCS) to quantify the spatial distribution of the target reflectivity.

Definition

Skolnik [46] defines the radar-cross-section, σ, as a quantitative measure of the ratio of power in the signal scattered in the direction of the receiver to the power density of the radar wave incident upon the target.

$$\sigma = \frac{\text{equivalent isotropic reradiated power}}{\text{incident power density}} \tag{2.1}$$

In other words, the RCS of an object can be defined as an equivalent area intercepting that amount of power which, when scattered isotropically, produces at the radar receiver a power density which is equal to that scattered by the real object. This is given by

$$\sigma = 4\pi \lim_{R\to\infty} \left|\frac{E_s}{E_i}\right|^2 R^2 \tag{2.2}$$

where

- E_i is the magnitude of the electric field component of incident electromagnetic (EM) field, $(V.m^{-1})$
- E_s is the magnitude of the electric field component of scattered EM field as measured by hypothetical observer, $(V.m^{-1})$
- R is the distance from target to observer (m).

As the name suggests, the RCS has dimensions of area: metre-squared. In general, it is given in decibels relative to one square metre $(dBsm)$ because it may vary over rather wide limits. The RCS in m^2 can be converted into $dBsm$ by the following equation.

$$\sigma(dBsm) = 10.log_{10}(\sigma/1m^2) \tag{2.3}$$

Far field

Knott *et al.* provide a basic far-field criterion [23]. For a target of principal dimension D_T, the range to the radar R must satisfy

$$R > 2\frac{D_T^2}{\lambda} \tag{2.4}$$

For instance, a Boeing-727 of principal dimension $D_T = 50\ m$ and located at 50 km requires a wavelength greater than 10 cm for the scattered wave to satisfy the Far-field criterion.

Some values for RCS

The following table provides typical values of RCS at X-band for the frontal sector of different types of target. [52]

Type	RCS in m^2	RCS in $dBsm$
Large commercial airplane	100	20
Large fighter	5	7
Small fighter	2.5	4
Man	1	0
F-117 fighter	0.03	-15
Small bird	0.01	-20

Variability

In [23], Shaeffer describes the normalised radar-cross-section to be a function of both the obstruction (*i.e.* target) and the incident wave. For simplicity, we do not include polarimetry in this analysis. In this case and for monostatic radar, the parameters can be reduced to

- position of radar relative to the target
- target geometry and material composition
- frequency (f) or wavelength (λ)

It is important to distinguish between the parameters that concern the target and those that depend upon the radar only and therefore may be controlled. For example, the target geometry cannot be changed; furthermore it is an unknown parameter in the high-resolution problem. In contrast, the frequency of the incident wave can generally be controlled.

Directivity

When considering radar problems, one must take into account that both the energy of transmission by the radar and the energy scattered by the target generally have an unequal distribution in space. Angular directivity is provided in the form of a beam generated by the radar antenna. The larger the antenna, the greater the directivity. The angle between half-power points of the resulting beam is given by

$$\Delta\theta_h = \frac{\lambda}{2D_A} \tag{2.5}$$

where λ is the wavelength and D_A is the main dimension of the antenna [52].

For a narrow beam, the illuminated scene depends upon the pointing direction of the radar (the bore-sight). In order to scan a large volume of space with narrow beam the initial solution was to rotate the radar antenna. Now a phase-array antenna can steer the beam via electronic control of the phase relationship between the transmit and receive elements comprising an array.

2.2.3 Scene reflectivity in time

Signal representation

The signal represented by a radar waveform can be written in mathematical terms as

$$w(t) = a(t).cos(\phi(t) + \omega_0.t) \tag{2.6}$$

where $a(t)$ is the envelope, $\phi(t)$ is the phase modulation and ω_0 is the carrier-frequency [46].

When the envelope and phase modulation functions are varying slowly compared to the carrier signal, the Fourier transform presents frequency components concentrated around the carrier frequency. The narrow-band approximation of the emitted signal is an important aspect as the energy is then located within a small region of the spectrum. Because radars are band-limited, so are the received signals. For this reason, radar signals are often written as a complex-valued waveform called the quadrature model:

$$s(t) = a(t).e^{i\Phi(t)} \tag{2.7}$$

where $\Phi(t) = \phi(t) + \omega_0.t$ is the instantaneous frequency.

Let us consider an electromagnetic wave satisfying the one-dimensional wave equation and propagating along the axis y. The waveform can be formulated by

$$w(y,t) = \begin{cases} s(y/c - t) & \text{for the transmitted wave} \\ s(y/c + t) & \text{for the reflected wave} \end{cases} \tag{2.8}$$

where c is the speed of propagation in the medium.

The expression for the signal at the receiver, w_r, as a function of the transmitted signal, w_t, given by equation 2.9, is a fundamental aspect of the direct problem in radar.

$$w_r(t) = \varsigma(t) \otimes w_t(t) \tag{2.9}$$

where $\varsigma(t)$ is the impulse response of the reflectivity filter corresponding to the illuminated scene and $\otimes$ is the convolution operator. The problem is that of extracting $\varsigma(t)$.

Point-scatterer model

At this stage, it is convenient to introduce a scattering model that can be used to derive the impulse response of the filter that is associated with the scattering scene. A simple way to describe the physical interactions between a wave and the target is through the so-called point-scatterer model. Let us assume that the target is composed of M non-interacting point-like spheres in free space. The transmitted wave creates a current on the target which generates an electromagnetic field similar to the emitted one. For a coefficient of reflectivity A_m and a time of propagation t_m, the received waveform for the m^{th} scatterer in a non-dispersive medium, is given by

$$w_r(t) = A_m . w_t(t - t_m) \tag{2.10}$$

Figure 2.1 illustrates the concept of a point-scatterer for direct path propagation. Here $d_m = c.t_m/2$ is the one-way distance between the radar and the m^{th} scatterer.

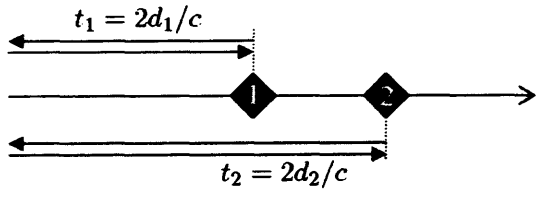

Figure 2.1: Concept of the point-scatterer model

According to this model, a signal at the receiver would be the sum of scaled and time-delayed replicas of the emitted waveform; each return being attributed to one scattering element called point-scatterer. This model is the foundation for most high-resolution imaging methods. Assuming that there is no interaction between the M point-scatterers that compose an hypothetical target, the reflectivity function of the target in the one-dimensional time domain is of the form of 2.11

$$\varsigma(t) = \sum_{m=1}^{M} A_m.\delta(t - t_m) \qquad A_m \in \Re \tag{2.11}$$

where $\delta(t)$ is the Dirac function.

In practice this model is very simple because it does not take into account the multipath or secondary waves that are induced by currents travelling on the structures.

System characterisation

A very common equation in the time-domain can be derived from 2.9 and 2.11.

$$w_r(t) = w_t(t) \otimes \sum_{m=1}^{M} A_m.\delta(t - t_m) \qquad A_m \in \Re \tag{2.12}$$

where the variables are defined in the previous section.

To characterise such a system, one can use the response to an impulsive excitation in the time-domain or alternatively the response to continuously swept frequency in the frequency domain.

- Time-domain

  A matched filter is used to maximise the signal-to-noise ratio at the receiver while preserving all the information of the signal. The instantaneous frequencies are calculated by the time-derivative of phase as a function of time.

  Let us consider the cross-correlation between the return $w_r(t)$ and a test signal $w_{test}(t)$ given as ζ in 2.13.

$$\zeta(t) = w_r(t) \otimes w_{test}(t) = \int_{\Re} w_r(t).w^*_{test}(t - \tau)d\tau \tag{2.13}$$

  where $\bullet^*$ denotes the complex conjugate. The signal returned from a fixed point-target is given by the correlation of the transmitted signal

with the reflectivity function described in 2.11. Its expression is given by

$$w_r = \sum_{m=1}^{M} A_m . w_t(t - t_m) \tag{2.14}$$

For independent point-targets in Gaussian noise, the optimal receiver is the correlator that performs time-correlation over a period of observation T between the received signal and the transmitted signal. The output of the matched filter is expressed as

$$\zeta(t) = \sum_{m=1}^{M} A_m \int_T w_t(\tau) . w_t^*(t - t_m - \tau) d\tau \tag{2.15}$$

In this case, the cross-correlation is optimal for $w_{test} = w_r$ and $t = t_m$. Eq. 2.15 is known as the one-dimensional radar mapping equation.

- Frequency domain

  The relation between the time-domain and the frequency-domain is a fundamental element of modern imaging techniques. Scattering models show that it is generally easier to treat the inverse problem in the frequency-domain but radar images require the scattering functions to be given in the time (range) domain. This is generally achieved by Fourier transforming the baseband-signal. The Fourier-transform and the inverse Fourier-transform are defined by equations 2.16 and 2.17.

$$S(\omega) = \mathcal{F}\{s\}(\omega) = \int_{\Re} s(t') . e^{-i\omega t'} dt' \tag{2.16}$$

$$s(t) = \mathcal{F}^{-1}\{S\}(t) = \frac{1}{2\pi} \int_{\Re} S(\omega' t) . e^{-i\omega' t} d\omega' \tag{2.17}$$

The above equations ensure that the information related to the spatial location of the target can be retrieved to some extent whether the reflectivity function is described in the time domain or in the frequency domain.

When applying the Discrete Fourier Transform to a vector, it is common to add a sequence of zeros at the ends of this vector before it is transformed. By introducing more points into the vector this operation, called zero-padding, does not improve the resolution but makes the spectrum smoother and subsequently more suitable to its interpretation by humans.

The output of the Fourier Transform and Matched Filter are not the same. Nevertheless, the first moment of the Fourier frequency is equal to the first moment of the instananeous frequency. In fact, when $a(t)$ is varying slowly, the second moments are also the same [29]. Both the impulse response and the transfer-function provide a good representation of the scene reflectivity that can be used for imaging or classifying targets.

Figure 2.2 illustrates the principle of radar imaging based on the transfer-function. The spectrum of the received waveform, W_r, can be seen as resulting from the modification of the spectrum of the transmitted waveform, W_t by the filter associated with the target and its environment. The filter with the correct transfer-function, $H(f)$, enables the target reflectivity to be imaged as a function of time or space.

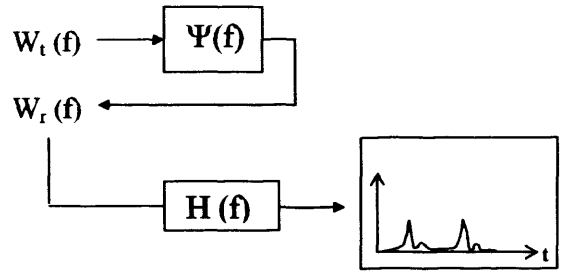

Figure 2.2: Principle of radar imaging

Resolution

The description of the reflectivity function in time enables discrimination of returns having different times of propagation. However, the time-domain response of short pulses is only an approximation of the so-called impulse-response of the illuminated scene. In practice, it relies upon the waveform transmitted. The shorter the pulse, the better the resolution. The duality between time and frequency means that the resolution is therefore affected by the signal bandwidth in the same way. In 2.16, Fourier components are defined over an infinite integration. Because the domain on which the reflectivity is measured is limited, the determination of the spectral contents by discrete Fourier Transform is only an estimate with limited resolution.

The criterion chosen by Lord Rayleigh to define the limit of resolution of a diffraction-limited optical instrument is also applicable to radar. Initially, it is "the condition that arises when the centre of one diffraction pattern is superimposed with the first minimum of another diffraction pattern produced

by a point source equally bright as the first." For a radar, it is defined as the distance between two point-scatterers so that the intersection of the returns is 9 dB below their maximum value. This case implies that the output of the matched filter is characterised by a trough greater than 3 dB.

One can address this in terms of actual radar resolution. For a simple pulse, the temporal resolution is directly derived from the duration of the pulse as defined by the time-width at 3 dB below the peak. In order to derive the spatial resolution from this, one needs to introduce the relation between time-of-propagation and target distance. This introduces the problem studied in the next section.

2.2.4 Scene reflectivity in space

Introduction

The description of the target reflectivity as a function of time provides useful information that can be used to retrieve the distance of propagation associated with each scatterer. From this expression, it is also possible to retrieve the location of the scatterers by making some assumption about the target structure, the target-motion and the scattering mechanisms involved.

Range

The previous section presented two techniques for obtaining the representation of the reflectivity as a function of time. They are Fourier-transformed and matched-filtered. The image obtained can be transposed onto the range domain using 2.18.

$$r_k = \frac{c}{2t_k} \tag{2.18}$$

where t_k is the propagation time (s) and r_k is the one-way propagation distance (m) associated with the m^{th} scatterer. In one dimension, the resulting image is known as a High-Resolution Range-Profile (HRRP) or simply a range-profile. It can be seen as a projection of the reflectivity onto the direction of propagation.

The echoes from two scatterers that are distant in range are said to be resolved when they produce two distinct returns in time. This implies that short-duration pulses enable resolution of closely spaced targets. As the equivalent of the pulse duration in the frequency domain is the signal bandwidth, methods applying the Fourier Transform of a band-limited signal have limited resolution.

As discussed earlier, it is common to define the resolution by the peak width of a single point echo measured at 3 dB below its maximum value. The nominal range resolution Δr is given for two point-targets by

$$\Delta r = \frac{c}{2B} \tag{2.19}$$

where B is the bandwidth (Hz).

Wehner defines the range resolution of a radar in terms of its "ability to resolve point targets that are separated in range to the radar" [52]. The nominal range resolution is the minimum distance between two resolvable targets travelling at the same speed and giving the same reflectivity amplitude.

Large bandwidth can be exploited for surveillance to detect targets that are closely spaced. Several waveforms can be used to achieve the desired bandwidth:

- continuous pulse of small time-duration
- continuous long modulated waveform
- continuous synthetic bandwidth
- sampled synthetic bandwidth

Such waveforms can provide enough resolution to distinguish between scatterers that are separated in range by only few centimetres. However, when the target is moving, the translation of the scatterer introduces a frequency component known as Doppler-frequency. The following section shows how the variation of range can affect the accuracy of the range profile or alternatively how it be used to estimate the target speed.

Doppler

The system described by radar is limited to the scene illuminated by the properties of the transmitted wave, the pattern of radiation and the time-gate of the receiver. For air-targets, the scene is generally not stationary in time. For instance, the reflectivity of a scene containing a flying aircraft changes with time since the position of the aircraft varies continuously. These variations appear through the rate of change of relative phase as a function of time. The faster the aircraft, the greater the variation in time. This effect, known as Doppler effect, is exploited by a class of radars to retrieve the components of the target-speed along the line of sight of the radar.

Let a target be flying towards a stationary radar at speed v_m. According to the point-scatterer model, a series of N narrow-band pulses transmitted at time $t_t = 0$ separated by pulse-repetition-interval, T_I, produces a series of N echoes. The n^{th} pulse arrives at the radar receiver at time t_r given by equation 2.20.

$$t_r = (n-1).T_I + 2.d_m/c \qquad n = 1, 2, \cdots, N. \tag{2.20}$$

For a target travelling at constant speed, the distance of the radar to the scatterer d_m decreases linearly with time following the relation 2.21

$$d_m(t) = d_m(0) + v_m.t \tag{2.21}$$

where $d_m(t)$ is the distance between the radar and the scatterer at time t. According to the point-scatterer model, the phase-shift measured between the n^{th} pulse and the n^{th} echo is given by

$$\Delta\phi_n = -\frac{4\pi}{\lambda}(d_m(0) + v_m.T_I) \tag{2.22}$$

The time derivative of the phase is given by

$$\frac{\partial\phi}{\partial t} = -\frac{4\pi.v}{\lambda} = 2\pi.f_D \tag{2.23}$$

where f_D is the Doppler frequency given by relation 2.24

$$f_{Dm} = -\frac{2v_m}{\lambda} \tag{2.24}$$

If the relative phase-shift $\Delta\phi$ measured for two targets is the same, it means that either the targets are travelling at same speed toward the radar or that the targets are travelling at speeds that induce identical relative shifts; in other words $\Delta\phi_1$ and $\Delta\phi_2$ are such that $\Delta\phi_2 - \Delta\phi_1 = 2\pi.k$ where k is positive or negative integer. A pulse repetition interval $PRI = T_I$ yields a corresponding ambiguous Doppler speed called the blind speed given by relation 2.25

$$v_{blind} = \frac{k.\lambda}{2T_I}, \qquad k = \pm 1, \pm 2, \cdots \tag{2.25}$$

The Doppler effect is exploited by radar to measure car speed by transmitting narrow-band pulses on highways for instance. However, these radar systems are unable to resolve scatterers whose contribution produce identical relative phase-shifts. Radar that can estimate both range and Doppler information can be used to build two-dimensional images. For exploiting the variations of reflectivity in time, it is important to distinguish the contributions that are due to the target-motion and the contributions that are due to other scatterers located further away in range.

Cross-range

High range-resolution radars could not resolve point-like targets that are located on a radius centred on the radar location because they would all create identical phase-shifts. In this case, a smaller beamwidth is needed to resolve them in the cross-range dimension. When this is not possible, one can exploit the Doppler effect associated with rotating scatterers to infer their position in cross-range. This section proposes one method for estimating the position of a scatterer in cross-range by measuring the Doppler frequency associated with this scatterer when the target is moving with respect to the radar.

The illumination of the targets varies according to the spatial pattern of radiation of the antenna. Accurate estimation of target positions requires scatterers to be discriminated in cross-range using narrow beams. This condition enables high cross-range resolution to be achieved according to 2.26.

$$\Delta r_c = \frac{\lambda}{2\delta\theta} \tag{2.26}$$

where λ is the wavelength (m) and $\delta\theta$ is the aperture (rad).

We can estimate the positions of scatterers for which the returns would generate identical phase-shifts at the radar antenna. For non-interacting isotropic point-scatterers, these positions define portions of concentric spherical surfaces. Let us generalise this idea by considering that any set of measurements is characterised by an iso-Doppler domain which defines a domain of ambiguity in space. This ambiguity domain can be reduced by adding measurements characterised by different domains of ambiguity. This can be done by varying the spatial domain of the measurements.

In order to remove the ambiguity in the cross-range direction, the measurements exploit the diversity of paths coming from a same scatterers by either acting directly on the spatial properties of the antenna or relying on the target motion, *e.g.*

- antenna of large time-extent (large aperture)
- non-linear small aperture
- synthetic aperture (SAR)
- sampled aperture (array, network)
- inverse synthetic aperture (ISAR)
- inverse sampled aperture

Depending on the method chosen, various processing techniques can be used to retrieve the information in two-dimensions. In this chapter we present some results using inverse synthetic-aperture but firstly we introduce the various types of high range resolution waveforms.

2.3 High range-resolution waveforms

2.3.1 Introduction

This section introduces three different types of waveforms including a simple pulse of short duration, modulated pulse and synthetic waveform.

2.3.2 Simple pulse

For target detection, radar systems rely on a spatial description of the reflectivity. HRR radar systems transmit waveforms whose spatial support is smaller than the target. The pulse excites the target's sub-elements which re-radiate some of the energy back to the receiver. Non-interacting point-targets produce a signal composed of pulses shifted in time. Under certain conditions, the range of each scatterer can be deduced from the delay of the echoes.

The bandwidth of simple pulses can be approximated by

$$B = \frac{1}{\tau} \tag{2.27}$$

where τ is the pulse-width (s) given at about 3 dB below the maximum as represented in figure 2.3.

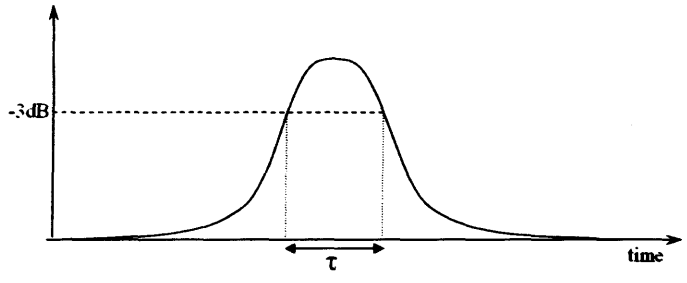

Figure 2.3: Simple pulse

The corresponding nominal resolution is given by

$$\Delta r = \frac{c\tau}{2} \tag{2.28}$$

In order to achieve high range-resolution, simple pulse systems require short signals. However, because the duration of the pulse is related to the energy transmitted, a reduction of the pulse's duration must be compensated by an increase of the power, otherwise the signal-to-noise ratio drops. In conclusion, a simple pulse suffers from high power requirements or limited detection. Ultimately it is limited by practical considerations such as voltage breakdown in the high power circuitry.

2.3.3 Pulse compressed waveform

Pulse compressed waveforms overcome the problem that characterises simple short-pulses. This class of waveforms is now extensively used and provides high-resolution without the constraints applied to the signal-to-noise ratio. The principle consists of modulating the pulse in such way that the frequency of the pulse increases with its duration. The linear frequency modulation (LFM) also known as chirp is certainly the most widely used. Here the instantaneous frequency of the waveform varies linearly with time. The signal of duration T can be written as the product of the baseband signal and the modulation signal in 2.29.

$$w_t(t) = a(t).e^{i2\pi f_c t}.e^{i\pi\gamma t^2} \tag{2.29}$$

where $a(t) = rect(\frac{t}{T})$ and γ is the chirp rate $(Hz.s^{-1})$. An example is shown in figure 2.4.

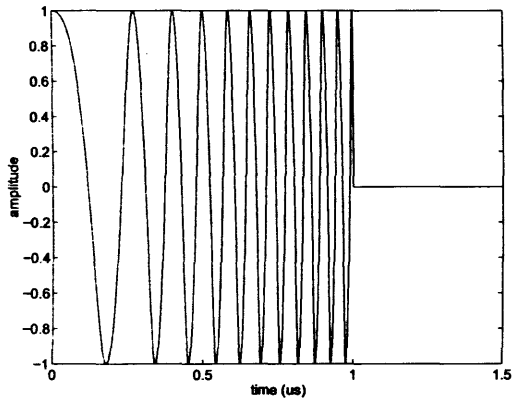

Figure 2.4: Chirp signal in the time domain - $w_t(t)$

From 2.12, the received signal, w_r, is given in 2.30 by the convolution of the scene reflectivity function $\varsigma(t)$ and the transmitted pulse.

$$w_r(t) = \varsigma(t) \otimes w_t(t) = \int_{\Re} \varsigma(t-\tau)w_t(\tau).d\tau \tag{2.30}$$

The return from a point target located at range $d_m = c.t_m/2$ is given by

$$w_r(t) = A_m.w_t(t-t_m) = A_m.a(t-t_m).e^{i2\pi f_c(t-t_m)}.e^{i\pi\gamma(t-t_m)^2} \tag{2.31}$$

By mixing the complex conjugate of this received signal with the phase of the transmitted chirp signal, we obtain the general expression in 2.32

$$w_m = w_r^*.e^{i(2\pi f_c t + \pi\gamma t^2)} \tag{2.32}$$

For the compressed waveform, the signal at the output of the mixer is given by

$$w_m(t) = A_m.a^*(t - t_m)e^{i(2\pi f_c t_m - \pi\gamma t_m^2)}e^{i2\pi\gamma t_m t} \tag{2.33}$$

The frequency components of 2.33 contain the information about the distance t_m. The discrete Fourier spectrum of the compressed signal shows the distribution of energy at different frequencies which span the reflectivity at different ranges:

$$\mathcal{W}(\omega) = \sum_{m=1}^{M} A_m.e^{i(2\pi f_c t_m - \pi\gamma t_m^2 - \omega t_m)} psf\Big(\omega - 2\pi\gamma t_m\Big) \tag{2.34}$$

where the point spread function in the frequency domain is

$$psf(\omega) = \mathcal{F}\{a^*(t)\} \tag{2.35}$$

The maximum absolute value of the function tells us the best estimate of the range to the point scatterer in Gaussian noise. For example, a target at range r_m will appear at the frequency $f_m = 2r_m/c$

Here the function $a(t)$ is a rectangular function in the time domain. Therefore the point spread function is a sinc function. This means that the range profile of point-targets is given by the convolution of sinc functions with delta function. For two closely spaced targets, the resolution is limited by the width of the sinc function. In terms of 3 dB-width, the nominal range resolution is given by

$$\Delta r = \frac{c}{2\gamma T} \tag{2.36}$$

where $B_{eff} = \gamma.T$ is the effective bandwidth (Hz).

The sinc function is also characterised by secondary lobes at 13 dB below the principal one. Weighting may be used to prevent peaks from weak targets being overlaid by the secondary lobes from a stronger target. However, weighting affects the resolution.

2.3.4 Synthetic waveform

Introduction

This principle relies on the duality between time-domain and frequency-domain. It is possible to create a wide spectrum with limited constraints applied on the hardware by assembling segments in the frequency domain. For instance, step-frequency radars transmit waveforms where the carrier-frequency is increased by discrete steps from pulse to pulse. When the segments are overlapping, filters can be used to flatten the spectrum [53], [21]. In contrast, when segments are not contiguous, range-ambiguities arise that vary with the sampling-rate. Figure 2.5 represents a stepped frequency waveform:

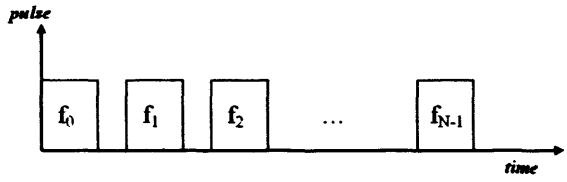

Figure 2.5: Stepped frequency transmitted waveform

Principle

Stepped-frequency radar achieves waveforms with large effective bandwidth by emitting successive relatively narrow-band pulses whose carrier-frequency is sequentially increased. The transmitted waveform is typically a monochromatic signal whose duration corresponds roughly to the inverse of the desired instantaneous bandwidth. It follows that this technique enables wide effective bandwidth to be synthesized without direct reliance on the implied necessary analogue to digital (A/D) sampling-rate.

The concept of synthetic range profile generation can be summarised as follows [52]:

1. Transmit a series of N pulses whose central frequency is swept from pulse to pulse by a constant bandwidth Δf called the frequency step
2. Set a range delayed sampling gate to collect I and Q samples of target baseband echo responses for each transmitted pulse (matched filter)
3. Store the quadrature components of each of the N echo signals. The complete set describes the frequency signature of the target's reflectivity

4. Compute the inverse discrete Fourier Transform of the resulting set of N samples to obtain the N components in the time domain.

Theory

Let a sequence of N narrowband waveforms emitted with linearly increasing frequency f_n given by

$$f_n = f_0 + n.\Delta f, \quad n = 0, 1, \cdots, N-1 \tag{2.37}$$

where Δf is the frequency-step and n the index related to the frequency f_n.

The signal transmitted at the frequency f_n is modelled by

$$w_t(t) = s_b(t).e^{i.2\pi(f_0+n\Delta f)t} \tag{2.38}$$

where $s_b(t)$ is the baseband signal.

The received signal is given by the convolution of the scene reflectivity function $\varsigma(t)$ and the transmitted pulse.

$$w_r(t) = \varsigma(t) \otimes w_t(t) = \int_T \varsigma(t-\tau) w_t(\tau).d\tau \tag{2.39}$$

For example, the signal received from a point-target with reflectivity $\varsigma_m(n,t)$ at range r_m is

$$w_r(t) = \varsigma_m(n,t).s_b(t-t_m).e^{i.2\pi(f_0+n\Delta f)(t-t_m)} \tag{2.40}$$

Coherent demodulation is applied to the received signal yielding the output signal, w_c, in 2.41.

$$w_c(t) = w_r(t).e^{-i2\pi f_n t} \tag{2.41}$$

Combining 2.40 and 2.41 yields the expression of the baseband signal reflected by a point scatterer:

$$w_c(t) = \bar{\varsigma}_m(n,t).s_b(t-t_m).e^{-i.2\pi n\Delta f.t_m} \tag{2.42}$$

where $\bar{\varsigma}_m(n,t)$ is the complex reflectivity of the point-target at range r_m

$$\bar{\varsigma}_m(n,t) = \varsigma_m(n,t).e^{-i2\pi f_0 t_m} \tag{2.43}$$

After matched-filtering, the signal is given by:

$$w_m(\Delta t) = \int_{Tr} \sum_{n=0}^{N-1} \bar{\varsigma}_m(n,t) s_b(t - n\Delta t - t_m).e^{-i.2\pi n\Delta f.t_m} \cdot \sum_{k=0}^{K-1} s_b^*(t - k\Delta T - \Delta t).e^{i.2\pi k\Delta f\Delta t} dt \qquad (2.44)$$

For a stationary target, the amplitude normalised with respect to the transmitted power is

$$|w_m(\Delta t)| = \bar{\varsigma}_m(n).|c_1(\Delta t)|.|c_2(\Delta T)| \qquad (2.45)$$

where c_1 is the frequency-domain sampling filter

$$c_1(\Delta t) = \frac{sin(\pi N \Delta f(t_m - \Delta t))}{sin(\pi \Delta f(t_m - \Delta t))} \qquad (2.46)$$

and c_2 is the pulse matched filter

$$c_2(\Delta T) = \int_T s_b(t - t_m) s_b^*(t - \Delta T) dt \qquad (2.47)$$

The filters c_1 and c_2 are now examined separately.

1. The frequency-domain sampling filter: $c_1(\Delta t)$

   The response of the pulse-matched receiver is multiplied by a function c_1 in the form of $sin(Nx)/sin(x)$ as a result of discrete sampling. The width at 3 dB below the maximum is similar to those of the *sinc* function. The width is inversely proportional to the number of samples and to the frequency step.

$$\tau_{3dB} = \frac{1}{N.\Delta f} \qquad (2.48)$$

   The function is also characterised by its repetition in the time domain. It repeats itself with a period T_{max} given by

$$T_{max} = \frac{1}{\Delta f} \qquad (2.49)$$

T_{max} is also the maximum delay between two returns in the synthesized time-domain response. This is related to the Nyquist sampling criterion for unambiguous reconstruction. The interval between samples in the frequency domain (or frequency step) must be smaller than the minimum bandwidth of the signal. In this case, the minimum bandwidth is given by the inverse of T_{max} in 2.49. It corresponds to an unambiguous range given by

$$R_{unambiguous} = \frac{c}{2\Delta f} \tag{2.50}$$

The range ambiguity due to discrete frequency sampling can be explained by observing the phases of the returns from two point-scatterers located at different ranges d_1 and d_2. There is ambiguity in 2.42 if both phases are identical, that is

$$\phi_2 - \phi_1 = 2\pi.\Delta f(t_2 - t_1) \propto 2\pi \tag{2.51}$$

or identically if the distance between scatterers is an integer value of half step-wavelength $\Delta\lambda$ is given by

$$d_2 - d_1 = K.\frac{\Delta\lambda}{2} \tag{2.52}$$

The maximum delay between the two returns is associated with the unambiguous range according to 2.53:

$$T_{max} = \frac{2R_{unambiguous}}{c} \tag{2.53}$$

As an example, we have considered the frequency-domain sampling filter c_1 for a waveform composed of $N = 20$ pulses separated by $\Delta f = 1.5\ MHz$. Figure 1 represents one period whose total extent is $1/\Delta f = 0.67\ \mu s$. The corresponding unambiguous range is $R_{unambiguous} = 100\ m$. The 3 dB-width ($\tau = 33\ ns$) implies the range resolution of the 30 MHz-bandwidth synthetic waveform is $\Delta r = c/(2\tau) = 5\ m$.

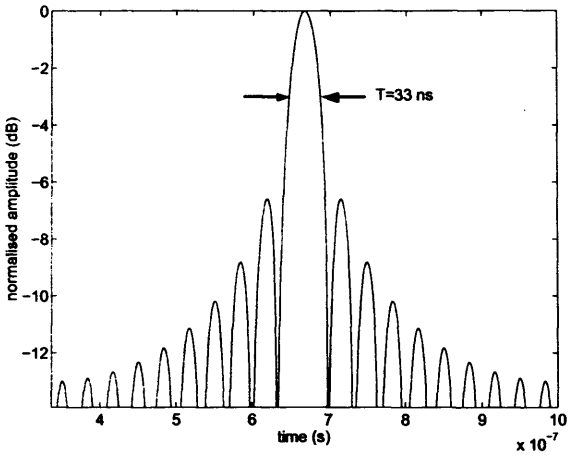

Figure 2.6: Width of the function $\sin(Nx)$ / $\sin(x)$

2. Pulse-matched filter: $c_2(\Delta T)$

The pulse-matched filter, c_2, is given by

$$c_2(\Delta T) = \int_T s_b(t - t_0).s_b^*(t - \Delta T)dt \tag{2.54}$$

The imaged area is given by the extent of the matched-filter's impulse-response. Ideally the unambiguous range should be larger than the imaged window. This condition ensures that the spectrum of the matched filter does not overlap on other $\sin(Nx)/\sin(x)$ patterns. This prevents an extended target from wrapping on itself (*i.e. aliasing*). Practically, the condition 2.55 is given in terms of 3 dB width.

$$R_{imaged} \leq R_{unambiguous} \tag{2.55}$$

In practice, it is usual to set the frequency step equal to the narrow bandwidth, that is:

$$\Delta f = \Delta B \tag{2.56}$$

The individual pulses of bandwidth ΔB must be sampled in the time-domain according to the sampling theorem for two channels:

$$\tau_s \leq \frac{1}{\Delta B} \tag{2.57}$$

The energy reflected from the imaged scene is distributed in time. For one target, the energy is present across the pulse duration τ. For a given sampling interval τ_s, the target is present on M range bins with different powers. The value of M can be calculated with 2.58.

$$M = \tau/\tau_s \tag{2.58}$$

To solve this ambiguity, the Discrete Fourier transform of M pulses at different frequencies must be performed. The condition for collecting at least one sample is given by the sampling theorem in the time-domain.

The simplest case is composed by N narrow-band monochromatic pulses separated by a pulse repetition interval (PRI) of T seconds. Each pulse of duration τ and frequency f_n can be written as 2.59:

$$w_t(t) = rect(\frac{t - \tau/2}{\tau}).e^{i.2\pi f_n t} \tag{2.59}$$

According to 2.54, the pulse-matched filter is a triangular function spanning twice the pulse duration. The 3 dB width measures half the length of the basis of the triangle. Therefore the imaged area is given directly by the pulse duration:

$$R_{imaged} = \frac{c}{2\Delta B} \tag{2.60}$$

From this follows the sampling rate conditions for avoiding aliasing

$$\frac{1}{2\Delta B} \leq \frac{1}{\Delta f} \tag{2.61}$$

It is convenient to chose a sampling time τ_s equal to the PRI. The return from a stationary point-target can be written as follows:

$$s(t) = \sum_{n=0}^{N-1} \varsigma.rect(\frac{t - n\Delta t - t_0 - \tau/2}{\tau}). \tag{2.62}$$
$$e^{i.2\pi f_n(t-n\Delta t-t_0)}.e^{-i.2\pi n\Delta f t_0}.e^{-i2\pi f_0 t_0}$$

The frequency step is often half of the bandwidth. However there is a special case known as synthetic waveform where they are equal. In this case, the total bandwidth is given by

$$B = N.\Delta f \tag{2.63}$$

The corresponding nominal resolution is given by

$$\Delta r = \frac{c}{2N\Delta f} \tag{2.64}$$

The signal received from P scattering centres can be written as a series of exponentials

$$s(n) = \sum_{p=1}^{P} \rho_p(n) e^{-i4\pi \frac{r_p}{c} \Delta f.n}, \qquad n = 1 \cdots N \tag{2.65}$$

$\rho_p(n)$: complex amplitude coefficient

r_p: one-way distance (m)

The inverse discrete Fourier transform of the measurement sequence is computed. The value at range bin m is given by

$$S(m) = \sum_{n=0}^{N-1} s(n).e^{i2\pi \frac{mn}{N}} = \sum_{n=0}^{N-1} \sum_{p=1}^{P} \rho_p(n).e^{-i2\pi(\frac{2r_p}{c}\Delta f + \frac{m}{N})n} \tag{2.66}$$

For a single target (P=1) with no frequency dependence, the absolute value can be approximated by

$$|S_1(m)| = \rho_1^2 \left| \frac{sin(\pi y)}{sin(\pi y/N)} \right|^2 \tag{2.67}$$

with $y = m - \frac{2Br_1}{c}$ where $B = n.\Delta f$

When using one sample per frequency, one needs to make sure that this sample contains the information from all scatterers. If the pulse is too short then sparse scatterers may generate distinct returns. In this case, information is lost. The extreme situation arises when the beginning of the return from the last scatterer occurs at the same time (t_i) as the end of the return from the first scatterer (t_f). Therefore for a pulse of duration τ, we need to have

$$t_f - t_i < \tau \tag{2.68}$$

It follows that

$$\frac{2(d_f - d_i)}{c} < \frac{1}{\Delta B} \tag{2.69}$$

Using the ratio between the unambiguous range and the range imaged, k, we have the relation in 2.70:

$$k.\Delta f > \Delta B \tag{2.70}$$

This defines the boundaries of the frequency step expressed in 2.71:

$$\frac{1}{k}.\Delta f < \Delta B < 2\Delta f \tag{2.71}$$

where

$$k = \frac{R_{unambiguous}}{R_{imaged}} \geq 1 \tag{2.72}$$

For example, if the imaged window is half the unambiguous range then one must chose the step frequency such that it satisfies the relation in 2.72

$$\frac{\Delta f}{2} < \Delta B < 2\Delta f \tag{2.73}$$

The basic principle of waveform designing have been introduced in this section. The following section presents some techniques commonly used to extract the information from the received waveform in order to create a radar image.

2.4 Radar imaging

2.4.1 Introduction

For imaging, it has been shown that range and cross-range resolutions have reliance upon the bandwidth and the aperture, respectively. By moving the radar or the target, it is possible to artificially synthesize an aperture. Measurements repeated during the formation of this aperture can be exploited for estimating the location of the scatterers in the cross-range direction. Techniques that exploit the variation of aspect-angle include Synthetic-Aperture-Radar (SAR), Inverse Synthetic-Aperture-Radar (ISAR), spot SAR and tomography. They create two-dimensional images whose quality relies upon the relative radar-to-target motion. Measurements obtained for various aspect-angles can be used to build a database of one-dimensional range-profiles as a function of aspect-angle. The variation of aspect-angle increases the amount of information via improvement in cross-range resolution. Based on the theory presented earlier, this part of the chapter approaches imaging techniques using turntable measurements and is therefore based upon the principles of ISAR.

2.4.2 Measurements

Principle

Imaging techniques process radar signals measured or simulated over a range of frequencies and aspect-angles. The system used here is known as a turntable. It consists of a rotating plaform on which a target is placed. The rotation allows illumination of the target from various aspect-angles. For a given angular position of the turntable, transmission of a wide-band waveform enables determination of a detailed range profile. As stated earlier, fine signatures can only characterise targets for the perspective taken by the radar during the measurement. By repeating the measurements for various aspect-angles, one can collect series of bursts at the receiver. This dataset constitutes a large support of information with two degrees of freedom, bandwidth and aspect-angle. It can then be exploited in various ways. This section successively presents techniques for building one or two-dimensional images including high-resolution range profiles and Inverse Synthetic Aperture Radar (ISAR) images.

Geometry

Let a general coordinate system be defined by an orthonormal basis of three unit-vectors $\{\vec{x}, \vec{y}, \vec{z}\}$. The turntable is centered on $O'(R_0, 0, 0)$ and rotates according to the rotation vector $\vec{\omega} = (0, 0, \omega)$. It has its own coordinate system $\{\vec{x}', \vec{y}', \vec{z}'\}$ with its origin at the centre of rotation O'. At a

given time the rotation angle can be defined by $\theta(t) = \omega.t$ if the rotation is continuous or by $\theta(n) = \Delta\theta.n$ if the rotation is performed by discrete steps $\Delta\theta$.

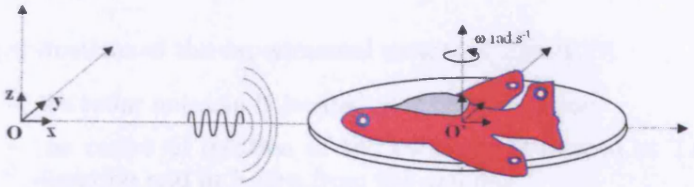

Figure 2.7: Geometry of a turntable from side

Let us formalise the definition of the distance for the two-dimensional case. For a target composed of M scatterers, the position of the m^{th} scatterer can be expressed in the general system by $\overrightarrow{OP_m} = x_m.\vec{x} + y_m.\vec{y}$ or alternatively in the turntable system by the vector $\overrightarrow{OP'_m} = x'_m.\vec{x}' + y'_m.\vec{y}'$. In the latter system, the position of the scatterer can also be expressed using polar coordinates as $x'_m = \rho_m.cos(\theta_m)$ and $y'_m = \rho_m.sin(\theta_m)$ so that the distance of the scatterer to the centre of rotation is given by $\rho_m = x'_m.cos(\theta_m) + y'_m.sin(\theta_m)$.

When the target rotates, the position of the scatterers varies in range. According to 2.24, the radial components of the vector position shift generates an instantaneous Doppler frequency shift, $f_D(t)$.

$$f_D(t) = \frac{2.\|\vec{\nu}\|}{c} f \tag{2.74}$$

where $\|\vec{\nu}\|$ is the radial velocity of a scatterer defined by its component $\vec{\nu}^t$ due to translation and it component $\vec{\nu}^r = \vec{\omega} \times \vec{r}$ due to rotation. For turntable measurements, the Doppler-frequency can be directly related to the scatterer-location in cross-range:

$$f_D = \frac{2f}{c} \omega_{eff}(t).r_c(t) \tag{2.75}$$

where ω_{eff} is the magnitude of the effective rotation vector that is perpendicular to the line of sight and r_c is the cross-range displacement.

Facilities

The set of turntable-measurements utilised in this thesis have been carried out on two different experimental systems by engineers from ENSIETA and CSIR. Located within an anechoic-chamber, the indoor-facility of ENSIETA

in Brest (France) enables radar measurement of small targets. For experiments on larger targets such as full-scale aircraft, measurements from the outdoor-facility at the Airforce Base Waterkloof in Pretoria (South-Africa) have been used.

- Specifications of the experimental system of ENSIETA
  - the radar antenna is located at 2 m in elevation
  - the centre of rotation of the turntable is located at 1.82 m in elevation and at $5.25m$ from the antenna.
  - the grazing angle is smaller than $\theta_g = 1.6°$
  - the radar system is based on a vector network-analyser
  - a dataset consists of 201 bursts from aspect-angle $\theta = -5°$ to 95°
  - a burst consists of 128 IQ samples at frequency $f_n = 11.95\ GHz$ to 18 GHz

Figure 2.8: Experimental system at ENSIETA

- Specifications of the experimental system of CSIR
  - the centre of rotation of the turntable is located at about 25 m from the antenna.
  - A dataset consists of bursts from aspect-angle $\theta = -30°$ to 30°
  - A burst consists of IQ samples from frequency $f_n = 0.3\ GHz$ to 18 GHz

Figure 2.9: Experimental system at CSIR

2.4.3 Radar imaging techniques

Introduction

Here, we are interested in showing a review of techniques for imaging targets. They include high-resolution range profiles, Radon images and ISAR images. The dataset employed has been obtained by turntable-measurement at ENSIETA. The target is composed of three spheres made of steel with a diameter of 50 mm. The scatterers are separated by 21.5 cm from each other.

High-resolution range-profiles

As shown earlier, High-Resolution Range-Profiles (HRRP) can be seen as the projection of the target reflectivity on the line of sight. They can be computed by Fourier-transforming a set of complex-valued radar samples obtained from one perspective.

In this example, measurements have been made for a target composed of three metal-spheres for an angular position of the turntable $\theta = 50°$. The image 2.10 represents the normalised power-spectra of the received signal for two different bandwidths: $B_{LR} = 3.175\ GHz$ (top) and $B_{HR} = 6.35\ GHz$ (bottom) starting at 11.95 GHz. Zero-padding has been applied to the data. The x-axis represents the range in metres.

On top, the 47mm-resolution image shows only two peaks. In order to distinguish the third peak, one has to increase the bandwidth. At the bottom, the 24mm-resolution image obtained with twice the bandwidth allows

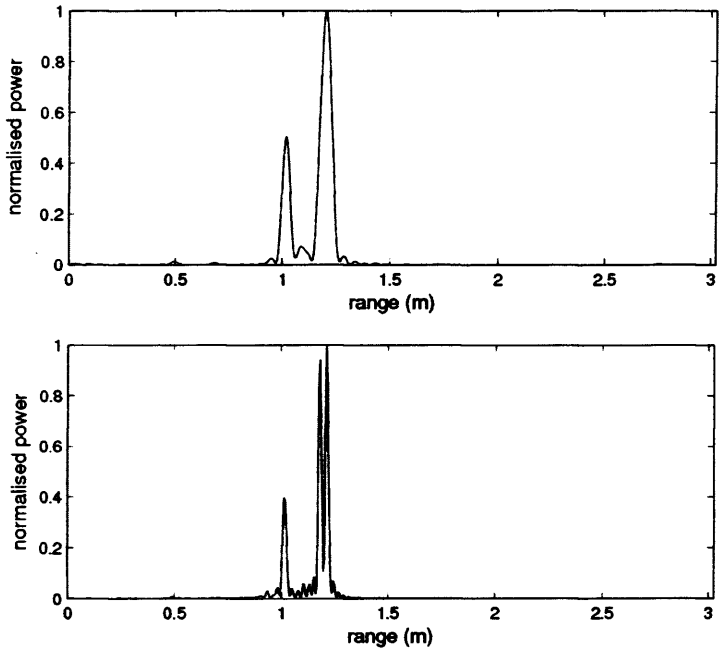

Figure 2.10: HRRP of three metal-spheres - $\Delta r = 47\ mm$ (top) and $\Delta r = 24\ mm$ (bottom), $\theta = 50°$ for $B = 6.35\ GHz$ (top) and $B = 11.95\ GHz$ (bottom)

resolution of the third scatterer. The range resolution required to distinguish the scatterers on a range profile depends upon their position in range. Positions vary with aspect-angle as can be seen on figure 2.11.

The rotation of the turntable allows measurements to be made for various aspect-angles. A two-dimensional dataset can be formed by collecting measurements at regular angles. Applying the method presented in the previous page, an image can be computed by Fourier transforming an array of complex-valued radar samples.

The example shown in figure 2.11 has been created by concatenating 201 range-profiles corresponding to aspect-angles $\theta = -5°$ to 95°. Each range profile has been obtained with the largest bandwidth (6.35 GHz). It therefore has a range-resolution $\Delta r = 24\ mm$. The x-axis represents the angle while the y-axis represents the range. Bright pixels correspond to large values of the power-spectrum.

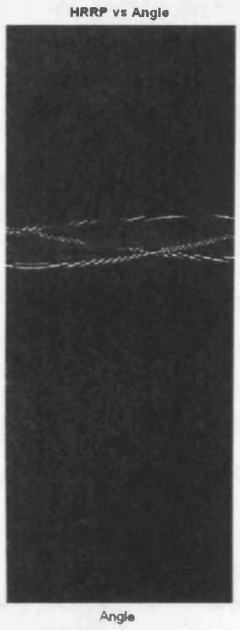

Figure 2.11: HRRP vs angle of three spheres: maximum range on y-axis $L = 3.024\ m$; range resolution $\Delta r = 24\ mm$, maximum angle on x-axis $\theta = -5°, -4.5°, \ldots, 95°$

The range of the scatterers is defined by cos-type functions with respect to aspect-angle. Depending on the aspect-angle, distinguishing the scatterers may require extremely high range-resolution. Hence the motivation for improving the cross-range resolution.

Inverse synthetic-aperture-radar

Inverse Synthetic-Aperture-Radar (ISAR) is a processing technique that images the reflectivity in two-dimensions: range and cross-range. Whereas the range to a scatterer is estimated by computing range-profiles, the cross-range is determined from the estimation of the Doppler frequency caused by rotation of the turntable in the example used here.

Let us assume a rotating target illuminated by a stepped-frequency radar. Stepped-frequency radar achieves waveforms with large effective bandwidth by emitting successive narrow-band pulses whose the carrier-frequency is sequentially increased. The transmitted waveform is typically a monochromatic signal whose duration corresponds roughly to the inverse of the desired narrow-bandwidth.

The concept of synthetic range profile generation [1] is summarised here and the technique used for computing ISAR images is represented below.

1. Transmit a series of N pulses in which the frequency is swept from pulse to pulse by a constant bandwidth, Δf, called the frequency step
2. Set a range-delayed sampling gate to collect I and Q samples of the target baseband echo response for each transmitted pulse (matched filter)
3. Store the quadrature components of each of the N echo signals. The complete set describes the frequency signature of the target's reflectivity
4. Rotate the target by a small angular step $\Delta\theta$
5. Repeat the above stages M times to synthesize both the bandwidth and the aperture.
6. Compute the inverse Discrete Fourier Transform (DFT^{-1}) of the set of N complex frequency samples to obtain the N complex components in the time domain per row.
7. Compute the Discrete Fourier Transform (DFT) of the resulting set of M complex time samples to obtain the M complex components in the Doppler domain per column.

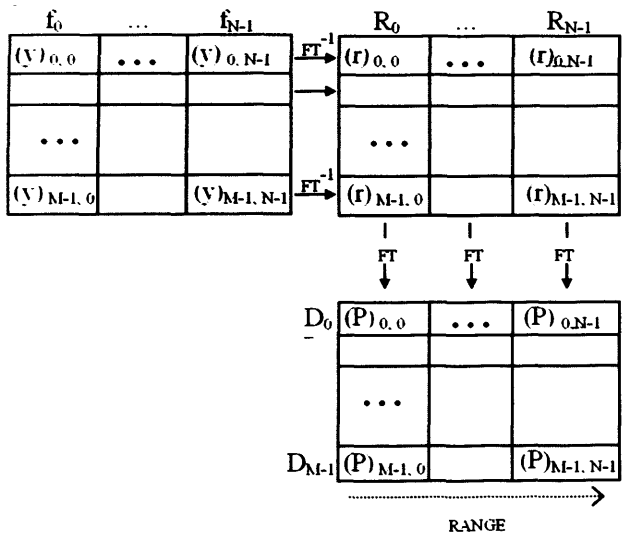

Figure 2.12: Principle of ISAR imaging

The I and Q samples collected during the measurements are organised in a two-dimensionnal array where each row corresponds to a different aspect-angle and each column to a different frequency. The first stage computes the Fourier transform of the row to create the M range-profiles. Each column is thus a time-history for one range-cell. Assuming the scatterers remains in the same range-cell, the second stage computes the Doppler content by Fourier processing the column. Images are then obtained by computing the power for each pixel. Although zero-padding does not improve the resolution, it can be used to interpolate images for enhancing the smoothness of the image.

In this example, an ISAR image is computed with radar data from the same set of complex-valued radar-measurements. The full 6.35 GHz bandwidth provides a range-resolution $\Delta r = 24\ mm$. In order to obtain a cross-range resolution $\Delta r_c = 24\ mm$, the aperture synthesized covers 24.5° from aspect-angles $-5°$ to 19.5°. The dimension of the imaged area are $3.024\ m \times 1.185\ m$. The resulting ISAR image is reproduced in figure 2.13

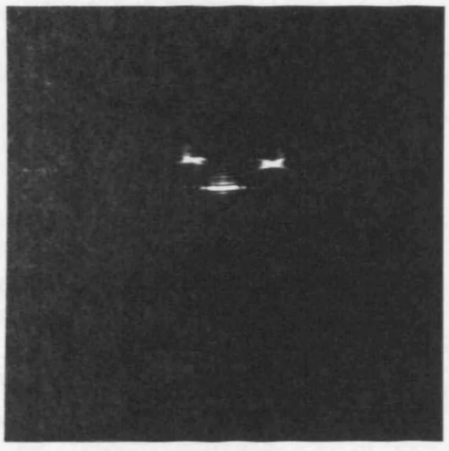

Figure 2.13: ISAR image of three metal-spheres: $L \times W = 3.024\ m \times 1.185\ m$, $\Delta r = \Delta r_c = 24\ mm$

ISAR imaging enables target characterisation to be made based on techniques that are close to human visual interpretation. However, accurate imaging requires motion compensation. This stage may be relatively easy to do for turntable measurement where the rotation vector is known. However, real targets may have a more chaotic motion including both rotation and translation.

2.4.4 Radar imaging limitations

Introduction

Radar imaging is achieved using techniques whose theory has been built with the assumptions of ideal targets and ideal radars. In the real-world, several factors may affect the quality of the images obtained. They can be related to the measurements, to non-ideal targets or the motion-compensation. Here we are interested in the limitations that may affect radar images .

Physical scatterers

Since the measurements are illuminating targets under different angles, the imaging methods must take into account the reflectivity as a function of angle. Individual scatterers may have a very complex structure and be characterised by impulse-responses that may greatly vary with aspect-angle. Non point-like targets are likely to vary from sphere-like targets. The effect of an irregular surface on the resolution is not considered.

To find an "equivalent" in frequency to the problem posed by complex surfaces, we need to imagine an articulated target composed of scatterers which independently move during the variation of signal phase, that is during the transmission of a pulse. The further the surface is from a sphere, the more chaotic and fast would be the motion.

The problem of moving-target compensation has been studied and is usually simplified to the case of rigid targets moving slowly and smoothly along a trajectory that can be estimated by taking into account the aerodynamic property of the existing target and a third-order polynomial model estimated directly by measurements from tracking radars. The performance of the compensation is limited by the ability to estimate target trajectory and by the ability to mathematically compensate for the effect of moving targets. This enables a focused image to be created in spite of the additional motion.

In the case of irregular surfaces, the direct estimation of the irregularity would be impossible by radar measurements. The more irregular the surface the more blurred the images. The surface irregularity can thus be considered as a limiting factor for the resolution of closely spaced scatterers in both range and cross-range. Resolving closely spaced targets that have irregular shapes could be more difficult in practice such as resolving micro-Doppler variation. For this reason it is important to use *a priori* information where possible. This is the idea behind matched-illumination.

Clutter

The signal at the receiver is created by direct echoes from the target but there is also a contribution from potentially large numbers of strong scatterers that are illuminated directly or indirectly by the radar. The discrimination between targets echoes and the other echoes is a difficult problem. However, it is a necessary one for constructing an accurate model.

2.4.5 Conclusion

In this chapter, we have shown that the target reflectivity function is estimated by comparing the returned radar signal with the transmitted one. When a coherent radar is used, precise information can be extracted as a function of phase. This information is then processed to obtain an image as a function of either the time of propagation and eventually Doppler frequency. Adding various assumptions about the scene reflectivity and variability in time, it is then possible to image the reflectivity as a function of space.

The signal bandwidth, the aperture and the validity of the assumptions made are key parameters to the image resolution, that is, the minimum distance between two point-scatterers that can be distinguished. Complex scattering mechanisms, and the presence of noise and clutter may affect the resolution. In the following, we are interested in a model-based technique that is used to enhance the resolution by extrapolating the bandwidth.

As the method relies on various assumptions, it is expected that the accuracy of the result varies with the target and its environment. The study presented in this thesis concerns the limitations of this technique when used to model extended man-made targets such as aircraft. Chapter 3 presents the theory behind the model and the technique. Chapter 4 is interested in its limitations, especially those arising from the inability of the technique to capture the information required for bandwidth extrapolation.

Chapter 3

SCATTERING-CENTRE MODEL ESTIMATION TECHNIQUES

3.1 Introduction

In this chapter we introduce the construction of scattering models based on their relationship with radar measurements. This is motivated by the fact that an accurate model describing the scattering mechanisms induced by a target constitutes a valuable source of information for radar imaging and non-cooperative target recognition. In addition, a model to interpolate the radar signal measured in discontinuous parts of the spectrum is also an attractive idea. Firstly, it would enable conventional techniques to process these signals with greater accuracy. Secondly, the capability to exploit sub-bands that are sparsely spaced makes radars more suitable for operating in environments where the large continuous bandwidths conventionally used for achieving high-resolution cannot be transmitted. Finally, this same capability can be used for extrapolating the bandwidth and enhancing the resolution. In our case, the model chosen has a physically intuitive structure directly inspired by the idea that only a few scatterers are responsible for most of the back-scattered signal. Whereas the complex-valued spectrum of the radar signal can be difficult to interpret, the model presents the information in a very meaningful way. The scattering-centre model describes a radar signal as a sum of elementary signals whose parameters depend upon the position, the geometry and the strength of the scatterers.

The estimation of the model requires extraction of precise and accurate information about the target. Conventionally, the Fourier-transform is used by spectral-estimation methods to provide a spatial representation of the target reflectivity function. However, the time (or range) resolution is limited by the recorded signal. By operating on a windowed spectrum, the results imply that the transfer-function outside the window is null. For most physical system, this assumption is incorrect. Therefore, the one-dimensional picture obtained by computing the Discrete Fourier-Transform only represents an estimate of the power spectral density (PSD). For stepped-frequency radar, the domain of integration corresponds to the bandwidth spanned by the returns measured at different frequencies; the larger the bandwidth, the better the range resolution.

In order to overcome the resolution limit imposed by the bandwidth, modern techniques, known as super-resolution algorithms, relying on *a priori* that knowledge can be employed. Many of them were developed during the last few decades. The principal algorithms include the covariance(or Prony) method, the Maximum Entropy (or Burg) method, CLEAN[1], Matrix Pencil, ESPRIT[2], MUltiple SIgnal Classication (MUSIC) and root-MUSIC. They are often less robust but more efficient than the conventional Fourier-based techniques. Whereas their performances are comparable for large sets of data, they present different statistical behaviours for smaller ones.

In this chapter, we concentrate on the construction of a scattering model from a radar-signal using super-resolution techniques that do not require estimation of an autocorrelation matrix. This choice is driven by the fact that the computation of this matrix is expensive and that the accuracy of the result has reliance upon the number of samples available. In addition, there exists more than one method by which this matrix can be estimated. In order to avoid this, the linear prediction techniques chosen here operate directly on the observation matrix. They include the Matrix Pencil and a modified root-MUSIC algorithm. Both are known to perform relatively well. The method presented in this chapter comes from the article initially published in the Lincoln Laboratory Journal in 1997 [12]. The model estimate achieves high-resolution imaging by accurate bandwidth extrapolation. It is the technique on which is built much of the analysis that follows in subsequent chapters.

This chapter is organised into three sections. First, it reviews the equations which lead to the creation of scattering models. Second, it presents the

[1]CLEAN reduces sidelobes induced artefacts by iterative estimation and suppression of the contribution of the strongest scattering centres to the signal, revealing the weakest ones.

[2]ESPRIT estimates the parameters of the scattering-centre model by manipulating the data array in such way that they become the solutions of two coupled eigenvalue problems.

technique used for modelling the data using a simulated signal. It provides an insight into the five stages dedicated to the estimation of the model-parameter values. Third, it demonstrates the technique's capability using a real signal backscattered from the metal spheres presented in Chapter 2.

3.2 Scattering

3.2.1 Introduction

In this section, we are interested in the interactions between wave and target. Starting with the general equation of scattering for the electromagnetic field, we present sophisticated forms of scattering models [6] that are derived from the theory of physical optics, geometrical optics and diffraction. In order to estimate the position of the scatterers from a set of radar data, the scattering model chosen must be suitable for being used by rather simple mathematical techniques. For this reason, we extend the approximation to the so-called scattering-centre model or Prony model whose simplest version is known as the point-scatterer model.

3.2.2 Scattering models

General equations

The scattering models are formed from the Helmholtz equation in 3.1.

$$\vec{\nabla}^2 H(\vec{x}) + k^2(1 + \varsigma(\vec{x}))H(\vec{x}) = 0 \tag{3.1}$$

where ς is the reflectivity function with support D and x is a space vector.

The field H can be written as the sum of an incident field and a scattered field $H = H_{inc} + H_{scatt}$. The solution to the direct problem is given by 3.2.

$$H_{scatt}(\vec{x}) = k^2 \int_{\mathcal{D}} G_k(\vec{x}, \vec{x}')\varsigma(\vec{x}')(H_{inc}(\vec{x}') + H_{scatt}(\vec{x}'))d\vec{x}' \tag{3.2}$$

where $G_k(\vec{x}, \vec{x}')$ is the free-space Green's function for the Helmholtz equation.

The scattered field at one part of the body depends upon the field scattered by neighbouring parts. An incident wave H_{inc} illuminating an elementary surface ∂D will generate currents $\vec{J}(\vec{x}, t)$ which are functions of space and time. These currents can propagate outside ∂D. Inversely, the energy scattered from ∂D is not restricted only to the energy incident upon this surface. Introducing the boundary conditions of a smooth-surface for

a perfect conductor into the Maxwell equations yields the equation for the scattered field, 3.4.

$$\vec{J}(\vec{x},t) = \hat{n} \times (\vec{H}_{inc}(\vec{x},t) + \vec{H}_{scatt}(\vec{x},t)) \quad (3.3)$$

$$= 2\hat{n} \times H_{inc}(\vec{x},t) + \hat{n} \times \frac{1}{2\pi} \int_{\partial\mathcal{D}}^{\diamond} \mathcal{L}\{\vec{J}\}(\vec{x}',t') \times \hat{r}.dS' \quad (3.4)$$

where $\int^{\diamond}$ is the principal value of the integral and $\mathcal{L}\{\vec{J}\}(\vec{x}',t')$ is defined by $\mathcal{L}\{\vec{J}\}(\vec{x}',t') = (r^{-2} + (rc)^{-1}\partial/\partial t')\vec{J}(x',t')$ with $r = |\vec{x} - \vec{x}'|$. The complexity of this expression can be reduced further by considering the weak scatterer assumption. It yields the physical optics model.

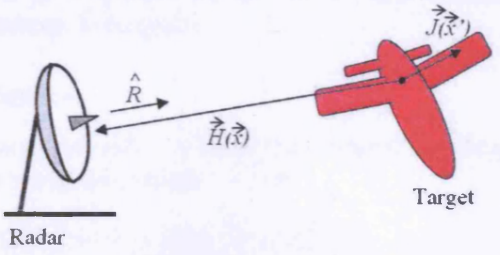

Figure 3.1: Propagation of currents on the illuminated target

Physical optics

When the indirect contributions to the current are weak, the support of integration is limited to ∂D and an approximate for $\vec{J}$ is given by $\vec{J}_{po}$ in 3.5

$$\vec{J}(\vec{x},t) \approx \vec{J}_{po}(\vec{x},t) = 2\hat{n} \times \vec{H}_{inc}(\vec{x},t) \quad (3.5)$$

Equation 3.6 represents the physical optics field obtained by integrating over the illuminated surface ∂D.

$$\vec{H}_{po}(\vec{x},t) = \frac{1}{4\pi} \int_{\partial\mathcal{D}}^{\diamond} \mathcal{L}\{\vec{J}_{po}\}(\vec{x}',t') \times \hat{R}.dS' \quad (3.6)$$

For an incident plane wave the physical optics far field approximation is given by 3.7. Figure 3.2 illustrates the idea of weak interaction between neighbouring surfaces.

$$\vec{H}_{po}(\vec{x},t;k) = -\frac{ik\vec{H}_0.e^{i(2kR-\omega t)}}{2\pi|\vec{R}|} \int_{\hat{R}.\hat{n}<0} \hat{R} \times \hat{n}.e^{i2k\hat{R}.\vec{x}'} dS' \quad (3.7)$$

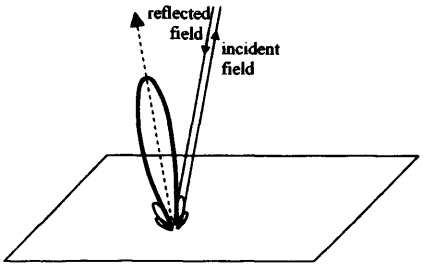

Figure 3.2: Physical optics

The latter can be simplified further under high-frequency conditions. It is then called geometrical optics.

Geometrical optics

When ∂D is smooth and k is large the integral can be evaluated by considering only the specular points on ∂D.

$$\vec{H}_{go}(\vec{x},t;k) = -\lim_{k\ large} \vec{H}_{po}(\vec{x},t;k) \tag{3.8}$$

$$= -\frac{ik\vec{H}_0.e^{i(2kR-\omega t)}}{2\pi|\vec{R}|}\sum_{<m>} A_m.e^{i2k\hat{R}.\vec{x}_m} + O(k^0) \tag{3.9}$$

Physically, 3.9 contains the idea that the signal backscattered can be approximated by a limited number of elementary signals associated with strong scatterers.

Geometrical theory of diffraction

In 1953, Keller introduced the geometrical optics theory of diffraction as an extension to geometrical optics to include edge and vertex diffracted rays. He then developed his theory for the field of rays diffracted from a perfectly conducting wedge. The method is known as the Geometrical Theory of Diffraction (GTD). It predicts that at high frequency, the incident field appears to originate from a discrete set of independent scattering-centres and follows a $(jk)^\alpha$ frequency dependence where α depends upon the target geometry. For an incident field that is an infinite plane wave, the model for the geometrical theory of diffraction is given by 3.10 [36]

$$E(f) = \sum_{m=1}^{M} A_m \left\{ j\frac{f}{f_c} \right\}^{\alpha_m} e^{-j\frac{4\pi f}{c}r_m} \tag{3.10}$$

where

- A_m is the complex amplitude associated with the reflectivity of the m^{th} scattering-centre,
- f frequency,
- f_c reference frequency,
- r_m relative location of the m^{th} scattering-centre,
- α_m frequency dependence parameter of the m^{th} scattering-centre.

For simple targets, the frequency dependence of canonical scattering geometries is given by the following table [37].

Surface type	**Example**	α
Corner reflector	Dihedral, plate	1
Singly curved	Cylinder	1/2
Doubly curved, straight edge	Spheroid	0
Curved edge	Circular disk	−1/2
Vertex	Cone tip	−1

The parameter α introduces the frequency dependence of the scatterers. There exists an approach, called the Simple Geometry Model approach, which exploits the parameter α for target classification. The technique considers that a complex target can be described as a structure of elements whose geometry can be used as a source of discriminating information.

Prony model

The Prony model is close to the GTD-based model in the sense that both assume contributions from independent scatterers with frequency dependence. The only difference is that Prony assumes an exponential frequency dependence while the GTD-based model assumes a power dependence [37].

For a discrete representation with frequency index n such that

$$f_n = f_0 + n.\Delta f, \quad n = 0 \cdots N-1 \tag{3.11}$$

the Prony model is given by 3.12

$$\begin{aligned} E(n) &= \sum_{m=1}^{M} A_m.p_m^n \\ &= \sum_{m=1}^{M} A'_m.\beta_m^{kn} e^{-j2r_m k_n} \end{aligned} \tag{3.12}$$

where: A_m is a complex-valued amplitude associated with the m^{th} scatterer, p_m is a pole whose angle is associated with the relative range r_m, and $k_n = 2\pi f_n/c$.

3.2.3 Conclusion

This section has shown that the scattering equations can be reduced to simpler forms depending on the level of approximation and the assumptions made. Although the general equations enable a very accurate prediction of the signal scattered by a given target, they are far too complicated to be used in the inverse problem. Instead, simple models that can be mathematically estimated from the signal at the receiver are preferred, but it is important when drawing any conclusion that their limitations are recognised.

For high-frequency waveforms, the currents induced on the surface of the target are assumed to be limited in space. Based on this assumption, theories can be used to decrease the complexity of the scattering equations. Adding the assumption of direct-path returns from strong backscatterers, the approximations lead to simple models that can be handled by various mathematical techniques created for model-estimation.

Amongst the various models presented here, the radar processing techniques found in the literature mostly employ Prony and GTD-based models. For scattering-centres with no frequency-dependent amplitude terms, both models are identical. This special case is known as the point-scatterer model. For more complex scattering behaviours, Prony-based algorithms are computationally less expensive than those which are GTD-based. In the following sections, we present a method for extracting the scattering-centres of the Prony model from a limited set of complex-valued narrow-band radar signals in the frequency domain.

3.3 Classic linear technique

3.3.1 Introduction

In this section, we introduce the basics of model-construction techniques using Prony's method. The initial algorithm created in the 18^{th} century, by the French mathematician Baron Gaspard Clair François Marie Riche de Prony, uses a linear sum of complex exponentials to represent signals that are uniformly sampled. The results can then be used to predict the signal by interpolation or extrapolation of the model. In radar, it can therefore be employed for estimating the parameters of the model defined by 3.12 from the signal at the receiver. This initial version has been revisited and improved recently in order to reduce the noise susceptibility.

3.3.2 Principle

In communication problems, the signal is in general assumed to be composed of two parts: the signal and the noise. In radar a similar approach is taken where it is assumed that the received waveform, x, is composed of a deterministic signal, s, corrupted by additivewhite Gaussian noise, u.

$$x(n) = s(n) + u(n) \tag{3.13}$$

Let us consider a complex-valued radar signal, $x(n)$, measured for N contiguous frequencies, f_n, as given by 3.11. Based on 3.13, the approach to the optimisation problem is to determine a model, $s(n)$, that minimises the Euclidian distance between the signal and the model, or equivalently the expression, $e(n)$, in 3.14 across the whole bandwidth.

$$e = \sum_{n=0}^{N-1} |x(n) - s(n)|^2 \tag{3.14}$$

where $|\bullet|$ represents the 2-norm.

3.3.3 Additive white Gaussian noise

The broad-band noise, $u(n)$, is described by its statistical properties:

$$\mathcal{E}\{u(n)u^*(n-m)\} = \begin{cases} \sigma_u^2, & m = 0 \\ 0, & m \neq 0 \end{cases} \tag{3.15}$$

where $\mathcal{E}(\bullet)$ is the expectation operator, $\bullet^*$ is the complex conjugate and σ_u^2 is the variance. The signal-to-noise ratio is defined by 3.16

$$SNR = 10.log_{10}\left(\frac{Power\ (s)}{Power\ (u)}\right) dB \tag{3.16}$$

3.3.4 High-frequency approximation

In the high-frequency region where most radar systems operate, it is often assumed that man-made targets can be accurately represented by a set of isolated scattering points. These scatterers generally correspond to discontinuities on the target. Due to structural similarities, scattering points on similar aircraft are principally located in the same areas. They principally include radomes, leading edges of wings and engine ducts. In addition to these general sources of scattering, there exist discontinuities which are more specific to individual aircraft such as cracks on the structures.

Let a target be composed of P scattering-centres. Providing there are no strong interactions between the scattering-centres, the signal, $s(n)$, could be approximated by a sum of P complex exponentionals.

$$s(n) = \sum_{p=1}^{P} a_p.z_p^n \tag{3.17}$$

where the complex coefficient, a_p, and the pole, $z_p = \rho_p.e^{i.\varphi_p}$, are associated with the reflectivity and the location of the p^{th} scattering-centre, respectively. Let us assume that amongst the P scattering-centres, M are much stronger than the others. In this case, the signal can be approximated with the contributions of M scatterers. It follows

$$\begin{aligned} s(n) &= \sum_{p=1}^{M} a_p.z_p^n + \sum_{p=M+1}^{P} a_p.z_p^n \quad P > M \\ s(n) &= s_1(n) + s_2(n) \approx s_1(n) \quad \forall(M,n)/\mathcal{P}ower(s_1) \gg \mathcal{P}ower(s_2) \end{aligned} \tag{3.18}$$

Figure 3.3 illustrates the concept of scattering-centres for an aircraft. Strong scatterers on the target are projected onto the direction of propagation of the beam, x.

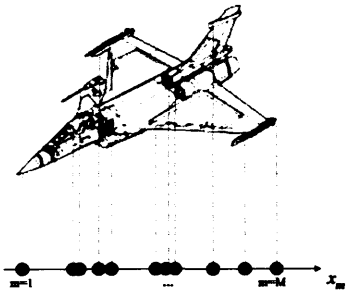

Figure 3.3: Concept of scattering-centres in one-dimensional imaging on the fighter-aircraft Rafale - courtesy SIRPA AIR [2]

3.3.5 The autoregressive model

Many representations of the data-process have been proposed. In radar, the most widely applied class of finite parametric models is the autoregressive (AR) process.

Let us consider the radar return in 3.13. The autoregressive model describes a signal generated by a system excited by white noise. The data at the output $x(n)$ are assumed to be related to the past output data and to the input data $u(n)$. The AR process is represented by equation 3.19.

$$x(n) - \sum_{q=1}^{Q} c_q.x(n-q) = u(n) \tag{3.19}$$

in which Q is the model-order and c_q are the autoregressive coefficients [22].

The corresponding rational transfer-function $\mathcal{H}(z)$ given by 3.20

$$\mathcal{H}(z) = \frac{1}{\mathcal{A}(z)} = \frac{1}{1 - \sum_{q=1}^{Q} c_q.z^{-q}} \tag{3.20}$$

where the Q roots of $\mathcal{A}(z)$ are the poles of the system. For this reason the model is also called the all-pole model.

3.3.6 The least-squares Prony model

The Least-Squares Prony is a classic polynomial technique for determining the parameter of a linear combination of exponential functions. Tufts *et al.* [24] describe the generalised Prony algorithm as follows:

1. Using the method of Least-Squares, minimise the approximation error

$$e = \sum_{n=Q+1}^{N-1} |x(n) - \sum_{q=1}^{Q} \hat{c}_q.x(n-q)|^2 \tag{3.21}$$

by the best choice of coefficients $\hat{c}(q)$ where $\hat{}$ denotes the estimated value here.

The necessary condition for the minimum of e is given by the orthogonality principle:

$$\sum_{n=Q+1}^{N-1} \left[x(n) - \sum_{q=1}^{Q} \hat{c}_q.x(n-q) \right] x^*(n-m) = 0 \quad for\ m = 0 \cdots L-1 \tag{3.22}$$

In theory, the orthogonality principle requires an infinite length of stationary process data.

2. For $Q = P$, the autoregressive coefficients in 3.19 are unique. If there is no measurement noise, then the poles of $\mathcal{H}$ correspond to the poles of a Prony model representing P scatterers. Consequently after the Q coefficients c_qs are determined, the roots of the forward prediction error (PEF) polynomial, $\mathcal{A}(z)$, are found by 3.23:

$$\mathcal{A}(z) = 1 - \sum_{p=1}^{P} \hat{c}_p.z^{-1} = \prod_{p=1}^{P}(1 - \hat{z}_p z^{-1}) \tag{3.23}$$

The accuracy of the $\hat{z}_p$ value can be improved by using a PEF with an order $Q > P$. In this case, there are extra noise-subspace roots of the PEF polynomial. The P true roots must be extracted from the $Q - P$ extraneous noise roots.

3. Having determined the pole estimates of the signal roots z_p for $p = 1 \cdots P$, the amplitude terms can be estimated by solving a linear least-squares problem:

$$e(n) = x(n) - \sum_{p=1}^{P} \hat{a}(p).\hat{z}^n(p) \tag{3.24}$$

In principle, one only needs P equations to compute $\hat{a}_p$. However, because the P autoregressive coefficients are determined by the least-squares approach, the method suffers from hypersensitivity resulting in the modelling of the noise components.

The estimated autoregressive coefficients $\hat{c}_q$ in 3.20 can be utilised to predict the estimate sample $\hat{x}(n)$ of $x(n)$ by the following relation with the model-order Q equal to the number of scatterers P.

$$\hat{x}(n) = \Sigma_{q=1}^{Q} c_q.x(n - Q + q) \tag{3.25}$$

3.4 Scattering-centre extraction

3.4.1 Introduction

In 1795, Prony developed a polynomial-based prediction method for modelling a sum of complex exponential signals [13]. The introduction of Least-Squares methods in the 1970's enables accurate pole extraction to be achieved more efficiently. However, these algorithms are also extremely sensitive to the noise. In 1978, Kung introduced a state-space method for harmonic-retrieval directly from the data [25]. The eigenvectors of the autocorrelation matrix are obtained by singular-value-decomposition (SVD) rather than by computing the autocorrelation matrix itself. Four years later, Tufts and Kumaresan developed the principle for estimating the parameters of exponentially damped sinusoids [49]. This eigenvector method (or principal eigenvalue method) reduces the effect of noise by only using the set of eigenvectors that constitute a basis for the signal subspace. For low signal-to-noise ratios, these methods are known to perform better than any other method based on Least-Squares approach. In 1987, a new version of the Prony method was proposed by Rahman and Yu, Total Least-Squares (TLS-Prony) [39]. An alternative to these polynomial methods commenced with the creation of more recent techniques such as ESPRIT [34] and Matrix Pencil [17]. Based on the Generalised-Eigenvalue approach, they also achieve accurate linear prediction for low signal-to-noise ratio conditions.

In this section, we are interested in a linear prediction technique that relies on the construction of a scattering model defined as a finite sum of complex exponentials, known as cisoids. The technique is employed to demonstrate that a scattering model can improve radar range-resolution. Firstly, the signal backscattered from three simulated spheres is modeled by three point-scatterers. Secondly, the model is determined by a linear-prediction technique, which consists of five processing stages:

1. model-order estimation
2. pole determination
3. pole selection
4. amplitude coefficient estimation
5. parameter adjustment

The model is then extrapolated across a large bandwidth. Whereas the initial signal can only generate two peaks on the range-profile, the extrapolated model enables the third to be resolved. Several algorithms can be used for computing each stage. This section offers an insight into some of them.

3.4.2 Radar signal

In this section, we illustrate the theory by using a radar signal backscattered by a simulated target consisting of three identical spheres located at range $R_0 + r_k$ from the radar where R_0 corresponds to the start of the imaging window and r_k is the range of the k^{th} scatterer relatively to R_0. The deterministic signal is simulated by the Prony model in 3.27.

$$s(n) = \sum_{k=1}^{3} e^{\frac{i2\pi.f_n.2(R_0+r_k)}{c}} = \sum_{k=1}^{3} e^{\frac{i4\pi.f_0.(R_0+r_k)}{c}}.e^{\frac{i4\pi.(\Delta f.n).(R_0+r_k)}{c}} \quad (3.26)$$

$$= e^{\frac{i4\pi.f_0.R_0}{c}}.\sum_{k=1}^{3} e^{\frac{i4\pi.f_0.r_k}{c}}.e^{\frac{i4\pi.(R_0+r_k).\Delta f.n}{c}} \quad (3.27)$$

Replacing $R_0 = 5.25\ m$, $r_1 = 10\ cm$, $r_2 = 13.5\ cm$, $r_3 = -0.10\ cm$ and $f_n = 11.65 + 0.05.n$ (GHz) into 3.27 follows 3.28

$$\begin{aligned} s(n) = \ & (\ -0.9945 - i.0.1045).e^{-i.1.3614.n} + \\ & (\ 0.0941 + i.0.9956).e^{-i.1.2881.n} + \\ & (\ 0.9945 - i.0.1045).e^{-i.1.7802n} \end{aligned} \quad (3.28)$$

The simulated signal is corrupted by Additive White Gaussian Noise ; the signal-to-noise ratio is defined by 3.29

$$SNR = 10.log\left(\frac{Power(Signal)}{Power(Noise)}\right) = 30\ dB \quad (3.29)$$

Figure 3.4 shows the simulated real-valued radar samples, $x_I(n)$, from the I-channel.

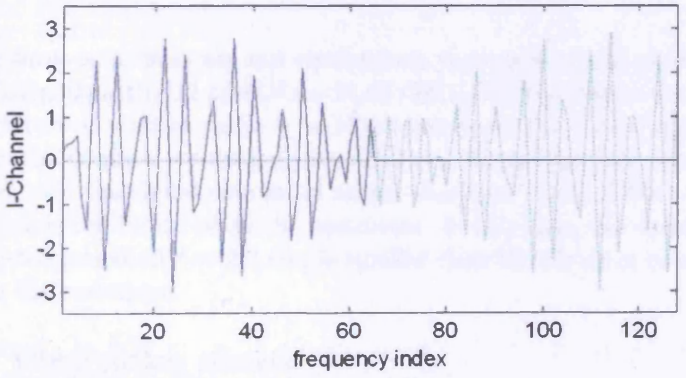

Figure 3.4: I-channel - sub-band 1 (solid-line) - subband 2 (dashed-line) - $SNR = 30\ dB$

The first 64 samples (solid line) of the sub-band [11.65 GHz−14.85 GHz] are used to build the model. The 64 samples (dotted line) of the sub-band [14.85 GHz − 18 GHz] are only presented for information.

Figure 3.5 shows the range-profile obtained by taking the IFFT of the first 64 complex samples (top) and by taking all 128 samples (bottom).

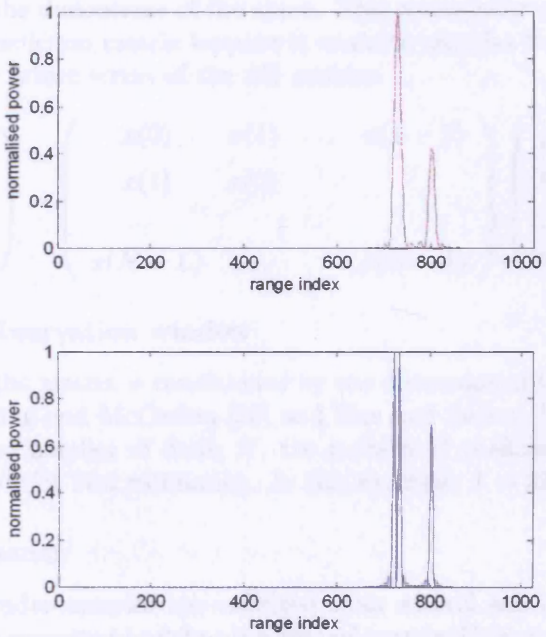

Figure 3.5: HRRP - range window $R = 3\ m$ - $B = 3.2\ GHz$ (top) and $B = 6.4\ GHz$ (bottom) - $SNR = 30\ dB$

The three scatterers are not resolved on the range-profile obtained with 3.2 GHz-bandwidth, [11.65 GHz − 14.85 GHz]. This is due to the fact that the scatterers at relative range $r_1 = 10\ cm$ and $r_2 = 13.5\ cm$ are separated by less than the nominal resolution, $\Delta r = 4.7\ cm$. In contrast, the range-profile obtained with the signal simulated across the band [11.65 GHz − 18 GHz] would enable resolution of all the scatterers. In this case, the corresponding nominal-resolution, $\Delta r' = 2.3\ cm$, is smaller than the distance of separation between the scatterers.

3.4.3 Observation matrix

Here, we present a technique that can resolve the three scattererers by only using the first 64 samples of the 128 available. Rather than computing the autocorrelation-matrix, the method relies on the mathematical properties of

the Hankel matrix. Given the values of $x(n)$ for N frequencies, such matrix is obtained by implementing the autoregressive model in 3.19 for $N - L$ equations.

$$\vec{X} = H.\vec{C} \tag{3.30}$$

The observation matrix H formed by N complex-valued samples arranged in a quasi-symmetrical manner has constant skew diagonals; the parameter L determines the dimensions of the space. This rectangular matrix is called the forward-prediction matrix because it contains samples that are used for estimating the future terms of the AR process.

$$\begin{pmatrix} x(L) \\ x(L+1) \\ \vdots \\ x(N) \end{pmatrix} \approx \begin{pmatrix} x(0) & x(1) & \dots & x(L-1) \\ x(1) & x(2) & & \vdots \\ \vdots & & \ddots & \\ x(N-L) & \dots & & x(N-1) \end{pmatrix} \begin{pmatrix} c_L \\ c_{L-1} \\ \vdots \\ c_1 \end{pmatrix} \tag{3.31}$$

Size of the observation window

The size of the matrix is conditioned by the dimension of the observation window, L. Lang and McClellan [26] and Hua and Sarkar [17] recommend that for a fixed number of data, N, the number of coefficients chosen be $N/3 < L < N/2$ for best estimation. In this example, $L = 22$.

Sparse sub-bands

When the radar-samples are collected from several sub-bands, the authors of [12] recommend building the Hankel matrix H from the individual observation matrices H_i formed using the radar samples in each sub-band. For example, the observation matrix obtained using two different sub-bands would be built from the matrices H_1 and H_2 as follows:

$$H = \begin{pmatrix} H_1 \\ H_2 \end{pmatrix}$$

Singular-value decomposition

The matrix H can be decomposed into the product of three matrices by singular-value-decomposition (SVD).

$$H = U.\Sigma.V^H \tag{3.32}$$

where $\bullet^H$ denotes the Hermitian transpose. The unitary matrices U and V have orthogonal columns. Σ is a diagonal matrix containing the L singular values, σ_i, sorted in decreasing order.

$$\Sigma = \begin{pmatrix} \sigma_0 & 0 & \dots & 0 \\ 0 & \sigma_1 & & \vdots \\ \vdots & & \ddots & 0 \\ 0 & \dots & 0 & \sigma_{L-1} \end{pmatrix} \tag{3.33}$$

where the singular values σ_i are the square-roots of the estimated correlation matrix HH^H or H^HH.

The SVD generates two families of dual eigenvectors $\vec{u}$ and $\vec{v}$ from the following coupled equations:

$$\begin{aligned} HH^H.\vec{u} &= \lambda\vec{u} \\ H^HH.\vec{v} &= \lambda\vec{v} \end{aligned} \tag{3.34}$$

Asymptotically, the columns of the square matrices U and V are the eigenvectors of HH^H and H^HH, respectively. The left and right singular matrices U and V can be written as a set of columns $\vec{u_i}$ and $\vec{v_i}$, respectively :

$$\begin{aligned} U &= \{\vec{u}_0, \vec{u}_1, \dots, \vec{u}_{L-1}\} \\ V &= \{\vec{v}_0, \vec{v}_1, \dots, \vec{v}_{L-1}\} \end{aligned} \tag{3.35}$$

3.4.4 Rank deficiency

Considering a corrupted signal $x(n)$ composed of the sum of P complex sinusoids in complex white noise, the autocorrelation matrix R_{xx} is the sum of the signal autocorrelation matrix R_{ss} and the noise autocorrelation matrix $R_{uu} = \sigma_u^2 I$ where I is the identity matrix.

$$R_{xx} = \sum_{i=0}^{P-1} A_i^2.\vec{e}_i\vec{e}_i^H + \sigma_u^2 I \tag{3.36}$$

where $\vec{e}_i = [1 \quad exp(j\varphi_i) \dots exp(j\varphi_i(P-1))]^T$

The estimated autocorrelation matrix 5.6 can be decomposed into

$$R_{xx} = \sum_{i=0}^{P-1} (\lambda_i + \sigma_u^2)\hat{v}_i\hat{v}_i^H + \sum_{i=P}^{L-1} (\sigma_u^2)\hat{v}_i\hat{v}_i^H \tag{3.37}$$

where $\hat{v}_i$ are the eigenvectors and λ_i are the eigen-values of the estimated signal autocorrelation matrix R_{xx}. The matrix R_{ss} is not full rank since its dimensions are generally greater than the rank P. Nevertheless, in practice matrix R_{xx} is full rank due to the presence of noise.

3.4.5 Subspace decomposition

Let us assume that the values of L and $N-L$ are both much greater than the number of scattering-centres P. The Hankel matrix H comprises two orthogonal subspaces because it is realised from the complex-valued radar samples containing the uncorrelated $P(< L)$ signals and white noise. This is illustrated by figure 3.6 .

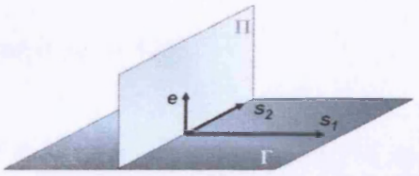

Figure 3.6: Concept of orthogonal sub-spaces

Using time-series theory, subspace-decomposition may be employed as a way to separate the signal from the noise. Assuming there is no noise, the expression of $x(n)$ is reduced to $s(n)$ in 3.13. Although this case is purely theoretical, it helps understanding the principle of subspace-decomposition. The rank of the Hankel Matrix H is P and therefore Σ contains P non-null singular values. The $L \times L$ matrix Σ can then be written as follows:

$$\Sigma = \begin{pmatrix} \Sigma_s & 0 \\ 0 & 0 \end{pmatrix} \tag{3.38}$$

where Σ_s is a diagonal matrix containing the P singular-values associated with the components of the signal in 3.39.

$$\{\sigma_0 < \sigma_1 < \cdots < \sigma_{P-1}\} \tag{3.39}$$

The singular-values correspond to the variance of the eigenvectors. For high SNR, it follows that the weakest $L-P$ singular-values are directly related to the smallest eigen-values and to the power of the noise in 3.13.

$$\lambda_i = \sigma_i^2 = (N-L)\sigma_u^2, \quad i = P \ldots L \tag{3.40}$$

The matrix Σ can be written as follows:

$$\Sigma = \begin{pmatrix} \Sigma_s & 0 \\ 0 & \Sigma_n \end{pmatrix} \tag{3.41}$$

where Σ_n is a diagonal matrix containing the $L-P$ singular values associated with the noise, in 3.42.

$$\{\sigma_P < \sigma_{P+1} < \cdots < \sigma_{L-1}\} \tag{3.42}$$

In a similar way, the basis of the eigenvectors that constitute the columns of U and V can be split into two parts. The sets of columns (or eigenvectors) defined by V_s and V_n would span the signal-subspace and noise-subspace, respectively. The expression for U and V are given by 3.43.

$$\begin{aligned} U &= \{U_s, U_n\} = \{(\vec{u}_0, \ldots, \vec{u}_{P-1}), (\vec{u}_P, \ldots, \vec{u}_{L-1})\} \\ V &= \{V_s, V_n\} = \{(\vec{v}_0, \ldots, \vec{v}_{P-1}), (\vec{v}_P, \ldots, \vec{v}_{L-1})\} \end{aligned} \tag{3.43}$$

3.4.6 Model-order selection

Introduction

The model-order is the number of terms in the model used by linear-prediction methods. Here, the model-order of the autoregressive process corresponds to the number of scattering-centres, P, that contribute to the signal. Estimating the model-order is needed for building the model. Even if the number of targets is known, the model-order has to be estimated because the enhanced resolution may increase the number of scattering-centres that may become relevant.

Singular-values

It is possible to estimate the model-order by exploiting the multiplicity of the eigen-values in 3.40 that are related to the noise. Here, the eigen-values are estimated by singular-value-decomposition (SVD) of the matrix H, as defined in 3.32. Because the singular-values are directly related to the eigen-values, the $L - P$ smallest singular-values, 3.42, should have small and almost identical values related to the power of the noise.

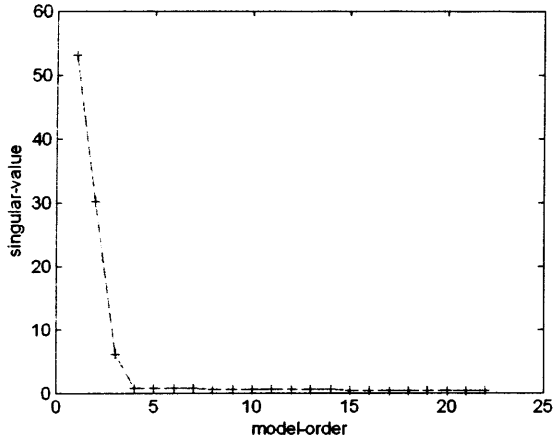

Figure 3.7: Model-order estimation - $P = 3$, $N = 64$, $L = 22$, $SNR = 30\ dB$

Figure 3.7 represents the singular-values extracted from the first 64 complex-valued radar-signals in 3.4. For $L = 22$, the nineteen weakest singular-values, directly related to the power of the noise, can be easily identified. For $SNR = 30\ dB$, the transition between groups of singular-values suggests that the model-order is $P = 3$.

Model-fitting theory

Another approach for estimating the model-order uses the general model-fitting theory. For modelling a signal, a measure of accuracy can be obtained by computing the distance between the signal, $x(n)$, and the model, $\hat{s}(n)$ using the mean-square error. In this case, the greater the model-order, the smaller the error. This can be explained by the fact that models with high orders are modelling not only the signals but the noise as well. In order to determine the model-order needed to model the deterministic component, $s(n)$, it is possible to refer to information theory.

Wax and Kailhath adapted two criteria, Akaike Information Criterion (AIC) [50] and Minimum Description Length (MDL) [42]:

- Akaike Information Criterion

$$\Lambda(k)_{AIC} = -2.ln(\frac{\prod_{i=k+1}^{L} \lambda_i^{\frac{1}{L-k}}}{\frac{1}{L-k}\sum_{i=k+1}^{L} \lambda_i}) + 2k.(2L-k) \tag{3.44}$$

- Minimum Description Length

$$\Lambda(k)_{MDL} = -ln(\frac{\prod_{i=k+1}^{L} \lambda_i^{\frac{1}{L-k}}}{\frac{1}{L-k}\sum_{i=k+1}^{P} \lambda_i}) + \frac{1}{2}.k.(2L-k).ln(N) \tag{3.45}$$

where N is the number of samples in the observation-matrix, L is the width of the observation matrix, λ_i are the smallest eigen-values.

The model-order estimate, P, is the value of k that minimises the expression Λ. Figure 3.8 illustrates the principle used to estimate the model-order using the same parameters as those used to generate figure 3.7. Here the minimum value of Λ is obtained for $k = 3$. The model-order is then estimated at $P = 3$.

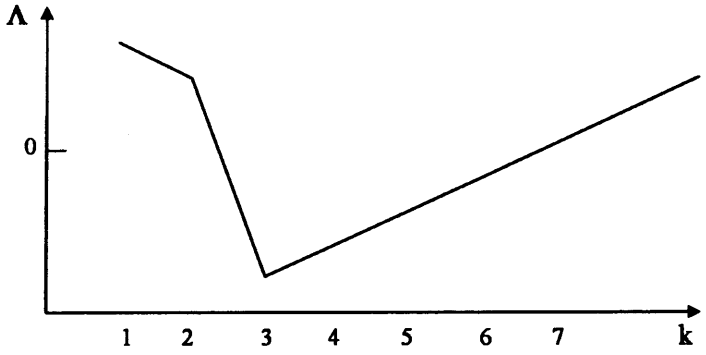

Figure 3.8: Concept of model-order estimation based on information theory - $P = 3$

3.4.7 Pole determination

So far, it has been assumed that the signal associated with the k^{th} scattering-centre can be defined by the k^{th} component of the Prony model given in 3.46:

$$s_k(n) = a_k.p_k^n \tag{3.46}$$

The complete construction of the model requires determination of the value of the amplitude coefficients a_k and those of the poles p_k for every scattering-centre. These terms form the so-called feature vectors of the targets and can be used for NCTR as will be shown in Chapter 5.

Here, we examine two linear-prediction methods based on the super-resolution algorithms root-MUSIC and Matrix-Pencil. The first one is based on a polynomial approach. It exploits the structure of the autoregressive equation to determine the poles. The algorithm used is a modified version of the original root-MUSIC. It was used by Cuomo *et al.* in [12]. The second method is called the Matrix Pencil (MP) [17]. This more recent method is also known as "generalised pencil of functions" (GPOF) due to the fact that it determines the poles by solving a generalised eigen-value problem.

MUSIC

The MUltiple SIgnal Classification (MUSIC) algorithm [45] initialy conceived for angular spectrum estimation, can also be used here for locating the poles in the z-plane. This principle was developed by Schmidt in 1997 and by Bienvenu ealier the same year [5]. The eigenvectors $\vec{u}$ or $\vec{v}$ form a basis for the signal and for the noise. The orthogonality of the eigenvectors is exploited for separating the signal subspace defined by the principal components from the the noise subspace. The MUSIC spectral estimator is written as 3.47 [22]

$$\mathcal{P}_{MUSIC} = \frac{1}{\sum_{i=P+1}^{L} |\vec{e}^H \hat{v}_i|^2} \tag{3.47}$$

where $\hat{v}_i$ are the eigenvectors of the estimate correlation matrix R_{SS}. The denominator may be expressed as

$$\mathcal{P}_{MUSIC}{}^{-1} = \vec{e}^H \sum_{i=P+1}^{L} \hat{v}_i \hat{v}_i^H \vec{e} \tag{3.48}$$

Eq 3.48 can be seen as the projection of the vectors $\vec{e} = [1\ z^{-1}\ \ldots\ z^{-L+1}]$ onto the noise subspace, as defined by the basis of eigen-vectors $\hat{v}_i$. Theoretically, when $\varphi = \varphi_i$, so that $\vec{e} = \vec{e}_i$, the denominator is null. For vectors that are perpendicular to the noise, $\mathcal{P}_{MUSIC} \rightarrow \infty$

The standard MUSIC algorithm provides a spectral estimate whose peaks are associated with the pole estimates. Figure 3.9 represents the pseudospectrum obtained by applying the MUSIC algorithm to the signal.

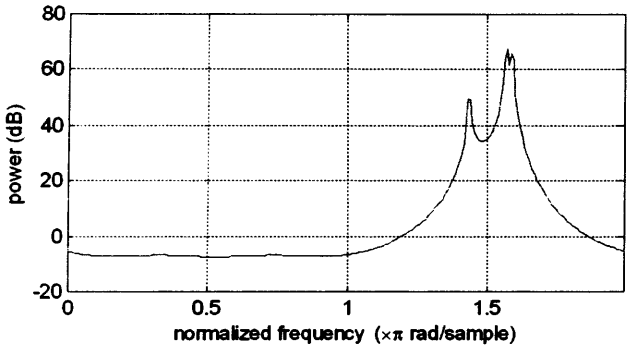

Figure 3.9: MUSIC pseudospectrum - $P = 3$

The presence of three peaks shows the resolution enhancement obtained using the MUSIC algorithm. The range of the three scatterers can again be determined by the position of the peaks. A closely related version of MUSIC, known as root-MUSIC, can estimate these parameters directly.

Modified root-MUSIC

The root-MUSIC algorithm, consists of determining the poles by rooting a polynomial. In the modified Fast-root-MUSIC proposed by Ren [40], the estimation of the poles starts by computing the projection matrix onto the noise subspace, A, as follows.

$$A = \hat{V}_n.\hat{V}_n^H \tag{3.49}$$

and constructing the polynomials $\mathcal{A}(z)$ given in 3.50:

$$\mathcal{A}(z) = \sum_{i=1}^{L} a_i z^{i-1} \tag{3.50}$$

where a_i denotes the elements of the first row of A

The roots of $\mathcal{A}(z)$ correspond to the pole estimates. However, due to the size of the observation window, the number of roots, L, is generally greater than the model-order P. We assume the model-order smaller than the number of poles so that true roots must be selected.

Figure 3.10 represents the poles of H determined by the modified root-MUSIC algorithm for $N = 64$ and $L = 22$. The twenty-one poles z_k are evently spread along the unit-circle and the three poles representing the model lie clearly on the unit-circle.

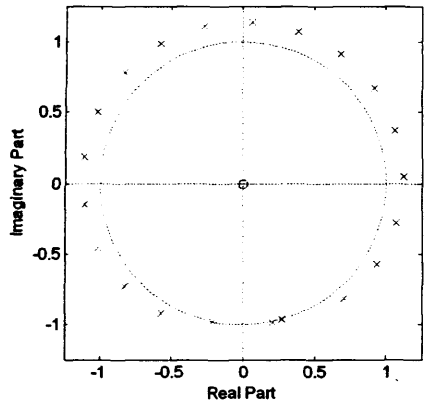

Figure 3.10: Z-plane - poles obtained with the modified root-MUSIC algorithm - $N = 64$, $P = 3$, $L = 22$, $SNR = 30\ dB$

Matrix pencil

This section concerns an alternative technique known as the Matrix-Pencil [17]. Unlike linear-prediction methods based on polynomial rooting, the Matrix Pencil method solves a generalised eigen-value problem. The techniques can also exploit subspace-decomposition and the rank-deficiency of Hankel matrices. The following presents the principle of SVD Matrix-Pencil for the extraction of cisoids [18] [44].

The matrix pencil is a linear combination of two matrices, $H_1 - z.H_2$ where H_1 and H_2 are formed from the prediction matrix H presented in 3.31.

$$H_1 = \begin{pmatrix} x(0) & x(1) & \dots & x(L-2) \\ x(1) & x(2) & & \vdots \\ \vdots & & \ddots & \\ x(R-1) & \dots & & x(N-2) \end{pmatrix} \tag{3.51}$$

$$H_2 = \begin{pmatrix} x(1) & x(2) & \dots & x(L-1) \\ x(2) & x(3) & & \vdots \\ \vdots & & \ddots & \\ x(R) & \dots & & x(N-1) \end{pmatrix} \tag{3.52}$$

where L is the pencil parameter that determines the dimensions of the space.

The matrices can be decomposed as follows:

$$H_1 = Z_1.B.Z_2 \tag{3.53}$$

$$H_2 = Z_1.B.Z_0.Z_2 \tag{3.54}$$

where

$$Z_1 = \begin{pmatrix} 1 & 1 & \dots & 1 \\ z_1 & z_2 & \dots & z_M \\ & & \dots & \\ z_1^{N-L-1} & z_2^{N-L-1} & \dots & z_M^{N-L-1} \end{pmatrix} \tag{3.55}$$

$$Z_2 = \begin{pmatrix} 1 & z_1 & \dots & z_1^{L-1} \\ & & \dots & \\ 1 & z_M & \dots & z_M^{L-1} \end{pmatrix} \tag{3.56}$$

and

$$Z_0 = diag[z_1, z_2, \dots, z_M] \tag{3.57}$$

$$B = diag[b_1, b_2, \dots, b_M] \tag{3.58}$$

where $diag[\bullet]$ denotes a $M \times M$ diagonal matrix.

The matrix pencil can then be written

$$H_2 - z.H_1 = Z_1 B(Z_0 - zI)Z_2 \tag{3.59}$$

where I is the $M \times M$ identity matrix.

Each observation matrix can be decomposed into a signal matrix, S, and a perturbation matrix, E. The pencil of the matrix can be decomposed as a sum of signal and noise matrices, S and E, respectively. It follows that a new expression of the pencil of matrix is given in 3.61.

$$\begin{aligned} H_1 - zH_2 &= (S_1 + E_1) - z(S_2 + E_2) && (3.60) \\ &= (S_1 - zS_2) + (E_1 - zE_2) && (3.61) \end{aligned}$$

In 3.61, S_1 and S_2 have the same column space and the same row space. One can demonstrate that the rank of the matrix pencil will be M, provided that $M < L < N - M$. However, if $\{z = z_i; i = 1, \ldots, M\}$, the i^{th} row of $(Z_0 - zI)$ is zero, and the rank of this matrix is $M - 1$. In other words, the noiseless pencil $S_1 - z.S_2$ decreases its rank by one if and only if z is one of the generalised eigen-values (GE) of $H_1 - z.H_2$.

Hence, we know the poles are the generalised eigen-values of the matrix pair $[H_1; H_2]$. However, the direct computation of the GE is not stable because S_1 and S_2 are not full rank. It is common to replace the matrices H by their truncated SVD's. The truncated versions are denoted by H_{1T} and H_{2T} and $\mapsto$ denotes the rank-P SVD truncation.

$$\begin{aligned} H_1 &\mapsto H_{1T} = U_1 \Sigma_1 V_1^H && (3.62) \\ H_2 &\mapsto H_{2T} = U_2 \Sigma_2 V_2^H && (3.63) \end{aligned}$$

where U_1, Σ_1 and V_1 only contain the P principal elements.

Replacing the truncated matrix into the matrix pencil yields

$$H_{1T} - z.H_{2T} = U_2^H U_1 \Sigma_1 V_1^H V_2 - z\Sigma_2 \tag{3.64}$$

The poles can be estimated by computing the eigen-values of 3.64 or equivalently the eigen-values of 3.65.

$$\Sigma_2^{-1} U_2^H U_1 \Sigma_1 V_1^H V_2 = [H_{2T}^H H_{1T}]^{-1} [H_{1T}^H H_{2T}] \tag{3.65}$$

Figure 3.11 represents the poles of H determined by the Matrix Pencil.

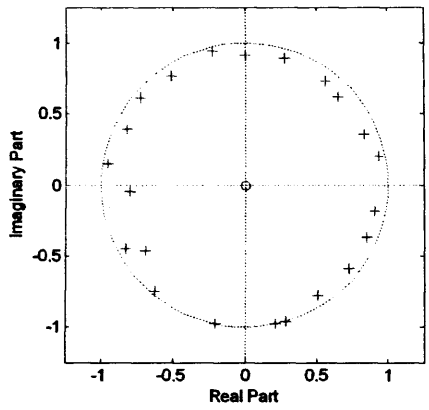

Figure 3.11: Z-plane - poles obtained with the Matrix Pencil algorithm - $N = 64$, $P = 3$, $L = 22$, $SNR = 30\ dB$

3.4.8 Pole selection

Regardless of the method chosen, the set of poles computed always comprise poles that are not associated with any physical scattering centres. It is thus essential that only "true poles" be selected and inserted in the model. For this, we consider that the frequency dependence of the signal-components associated with the scattering-centres is small whereas the contribution of spurious poles is very widely distributed in range. This is the basis for pole selection. The spatial distribution of the scattering-centre is related to the magnitude ρ_k of the pole estimated for that centre. If p_k is too far from the unit-circle then its contribution to the frequency model is greatly different at frequency f_0 and at frequency f_{N-1}. So, the true poles are the P poles whose modulus is close to one, that is those lying on the unit-circle.

For an unknown number of scattering-centres, Carriere and Moses suggest a criterion for discarding spurious poles [10]:

$$\frac{1}{100} < |p^N| < 100 \tag{3.66}$$

Expressions 3.67 and 3.68 are numerical examples of boundaries for 64 and 128 samples.

$$0.93 < |p| < 1.07, \quad N = 64 \tag{3.67}$$

$$0.96 < |p| < 1.03 \quad N = 128 \tag{3.68}$$

Figure 3.12 shows the poles selected using the above criterion.

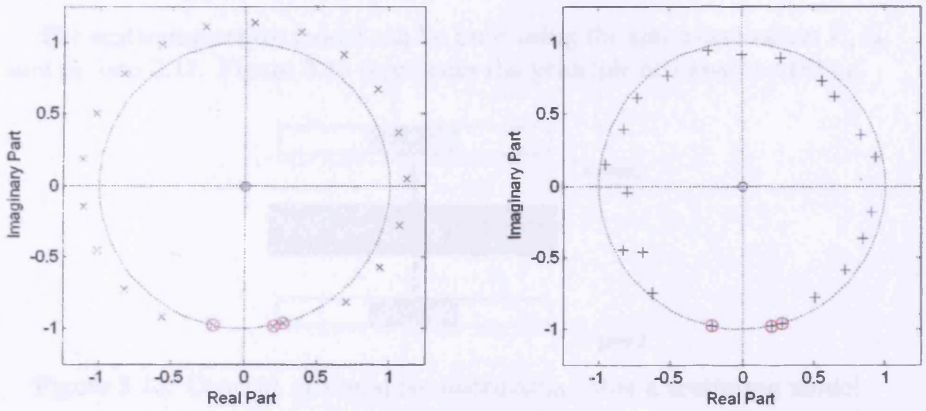

Figure 3.12: Z-plane - poles selection - root-MUSIC (left) and Matrix-pencil (right) - $N = 64$, $P = 3$, $L = 22$, $SNR = 30\ dB$

3.4.9 Amplitude-coefficient estimation

Linear least-squares fitting

Once the "true" poles are accurately determined, the coefficients can be estimated by fitting the model to the radar signal, $x(n)$. The P unknowns in the system can be calculated by a least-squares fit. This method consists of estimating the coefficients a_k that minimise the expression $\mathcal{C}$ in 3.69.

$$\mathcal{C} = \sum_{<n>} \left| x(n) - \sum_{k=0}^{P-1} a_k . p^n \right|^2 \tag{3.69}$$

The minimised cost-function is directly related to the model error in 3.14. The linear least-squares approach requires a system of P equations to determine the P coefficients. The estimates can be used to reconstruct the model, or as an initial set of values for parameter adjustment.

3.4.10 Parameter-estimate adjustment

Non-linear least-squares fitting

In our case, we make use of N samples with supposedly $N > P$. This is an overdetermined system of equations. This is why the matrix is not full rank. However, the linear model is only an approximation of the real physical system which, in practice, includes noise and non-linear effects. Both the pole estimates and the amplitude estimates can be adjuted by a non-linear least-squares fitting such as the Newton or the Levenberg-Marquardt algorithms.

3.4.11 Model reconstruction

The scattering-centre model can be built using the estimated values $\hat{P}, \hat{a}_k$ and $\hat{p}_k$ into 3.17. Figure 3.13 represents the principle of signal modelling.

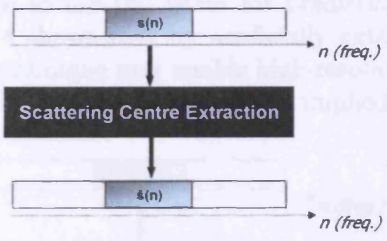

Figure 3.13: Concept of signal reconstruction using a scattering model

The model estimate, in 3.70, is determined using the modified root-MUSIC algorithm with linear least-squares fitting.

$$\begin{aligned}\hat{s}_1(n) &= (-1.0809 - 0.17994.i).(0.9993.e^{-i1.365})^n + \\ &\quad (0.1819 + 1.04.i).(0.9977.e^{-i1.29026})^n + \\ &\quad (0.96555 - 0.10906.i).(1.0003.e^{-i1.77991})^n\end{aligned} \tag{3.70}$$

A comparison with 3.28 shows that the estimation is very accurate.

3.4.12 Model accuracy

The following expressions can be used to estimate the model accuracy:

- comparison with the corrupted signal using the mean-square error :

$$\mathcal{C}_1 = \frac{1}{N} \sum_{<n>} \left| x(n) - \hat{s}(n) \right|^2 \tag{3.71}$$

  or the signal-to-residue ratio in dB

$$\mathcal{C}_2 = 10.log_{10} \frac{\sum_{<n>} |x(n)|^2}{\sum_{<n>} |x(n) - \hat{s}(n)|^2} \tag{3.72}$$

- comparison with the noise-free signal the mean-square error :

$$\mathcal{C}_3 = \frac{1}{N} \sum_{<n>} \left| s(n) - \hat{s}(n) \right|^2 \tag{3.73}$$

  or the signal-to-residue ratio in dB

$$\mathcal{C}_4 = 10.log_{10} \frac{\sum_{<n>} |s(n)|^2}{\sum_{<n>} |s(n) - \hat{s}(n)|^2} \tag{3.74}$$

The cost-functions $\mathcal{C}_3$ and $\mathcal{C}_4$ require knowledge of the uncorrupted signal $s(n)$. For this reason, they are suitable for simulation only.

3.4.13 Bandwidth prediction

Bandwidth extrapolation

Assuming the estimated model is accurate for the band of measurement, Cuomo *et al.* propose to use the latter for predicting the signal outside the band. Figure 3.14 shows that by artificially extending the frequency band, a model-based technique may enable high-resolution range-profiles to be created without effectively transmitting the implied bandwidth.

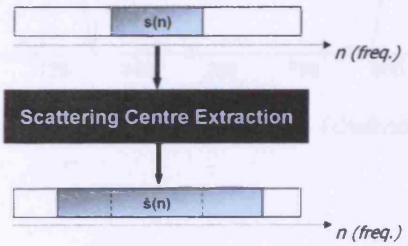

Figure 3.14: Concept of bandwidth-extrapolation using a scattering model

Figure 3.15 represents an overlay of the simulated signal, $s(n)$ (solid line), in 3.70 and the model, $\hat{s}_1$ (dashed line), obtained with linear least-squares. Built from 64 samples, the model matches the signal of the sub-band of measurement, $[11.65\ GHz - 14.85\ GHz]$. Moreover, it matches relatively well the 128 samples of the signal outside the band of measurement $[14.85\ GHz - 18\ GHz]$.

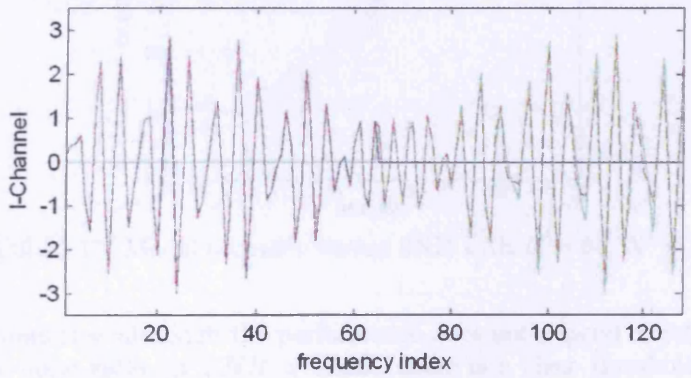

Figure 3.15: I-channel: $s(n)$ (solid line) and $\hat{s}(n)$ (dashed line) with $N = 64$, $N' = 128$, $SNR = 30\ dB$

The range-profiles of $s(n)$ and $\hat{s}_1(n)$ in figure 3.16 show that accurate model-based extrapolation can be used for enhancing the resolution.

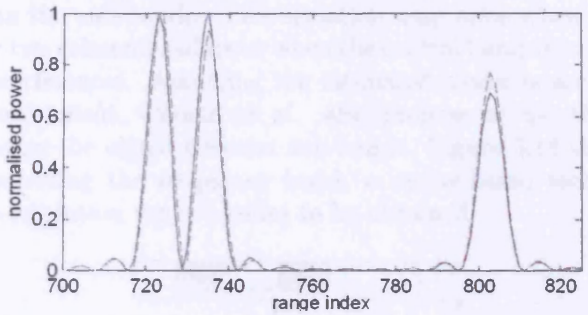

Figure 3.16: HRRP: $s(n)$ (solid line) and $\hat{s}(n)$ (dashed line) with $N = 64$, $N' = 128$

The scattering-centre extraction technique has been applied to a radar-signal backscattered from a target simulated with three point-scatterers. Figure 3.17 shows the model-accuracy (C_2) in 3.72 versus the signal-to-noise ratio. Each plot is the mean-value of fifty tests.

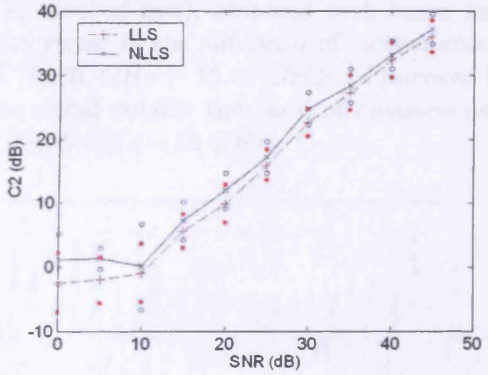

Figure 3.17: Model accuracy versus SNR with $N = 64$, $N' = 128$

It shows that although the performance does not depend closely on the signal-to-noise ratio for $SNR > 10dB$, there is a clear threshold at this value suggesting that the technique cannot accurately extract the scattering-centres below this limit. In terms of algorithm, non-linear (solid line) and linear (dashed line) least-squares generate a similar model-error.

Bandwidth interpolation

If the signal is defined across two different sub-bands, it is useful to build a model from the sub-bands. This situation may arise when the signal is measured by two coherent radars or when the central bandwidth is corrupted by strong interferences. Assuming the estimated model is accurate on the band of measurement, Cuomo *et al.* also propose to use the the latter for interpolating the signal between sub-bands. Figure 3.18 shows that by artifically extending the frequency band, a model-based technique again enables high-resolution range-profiles to be obtained.

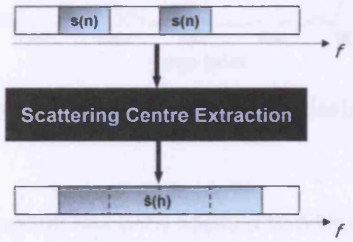

Figure 3.18: Concept of bandwidth-interpolation using a scattering model

Figure 3.19 represents an overlay of the simulated signal, $s(n)$ (solid line), and the model, $\hat{s}_1$ (dashed line), obtained with linear least-squares. The model matches the signal in the sub-band of measurement, [11.65 GHz – 13.25 GHz] and [14.85 GHz – 16.45 GHz]. Moreover it again matches relatively well the signal outside the band of measurement [13.25 GHz – 14.85 GHz] and [16.45 GHz – 18 GHz].

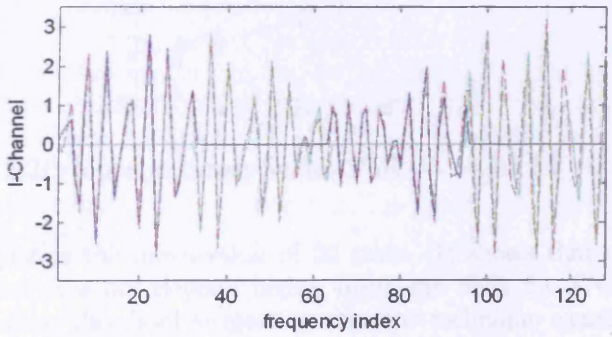

Figure 3.19: I-channel: $s(n)$ (solid line) and $\hat{s}(n)$ (dashed line) - $N = 32 \times 32$ - $N' = 128$ - $SNR = 30$ dB

The range-profiles of $s(n)$ and $\hat{s}_1(n)$ in figure 3.20 show that accurate model-based extrapolation can be used for enhancing the resolution.

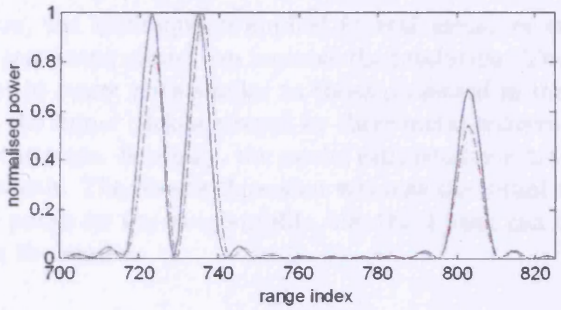

Figure 3.20: HRRP: $s(n)$ (solid line) and $\hat{s}(n)$ (dashed line) - $N = 32 \times 32$ - $N' = 128$

The modelling technique has been applied to a radar-signal backscattered from a target simulated with three point-scatterers. Figure 3.21 shows the model-accuracy (C_2) in 3.72 as a function of the signal-to-noise ratio.

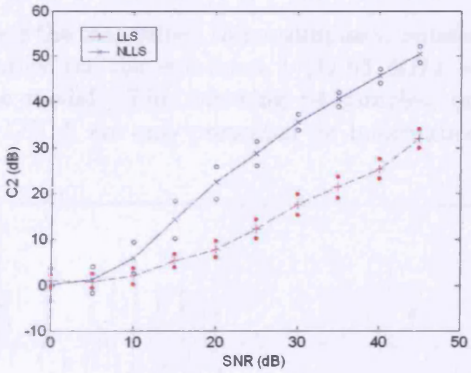

Figure 3.21: Model accuracy versus SNR - $N = [32; 32]$ – $N' = 128$

Each plot is the mean-value of 50 tests. It shows that although the performance does not depend highly upon the SNR for $SNR > 10\ dB$, there is a clear threshold suggesting that the technique cannot accurately extract the scattering-centres below this limit. NLLS (solid line) seems to perform better than LLS (dashed line). However, the fact that C_2 is greater than the noise suggests that the technique models the noise as well. Their performances converge for $SNR = 10\ dB$. Compared with the model built from 64 contiguous samples, the technique relying on NLLS performs better, whereas the technique relying on LLS performs worse.

3.5 Example

3.5.1 Principle

In this section, the technique is applied to real measurements to demonstrate that a scattering model can improve the resolution. The experimental conditions are in many ways similar to those presented in the previous section. Firstly, the signal back-scattered by three metal-spheres is modeled by three point-scatterers. Secondly, the model estimated is extrapolated across a large bandwidth. The results show that whereas the initial signal can only generate two peaks on the range-profile, the third peak can be revealed by extrapolating the model.

3.5.2 Radar signal

The radar signal is extracted from the experimental dataset obtained from ENSIETA, presented in Chapter 2 and used again in Chapter 4. It has been measured using the three spheres on a turntable at aspect-angle $\theta = 44.5°$. Due to the experimental conditions, the SNR is assumed to be relatively high. However, the following chapter provides an estimation, $SNR = 10.5\ dB$.

Figure 3.22 shows the real-valued radar samples simulated on the I-channel. The first 64 samples on the sub-band 1 [11.65 GHz – 14.85 GHz] are used to build the model. The following 64 samples, on the sub-band 2 [14.85 GHz – 18 GHz], are only presented for information.

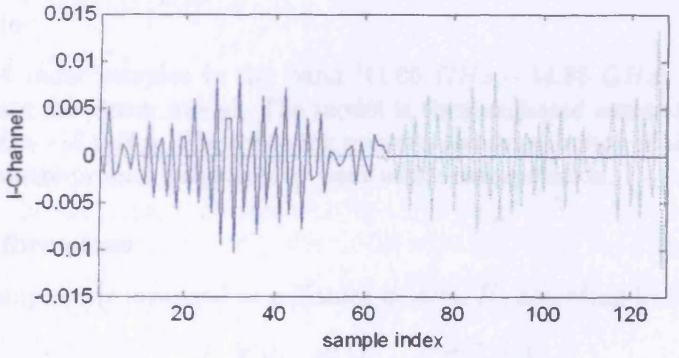

Figure 3.22: I-channel - sub-band 1 (solid-line), subband 2 (dashed-line), $SNR = 30\ dB$

Range profile

Figure 3.23 shows the range-profiles obtained by taking the IFFT of the first 64 samples (solid line) and 128 samples (dashed line). The range-profile obtained with 3.2 GHz does not enable the complete resolution of the scatterers. This is due to the fact that two of the scatterers are very closely spaced. In other words, the nominal resolution $\Delta r = 4.7\ cm$ is greater that is the distance of separation. In contrast, the range-profile obtained with the signal across the band [11.65 GHz − 18 GHz] enables resolution of the three scatterers. Here, the nominal-resolution, $\Delta r' = 2.3\ cm$, corresponding to 6.4 GHz is smaller than the distance of separation between the scatterers.

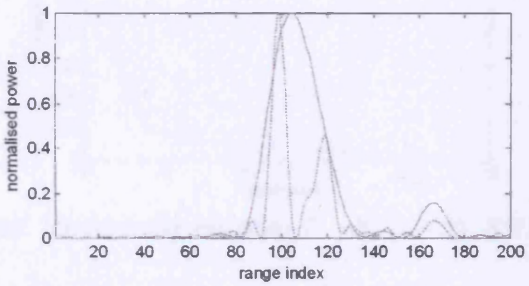

Figure 3.23: HRRP - range window $R = 58.6\ cm$, $N = 64$ (top), $N = 128$ (bottom), $SNR = 30\ dB$

3.5.3 Model estimation

Principle

The 64 radar samples in the band [11.65 GHz − 14.85 GHz] are used to estimate the Prony model. The model is then exploited across the band [11.65 GHz−18 GHz]. The following presents the construction of the model and the range-profiles enhanced by bandwidth extrapolation.

Matrix formation

The samples are arranged in a Hankel matrix, H, according to 3.75.

$$H = \begin{pmatrix} x(0) & x(1) & \dots & x(21) \\ x(1) & x(2) & & \vdots \\ \vdots & & \ddots & \\ x(42) & \dots & & x(63) \end{pmatrix} \tag{3.75}$$

where the width of the prediction-window is $L = 22$.

Model-order estimation

The model-order estimate is based on the number of strong singular values of H. Although the weakest singular values are not identical, the similarity between these singular-values, as shown in figure 3.24, suggests a correct model-order estimation: $P = 3$.

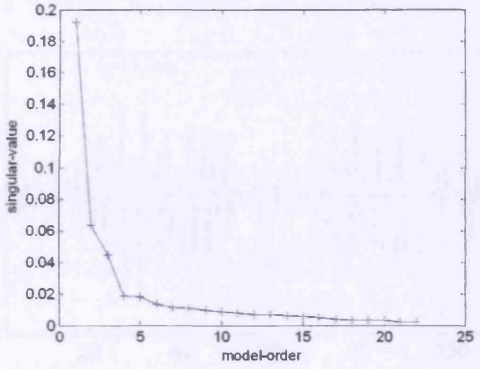

Figure 3.24: Model-order estimate $P = 3$, $L = 22$, $SNR = 30\ dB$

Model parameter determination

Figure 3.25 shows the poles obtained by root-MUSIC algorithm. Amongst them, the three poles corresponding to the three scatterers are selected because they are the closest to the unit-circle.

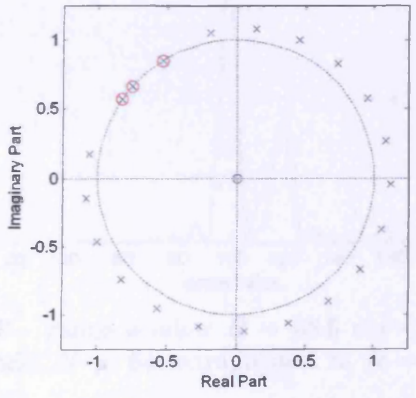

Figure 3.25: Z-plane - poles selection - real data $N = 64$, $SNR = 30\ dB$

Model extrapolation

Figure 3.26 represents an overlay of the radar signal and the model M_1 obtained with linear least-squares. The model (dashed line) generated from the first 64 samples (solid line) matches the signal in the sub-band of measurement, $[11.65\ GHz - 14.85\ GHz]$, but also in the band $[14.85\ GHz - 18\ GHz]$.

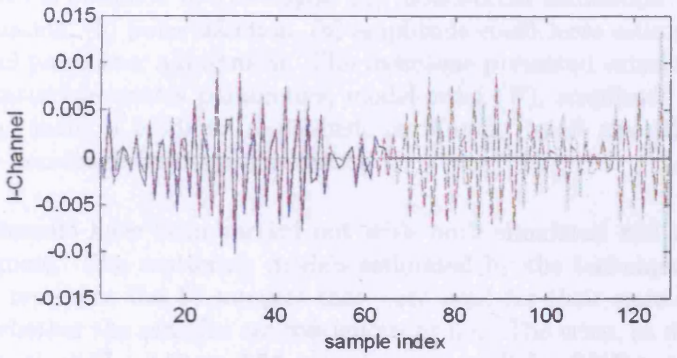

Figure 3.26: I-channel: simulated data vs. model - $N = 64$, $N' = 128$, $SNR = 30\ dB$

Figure 3.27 represents two range-profiles are obtained with the measured signal composed of 128 samples and the model computed with 64 samples and extrapolated to 128 samples.

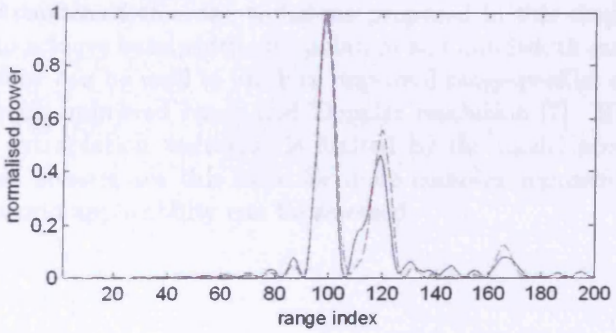

Figure 3.27: HRRP - range window $R = 58.6\ cm$ - real data $N = 128$ (solid line) vs. model $N = 64$ extrapolated to $N = 128$ (dashed line), $SNR = 30\ dB$

On both range-profiles, the three peaks corresponding to the three scatterers are present. Comparison with the true measured data reveals that their positions are very accurate. In this case, the technique allows the res-

olution of the three scatterers with only 3.2 GHz bandwidth, that is half of the bandwidth needed to produce the range-profile using traditional method.

3.5.4 Conclusion

In this section, we introduced a model-based technique for reconstructing, interpolating and extrapolating the complex-valued radar spectrum. The model is obtained in five stages: (1) model-order estimation, (2) poles determination, (3) poles selection, (4) amplitude coefficients estimation and (5) model parameter adjustment. The technique presented extracts the so-called scattering-centres parameters, model-order (P), amplitude (a_k) and poles (z_k) using a modified root-Music or Matrix Pencil algorithms, and linear or non-linear least-squares fitting.

Experiments have been carried out with both simulated and measured radar-signals. The scattering models estimated by the technique can accurately represent the 64 samples that were used for their estimation, no matter whether the samples are contiguous or not. The error, as defined by the expressions C_i - 3.71 to 3.74 - is relatively small for $SNR > 10\ dB$. In this region, the models are also able to predict the radar samples outside the band of measurements. This can be used for bandwidth interpolation or extrapolation.

Interpolation and extrapolation require prediction of the radar signal outside the band of measurements. By first computing a model, the technique enables a signal to be synthesized across a single wide bandwidth. This section has confirmed that the technique proposed in this chapter has the capability to achieve bandwidth interpolation and bandwidth extrapolation. Such technique can be used to produce improved range-profiles or ISAR images with both improved range and Doppler resolution [7]. However, the bandwidth extraplation technique is limited by the model accuracy. The next chapter investigates this issue for more complex representation from which real-world applicability can be assessed.

Chapter 4

MODELLING MAN-MADE TARGETS FOR BAND-EXTRAPOLATION TECHNIQUES

4.1 Introduction

4.1.1 Foreword

In the previous chapter a technique was introduced for estimating the ultra-wideband radar signature of a target without transmitting the total bandwidth required. The technique consists of fitting an all-pole model to a set of radar measurements from the in-phase (I) and quadrature (Q) channels. Once the expression is determined by combined use of super-resolution and least-squares fitting algorithms, a new dataset of samples is calculated for the same frequencies. The model accuracy is then estimated by computing the quadratic error or alternatively the signal-to-residue ratio. For small errors, it is proposed that the model also be used to predict the samples outside the band of measurement. This extrapolation of the bandwidth enables conventional imaging-techniques such as those based on the Discrete Fourier Transform to draw range-profiles with enhanced resolution.

There exists a large body of literature on super-resolution algorithms. In general this is treated as a problem of harmonic retrieval from time-series whose temporal extent does not enable close frequencies to be resolved by application of the Discrete Fourier Transform. Some very encouraging results have been shown by introducing super-resolution algorithms to solve practical problems encountered in radar imaging and detection. Typically, ideal point-scatterers that are located within the same Fourier range-bin

are resolved using super-resolution algorithms such as Matrix Pencil, MUSIC, root-MUSIC, or ESPRIT. However, transposing these techniques to real-world applications poses an important set of questions regarding the method's capability, many of which are addressed in this chapter.

4.1.2 Limits of the modelling technique

Introduction

The modelling technique introduced earlier has limits which are highlighted in this section. As an example, it is applied here to a radar signal backscattered by a real flying Boeing-727 aircraft. First, the estimated model is compared with the signal across the measurement-band. It is then extrapolated and compared with the signal across a larger band. By employing a complex and extended target such as a Boeing 727, the experiment unveils some aspects of the modelling process which do not necessarily appear when applied to simple targets. In particular, it challenges the relation between the mathematical accuracy as defined by distance between the signal and the model, and the physical accuracy which refers to capability to characterise the scattering properties of the target. This is not a trivial question as scattering processes such as creeping waves, edge diffraction and possibly non-linear behaviours are not necessarily captured in our mathematical model.

Figure 4.1: Boeing B-727

Radar signal

The dataset used has been provided by Dr Victor Chen from the US Naval Research Laboratory. "The Stepped Frequency Radar operates at 9 GHz and has a bandwidth of 150 MHz. For each pulse, 128 complex-valued range-samples were saved. The file contains 128 successive pulses. Motion compensation and range processing have been applied to the data. A radar image can be reconstructed by taking 1-D FFT of 128 pulses for each range sample." [11]

Figure 4.2 shows the ISAR image obtained by taking the FFT of a 128×128 complex-valued matrix with zero-padding with 2^{10} indices.

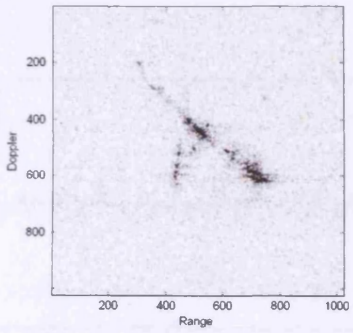

Figure 4.2: B-727: ISAR image

Model estimation

The 128 complex-valued samples forming the 49^{th} pulse are extracted from the data and used as a test-signal. The in-phase values are represented in blue in figure 4.3. The modelling technique is directly applied to the test-signal. The matrix width, L, is set $L = 43$ which follows the recommendation in 3.66. As the various techniques presented did not agree on the model-order estimate, an arbitrary value has been chosen: $M = 16$. The range-profiles obtained by direct reconstruction of the model generated from 128 samples and without parameter adjustment are represented in figure 4.3. The signal-to-residue ratio across the 128 samples is $SRR = 2.55\ dB$.

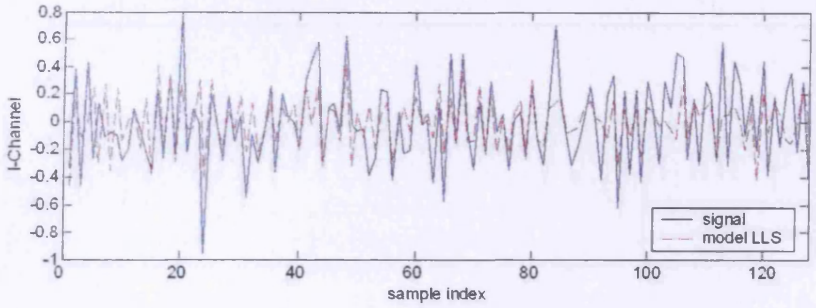

Figure 4.3: I-channel: measured data vs. model - $N = 128$

A new model is then determined from 75% of the signal only. The model-order and the ratio L/N are conserved so that $M = 16$ and $L = 32$ in this case. This 96 sample-model is then used to form a total band of 128 samples. Figure 4.4 represents the 96-sample signal provided (blue), the 32-sample missing signal (green) and the model (red). The signal-to-residue ratio is now $SRR = 1.95\ dB$ across the first 96 samples and $SRR = -4.15\ dB$ across the whole band, that is about 6.6 dB lower than the model obtained

using the whole band.

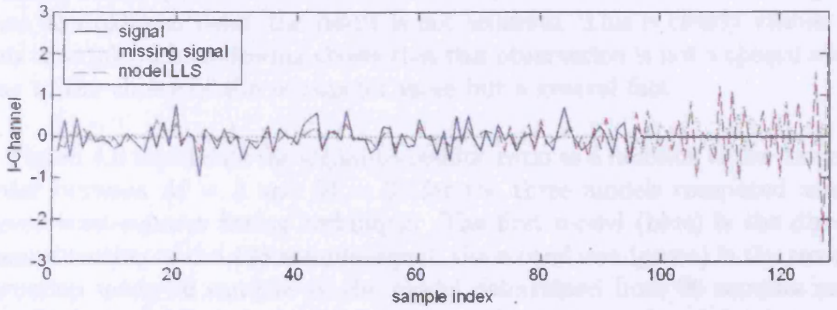

Figure 4.4: I-channel: measured data vs. model - $N = 96$

The same operation is then carried out on 75% of the signal but the 96 samples are distributed across two bands of 48 samples this time. The indices of the bands are $n_1 = [0 \dots 47]$ and $n_2 = [80 \dots 127]$. The indices of the missing band are $[48 \dots 79]$. The parameters are set to $M = 16$ and $L = 17$ to take into account the size of the sub-bands. The estimated model is then used to form a total band of 128 samples. Figure 4.5 represents the initial signal distributed over two 48-sample band (blue), the 32-sample missing signal (green) and the model (red). The signal-to-residue ratio is $SRR = 1.08\ dB$ only across the modelling band and $SRR = 0.62\ dB$ across the total band. The three results are discussed in the following section.

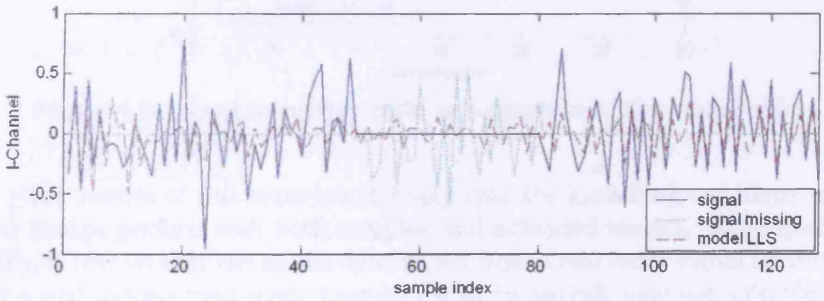

Figure 4.5: I-channel: measured data vs. model - $N = 2 \times 48$

Discussion

These experiments show that using the same model-order, $M = 16$, the model estimate seems to vary with of the number of samples of the signal but also with their distribution. Here the model determined enables reconstruction of the signal over the modelling band with a relatively good

accuracy, especially when the signal is defined over a single band. However, the above example shows that when this model is used to estimate the signal over an unknown band, the result is not accurate. This is clearly visible in this example. The following shows that this observation is not a special case due to the choice of the parameter value but a general fact.

Figure 4.6 represents the signal-to-residue ratio as a function of the model-order between $M = 3$ and $M = 30$ for the three models computed using linear least-squares fitting technique. The first model (blue) is the direct reconstruction of the 128 sample-signal, the second one (green) is the reconstruction using 96 samples of the model determined from 96 samples and the third one (red) is the model determined from 96 samples of the data and extrapolated to 128 samples. The figure shows that when the models are used to predict the data across the missing band, the accuracy strongly decreases. This experiment also suggests that the larger the model-order, the more accurate the reconstructed model and paradoxically the less accurate the extrapolated n

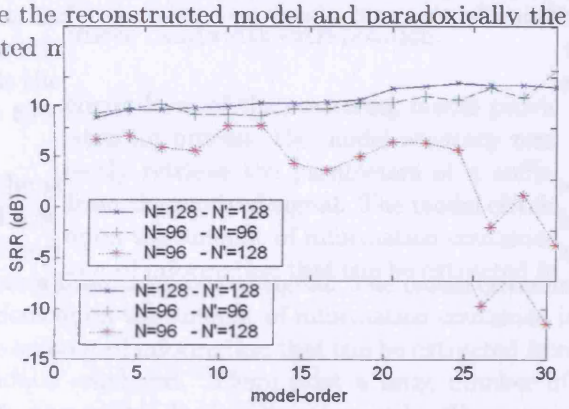

Figure 4.6: signal-to-residue ratio as a function of the model-order

The results of this experiment imply that the modelling technique may not always perform well with complex and extended targets. More specifically, it reveals that the model determined from a real radar-signal scattered by a real moving man-made target such as an aircraft may not suitable for extrapolation and should thus not be considered as accurate in the physical sense.

4.1.3 Problem statement

Both the use of a model to reproduce the radar data and the determination of the model parameters are subject to a rather strict theoretical framework. The model is justified by the fact that it can approximate the scattering mechanisms that are dominant for conditions that are supposedly the experimental ones. In order to rely on the estimated model, it is

essential that the validity of these assumptions be demonstrated and that the error arising from various approximations be bounded. These precautions can be neglected when experiments are carried out in the very ideal conditions which serve to mathematically approximate the radar problem. Nevertheless, this should not be the case when the experiments involve real radar signals or more specifically targets that cannot be described by a set of theoretical point-scatterers.

For most applications, the validity of the physical assumptions that are used to justify the chosen model is still to be demonstrated. The first one is the approximation of a signal as a sum of complex exponentials where each cisoid corresponds to the contribution of an independent and strongly reflecting point-scatterer. Another assumption concerns the description of the scattering model by linear regression. Considering that multi-bounce and surface-waves are not expressed by the model, it appears that along with modelling real radar-signals comes a large set of questions regarding both the accuracy and the physical meaning of the scattering model and on which depends the prediction of samples and subsequently the capability of the technique to achieve bandwidth extrapolation.

Assuming the generic form of the scattering model provides an accurate description of a scattering process, the model accuracy remains limited by the ability to correctly retrieve the parameters of a sufficient number of scattering-centres from the received signal. The model obtained is obviously highly dependent upon the amount of information contained in the dataset processed, the amount of information that can be extracted from this dataset and the technique employed. There exist a large number of factors that can be directly responsible for inaccurate models. They are related to the continuity of the band, the number of samples, the model-order, the number of strong scatterers, the conformity of the scattering-centres to the point-scatterer model, the method-parameters and the extrapolation-ratio. In addition, the corruption of the signal by sources other than the target can also affect the accuracy of the model and hence also makes the modelling process less robust.

4.1.4 Outline

Based upon this example, the rest of this chapter attempts to provide a stronger foundation for challenging the accuracy of the modelling technique, the accuracy of the model itself and the legitimacy of the model residual error to be used as an indicator of the model capability to achieve bandwidth extrapolation. The relatively broad analysis of the modelling method could be used as a guideline for setting-up the system parameters and interpreting the results.

This chapter starts with an introductory example that has, for the first time, highlighted some of the issues associated with the scattering-centre model. In the second section, the model is studied individually. The sensitivity of the model to its parameters is investigated and the greatest source of error is unveiled. This source appears to be the over-estimation of the pole-magnitude. The third section concentrates on the modelling technique and shows that over-estimation of the pole-magnitude occurs under certain conditions. It also shows that amongst all the possible causes of limitation, the factors which lead to the creation of a deficient model would increase the probability of seeing an over-estimation of the pole-magnitude.

4.2 Model

4.2.1 Introduction

The accuracy of the modelling stage naturally has some limits for which causes and consequences need to be clearly identified. The analysis of the model is performed in three steps. First, the next section reviews the relations between the model-parameters and the physical properties of the scattering mechanisms. It contains a qualitative analysis of the contribution of each parameter to the model followed by a sensitivity analysis. Based on simple examples, the second section uses the quadratic-error to provide a quantitative study of the model sensitivity. Finally, the limits of the latter expression as a measure of model-accuracy and its implication for bandwidth-extrapolation are discussed.

4.2.2 Model-parameters

The so-called scattering-centre model used to reconstruct the radar signal can be described as a weighted sum of M complex exponentials known as cisoids. For each elementary signal, the modelling technique determines three parameters: pole-magnitude (ρ), pole-angle (ϕ), and amplitude (a).

- the model-order, M, determines the number of components in the signal. It is loosely related to the number of scattering-centres needed to describe the target. Although it may be possible to associate scattering-centres with individual scattering elements, linking the mathematical expression to the physical interpretation is not straightforward. For example, multipath and surface waves are often responsible for scattering that are not taken into account by the model employed.

- the amplitude-coefficient, a_k, contributes to the relative power and relative signal-to-noise ratio associated with a given scattering-centre. Physically, this parameter is related to the scatterers' RCS. Exponentials weighted by large amplitude coefficients are responsible for strong singular-values in the SVD decomposition of the observation matrix and for high peaks in the range-profile. This phenomenon is exploited for estimating the model-order.

- the pole-magnitude, ρ_k, is the parameter used to take into account the frequency dependence of the RCS. Physically, this parameter is related to the geometry of the scatterer as indicated in table 1. For pole-magnitudes greater than one, the relative power increases with the frequency whereas this is the opposite for values smaller than one. On the range-profile, the peak-amplitude increases rapidly with the pole-magnitude. Finally, the pole-magnitude has a unique effect on the peak-width in such a way that values other than one introduce a

spread of the energy in range, the minimum peak width being obtained for $\rho_k = 1$.

- the pole-angle, ϕ_k, determines the frequency of the signal. Models composed of ideal point-scatterers are periodic by definition. Those composed of a limited number are characterised by a short period, which can be observed if the bandwidth is large enough. Physically, this parameter is related to the time-delay induced by the distance from radar to scatterer. For this reason, the determination of a scatterers' location is either treated by spectral analysis or, in the case of point-scatterers, as the problem of harmonic retrieval. The complete angular-domain $[0 - 2\pi]$ is defined by the unambiguous range window $R_u = c/(2\Delta f)$. For extended targets, a phenomenon of aliasing can be observed if the absolute pole-angle is greater than 2π.

4.2.3 Model susceptibility

Introduction

For convenience the assumption is often made that man-made targets are typically characterised by a limited number of strong scatterers that are responsible for most of the returned signal. Accurate modelling of their individual contributions could in some cases enable the reconstruction and prediction of the signal across a large bandwidth. However, the accuracy of the results depends upon the sensitivity of the model and upon the accuracy of the modelling technique employed.

In this example, equation 4.1 is used to generate the reference signal, $s(n)$. Perturbations which, in practice, represent the error of estimation are then individually applied to each parameter. Both the reference-signal and the corrupted signal which is referred to as the model are plotted on the same graph.

$$s(n) = e^{i\frac{2\pi 10.5\Delta r}{R}n} + e^{i\frac{2\pi 15.5\Delta r}{R}n} \tag{4.1}$$

where $\frac{\Delta r}{R} = \frac{1}{N}$ and the total number of samples $N = 128$.

Equation 4.1 predicts the return from two ideal scatterers such as points. This can be inferred from the magnitude of the poles, $\rho_k = 1$. The range of the scatterers can be obtained from the pole-angles and for a 128 sample signal the difference $\Delta\phi_k = (2\pi(.(5\Delta r)/R$ implies that the scatterers are separated by exactly five resolution-cells in range. Finally, the amplitude coefficients $a_k = 1$ express the fact that the receiver sees the same amount of energy from each scatterer.

Amplitude

Figure 4.7 represents the initial signal (solid line) and the model (dashed line) obtained for the estimated values $\hat{a}_2 = 1$ and either $\hat{a}_1 = 0.8$ (top) or $\hat{a}_1 = 1.2$ (bottom). This corresponds to variations of the amplitude-coefficient, $\hat{a}_1$, by -20% and $+20\%$, respectively. The variation of the amplitude coefficient seems to have limited effect on the signal as its general form is maintained. Nonetheless, large positive perturbations introduce greater sidelobes in the range-profile which may make the detection of weak scatterers difficult.

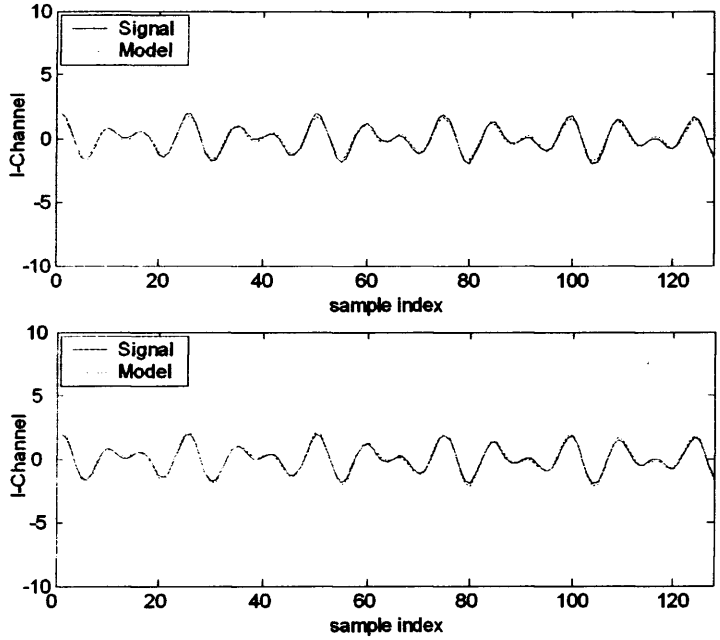

Figure 4.7: I-channel: variation of amplitude coefficient by -20% (top) and $+0.20\%$ (bottom)

Pole angle

Next we consider sensitivity to changes in the pole angles. Figure 4.8 represents the initial signal (solid line) and the model (dashed line) obtained for the estimated values $\hat{\phi}_2 = 0.5\ rad$ and either $\hat{\phi}_1 = 0.5031\ rad$ (top) or $\hat{\phi}_1 = 0.5277\ rad$ (bottom), which corresponds to variations of the pole-angle, $\hat{\phi}_2$, by -25% and $+25\%$ of the nominal-angular resolution, respectively.

The variation of the phase-angle modifies the pattern of constructive and destructive interferences. On the figure, the difference between the signal

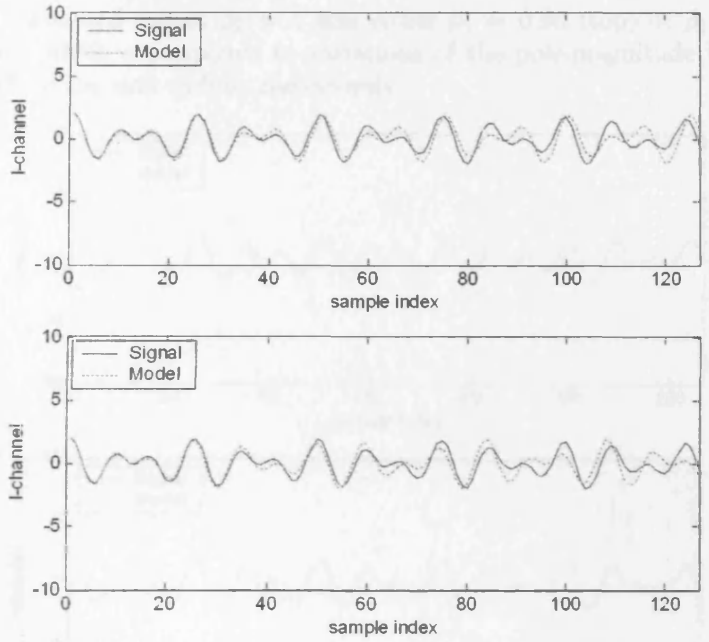

Figure 4.8: I-channel: variation of pole angle by $-0.25\Delta\phi$ (top) and $+0.25\Delta\phi$ (bottom)

and the model is more obvious at high frequency. This is due to the difference of periodicity between the two patterns. This can explain the decreasing performance of a model when it is used for extrapolating over a large bandwidth. Similarly, perturbing the pole-angle of a large number of scatterers causes variations which may be significant, even at low frequency.

Thus it is seen that the perturbation of a pole-angle has obvious effects that can be observed in the time-domain. In a one-dimensional range-profile, the range of the peak corresponding to the perturbed pole would be shifted in range, proportional to the angular variation. Therefore a variation common to all pole-angles would introduce a range offset whereas individual variations would cause different shifts of the peaks in range. The second type of perturbation would cause greater errors to most classification techniques. In this way, the limitations of the modelling approach are becoming apparent.

Pole magnitude

Finally we examine effects of changes in the pole magnitudes. Figure 4.9 represents the initial signal (solid line) and the model (dashed line) obtained

for the estimated values $\hat{\rho}_2 = 1$ and either $\hat{\rho}_1 = 0.95$ (top) or $\hat{\rho}_1 = 1.05$ (bottom), which corresponds to variations of the pole-magnitude by -5% and $+5\%$ of the unit radius, respectively.

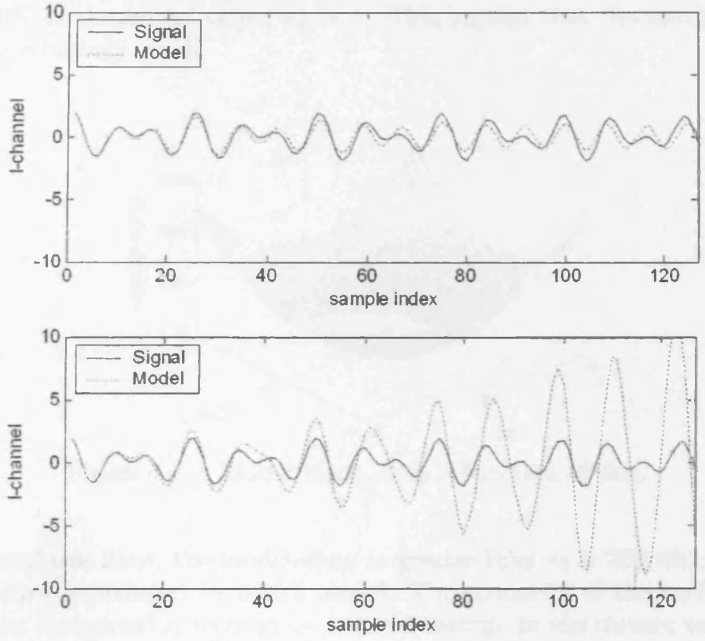

Figure 4.9: I-channel: variation of pole magnitude by -0.05 (top) and $+0.05$ (bottom)

The model is clearly more sensitive to positive variations of the pole-magnitude than to negative ones. Considering that the signal results from an autoregressive process, this result is predicted by the linear theory which requires as a condition of stability that no pole of the transfer function be located outside the unit-circle. In both cases, the variation is greater at high frequency due to the fact that the contribution of the pole-magnitude to the model is in the form ρ^n, where n is the frequency index.

4.2.4 Model Accuracy

This section presents the variation of the signal in 4.1 as a function of the perturbations of the model-parameters. It is quantified by means of the model quadratic-error in 4.2 where M_n and s_n corresponds to the estimated model and the signal in 4.1, respectively.

$$e = \sum_{n=0}^{N-1} |M_n - s_n|^2 \tag{4.2}$$

Amplitude

Figure 4.10 represents the model-error as a function of the variation of the amplitude coefficient, $\Delta a_k = \hat{a}_k - a_k$. The extent of the variation corresponds to $\pm 100\%$ of the initial value, $a_k = 1$. This implies that the sensitivity to errors is relatively small.

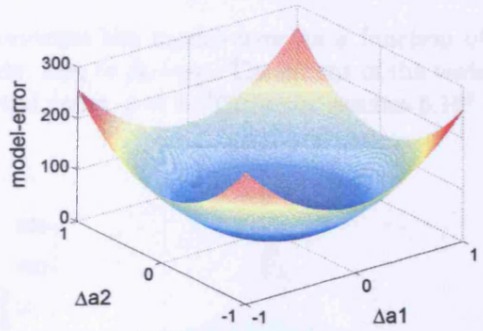

Figure 4.10: Model-error, e, as a function of Δa_k

Beyond this limit, the model-error is greater than $e_0 = 256$ which would be the error introduced by a null model. The concavity of the surface suggests that optimisation techniques would converge to the correct values.

Pole angle

Figure 4.11 represents the model-error, e, as a function of the variation of pole-angle, $\Delta\phi_k = \hat{\phi}_k - \phi_k$.

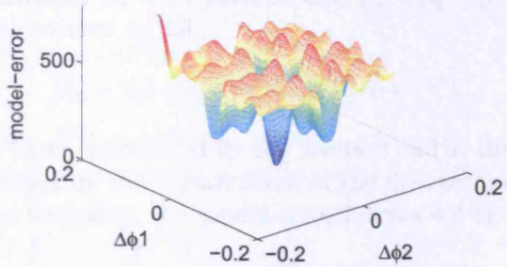

Figure 4.11: Model-error, e, as a function of $\Delta\phi_k$

The extent of the variation corresponds to four times the nominal resolution that is ±3% of the unambiguous extent. The shape of the function suggests that optimisation techniques may not converge to the expected value but to a local minimum instead. This highlights the importance of the accuracy of the estimator and requires careful implementation.

Pole magnitude

Figure 4.12 represents the model-error as a function of the variation of the pole-magnitude, $\Delta\rho_k = \hat{\rho}_k - \rho_k$. The extent of the variation corresponds to ±1% of the initial value, $\rho = 1$. The error reaches 6.10^6 for $\frac{\Delta\rho_k}{\rho} = +5\%$.

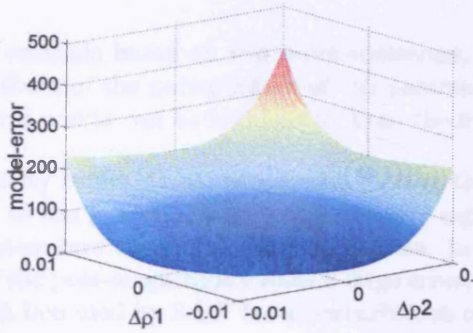

Figure 4.12: Model-error, e, as a function of $\Delta\rho_k$

The graph confirms that positive variations of the pole-angle have greater effects on the model error than negative ones. In order to quantify this behaviour, one can derive the expression of the difference between a signal and a model at frequency index n. For this, let us consider that the pole-magnitude is the only modified parameter, and that the variations of magnitude are identical for both poles so that $\hat{\rho}_1 = \hat{\rho}_2 = \hat{\rho}$. In this case, the expression can be written as 4.3.

$$|\hat{s}_n - s_n| = |\hat{\rho}^n - 1|.|e^{i.\phi_1 n} + e^{i.\phi_2 n}| \tag{4.3}$$

Since the second term is bounded by the values 0 and 2, the quadratic error can be approximated by the contribution of the first term only. Depending on the sign of the variation, the model-error follows 4.4 or 4.5.

$$|\hat{s}_n - s_n|^2 \approx \gamma_{1,n}.\hat{\rho}^{2n} \quad ,|\rho| > 1 \tag{4.4}$$

$$\approx \gamma_{2,n}.(1 - 2\hat{\rho}^n) \quad ,|\rho| < 1 \tag{4.5}$$

where $\gamma_{1,n}$ and $\gamma_{2,n}$ are independent of ρ_k.

This expression confirms that the error increases with both the number of samples and the distance of the pole to the unit-circle. Moreover, it confirms the model instability caused by poles located outside the unit-circle. For model-estimation, this implies that the model is especially sensitive to positive variation and that errors would be emphasized by bandwidth extrapolation.

4.2.5 Key points

The scattering-centre model used to reproduce the radar signal can be described by M sets of three parameters α_k, ϕ_k, and ρ_k, where M is the model-order and the elements of each set are the amplitude-coefficient, the pole-angle and the pole-magnitude, respectively.

In the simple example based on two point-scatterers, the above analysis has shown the effects of the perturbation of the parameters on the form of the model. Several points can be highlighted from the above analysis.

1. The sensitivity of the model varies with each of the parameters. The sensitivity to the pole-magnitude may be very significant as this parameter determines the stability of the process. In the example, a 5% increase of the pole-magnitude causes a large error, $e = 6.10^6$, whereas the latter is bounded by 2.10^3 for a perturbation of the pole-angle.

2. The fact that the contribution of the pole-parameter to the signal is frequency-dependent makes its sensitivity a serious issue for bandwidth extrapolation techniques. In practice, errors due to the pole-magnitude increase with the extrapolated bandwidth in a power-of-n relation, where n is the frequency index.

3. The shape of the model-error for a variation of the pole-angle suggests that optimisation techniques may not converge to the desired value due to the presence of several local minima. This highlights the importance of the initial pole-angle estimate.

4. The level of sensitivity of the model suggests that model-based classification will be similarly sensitive to each parameter. Considering the sensitivity to the pole-magnitude and the amount of information contained in this parameter with respect to those contained in the signature, it seems preferable to employ a technique less sensitive to this parameter.

4.3 Modelling technique

4.3.1 Introduction

The previous section shows that the accuracy of the model depends upon the modelling technique as the model-error varies with the error on each of the parameter estimates. In the technique proposed, five consecutive stages are used to estimate these parameters. They include model-order estimation, pole-estimation, pole-selection, amplitude-coefficient estimation and parameter adjustment. Because of the sequential form of the process, each stage has reliance upon the previous so that the final accuracy of the model has reliance on the accuracy of each stage.

The accuracy of each stage varies with the target, the transmitted signal, the statistical properties of the noise, and with elements not included in the model that may contribute to the dataset such as other scattering phenomenon, clutter, interference and multipath. Ideal conditions are expected to be met when the signal is produced by a few point-like scatterers with high signal-to-noise ratio and no other contributions. Away from these conditions, the accuracy of the model is expected to decrease but little information is known about that.

Depending on the experimental conditions, various perturbations may affect the input dataset, which subsequently could lead to errors in the parameter-estimates. Considering the sensitivity of the scattering-centre model highlighted in the previous section, even small errors may be sufficient to alter significantly the representation of the model. This problem which would be emphasized by bandwidth extrapolation may then have negative impacts on model-based techniques used for applications including imaging, classification and recognition.

This section studies the modelling process with the aim of identifying the mechanisms that are responsible for large errors. It relies on the expression of the model accuracy given by the signal-to-residue ratio. A sensitivity analysis is carried out with respect to the signal-to-noise ratio, the model-order, the matrix dimension, the number of samples and the signal bandwidth. Both the simulated and measured signals are used for this study.

The parameters are set as follow: model-order, $M = 3$, and observation-matrix width, $L = N/3$. The pole-estimation is carried out using the modified version of the root-MUSIC algorithm presented in Chapter 3. The poles selected are the M poles that are those closest to the unit-circle. The amplitude coefficients are estimated by solving a linear least-squares equation. Finally, the parameters may be adjusted by non-linear least-squares fitting.

4.3.2 Signal-to-noise ratio

Introduction

This section investigates the effects of the noise on the model. The metric used is the signal-to-residue ratio and the analysis contains a detailed assessment of the expression used as an indicator of the model accuracy. The conclusions serve as a basis for interpretation of the results obtained with the modelling technique. By comparing the results from simulated and measured signals, the experiment supports the principle of the technique reviewed but with limited extent. It also challenges the legitimacy of the signal-to-residue ratio. In addition, a simple technique for estimating the signal-to-noise ratio of a measured radar signal is proposed in this section.

The signal-to-residue ratio can be written as the ratio of the power of the reference-signal to the power of the residue as in 4.6.

$$SRR = \frac{\sum_{n=0}^{N-1} |\tilde{y}_n|^2}{\sum_{n=0}^{N-1} |M_n - \tilde{y}_n|^2} \tag{4.6}$$

where $\tilde{y}$ is the reference version of the signal, preferably the closest form to the deterministic component in the least-squares sense, M is the model, and $\bullet_n$ indicates the sample index.

Simulated signal

When the received signal, y_n, is simulated, the noise-free version of the signal, s, can be employed as a reference. In this case, 4.6 can be written as 4.7

$$SRR = \frac{\sum_{n=0}^{N-1} |s_n|^2}{\sum_{n=0}^{N-1} |\hat{s}_n + \hat{e}_n - s_n|^2} \tag{4.7}$$

where the residue is defined by $\hat{e}_n = M_n - \hat{s}_n$ with $\hat{s}$ the model component associated with the deterministic part of the signal.

Assuming the deterministic part of the signal is accurately modelled, that is $\hat{s}_n = s_n$ over $n = [0, 1, \ldots, N-1]$, 4.7 can be simplified to 4.8

$$SRR = \frac{\sum_{n=0}^{N-1} |s_n|^2}{\sum_{n=0}^{N-1} |\hat{e}_n|^2} \tag{4.8}$$

Since the residue, $\hat{e}$, is expected to decrease when the SNR increases, the SRR is expected to increase with the SNR in this equation. In order to characterise this variation, the model-error is computed for the simulated signal in 3.22 for various levels of noise, u. This signal simulates the return from three point-scatterers such as the measured signal used in the following section.

Figure 4.13 represents the SRR as defined in 4.7 for various SNR values between -20 dB and 40 dB. Each marker represents the mean-value of the SRR computed for 25 tests. The dots represent the maximum and minimum SRR values obtained.

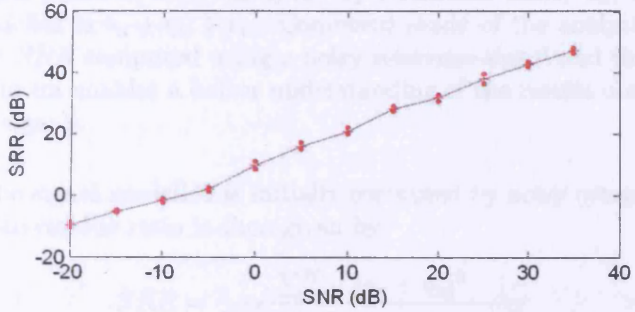

Figure 4.13: Variation of the signal-to-residue ratio as a function of the signal-to-noise ratio

Figure 4.13 confirms that the SRR increases with the SNR. The small difference between the mean and the extreme values of SRR on figure 4.13 suggests that the variance is relatively small. It can be inferred from the same figure that the power of the residue is 10 dB greater than the power of the noise added, that is $SRR \approx SNR + 10$ dB. It may thus be possible to approximate the residue as a fraction of the noise, u. This is formalised in 4.9.

$$< |e_n|^2 > \approx K. < |u_n|^2 > \tag{4.9}$$

By substituting 4.9 into 4.8

$$SRR \approx \frac{\sum_{n=0}^{N-1} |s_n|^2}{K \sum_{n=0}^{N-1} |u_n|^2} = \frac{SNR}{K} \tag{4.10}$$

where $K \approx 0.1$ based in figure 4.13. This expression estimated from experimental conditions is adapted in the following section to the more realistic case where measured signals are chosen as reference-signals.

Measured signal

When the dataset modelled is a measured signal, the deterministic component, s_n, is generally unknown. The latter cannot be used as a reference-signal, $\tilde{y}_n$, for computing the SRR in 4.6. For this reason, a sensitivity analysis is carried out with a signal initially corrupted with noise. The SNR value that is reported on the following figures only refers to the noise added during the study and not to the noise initially present. This is essential for

understanding what is actually determined when the SRR is computed with a measured signal.

In the following, a noisy measured signal, $s_n + \eta_n$, is used as a reference-signal. This signal is then corrupted by additional noise, u_n, so that the signal modelled is $s_n + \eta_n + u_n$. Combined study of the analytical expression of the SRR computed using a noisy reference-signal and the results of this experiment enables a better understanding of the results obtained with measured signals.

When the signal modelled is initially corrupted by noisy components, η_n, the signal-to-residue ratio is then given by

$$SRR = \frac{\sum_{n=0}^{N-1} |s_n + \eta_n|^2}{\sum_{n=0}^{N-1} |\hat{s}_n + \hat{e}_n - s_n - \eta_n|^2} \tag{4.11}$$

The signal-to-noise ratio of the reference signal, SNR_0, is given for $u_n = 0$ by

$$SNR_0 = \frac{\sum_{n=0}^{N-1} |s_n|^2}{\sum_{n=0}^{N-1} |\eta_n|^2} \tag{4.12}$$

Assuming the deterministic part of the signal is accurately modelled, that is $\hat{s}_n = s_n$, 4.11 can be simplified as 4.13

$$SRR = \frac{\sum_{n=0}^{N-1} |s_n + \eta_n|^2}{\sum_{n=0}^{N-1} |\hat{e}_n - \eta_n|^2} \tag{4.13}$$

Based on 4.9, it can be assumed that the residual varies in proportion with the total noise. In this case, the denominator can be approximated by a simpler expression. Depending on the power of the added noise relative to the power of the initial noise, the asymptotic form of the SRR can be approximated by 4.14 and 4.15.

$$SRR = \frac{\sum_{n=0}^{N-1} |s_n + \eta_n|^2}{\sum_{n=0}^{N-1} |\eta_n|^2} \approx SNR_0 \quad , SNR \gg SNR_0, \tag{4.14}$$

$$= \frac{\sum_{n=0}^{N-1} |s_n + \eta_n|^2}{\sum_{n=0}^{N-1} |\hat{e}_n|^2} \approx SNR/K \quad , SNR \ll SNR_0, \tag{4.15}$$

where the value of $K \approx 0.1$ has been estimated in the previous example.

The sensitivity analysis is now carried out on a measured signal corrupted by an initial noise, η. The signal employed is extracted from the dataset used to create figure 2.10. Figure 4.14 represents the SRR as defined in 4.6 for $\tilde{y}_n = y_n$. The blue lines refer to the measured signal. The SNR refers to the noise, u_n, that is added afterwards and does not include the unknown

initial noise, η_n. This is meant to match to the experimental conditions. The figure confirms the presence of the two behaviours described in 4.14 and 4.15 .

In order to simulate the measured signal, the simulated clean signal in 3.22 has been corrupted by an additive white Gaussian noise, $\hat{\eta}$. The power of the noise present in the measured signal being unknown, it has been estimated in the following way. First it is assumed from 4.14 that when modelling a noisy series of complex exponentials, the signal-to-residue ratio of the model is equal to the signal-to-noise ratio, that is $SRR = SNR_0$. Based on this and the figure 4.14, the initial SNR is estimated to be $SNR_0 \approx SRR \approx 10.5\ dB$.

Once the simulated noisy signal is created with $SNR_0 = 10.5\ dB$, a sensitivity analysis is carried out on the noisy simulated signal by adding more noise u_n and computing the models. The models of the simulated signals are then estimated and SRR computed for 24 values of u_n such that the SNR defined in 4.12 is between $-20\ dB$ and $40\ dB$. The results are represented by the red line on the same figure, 4.14. Each marker represents the mean-value of 25 tests.

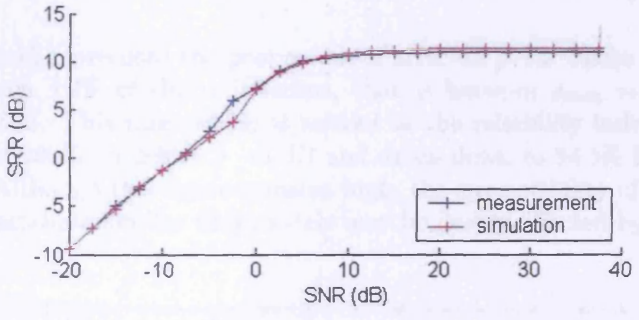

Figure 4.14: Variation of the signal-to-residue ratio as a function of the signal-to-noise ratio for both measured signal and simulated signal where $SNR_0 = 10.5\ dB$

Figure 4.14 confirms the form the SRR as predicted by the analysis. Although the value of K is not as high as expected, the SRR for small SNR seems to follow the pseudo-linear relation seen using noise-free signals for low SNR, and a plateau at $SRR \approx SNR_0$ for larger SNR. Considering that the model obtained with the simulated signal represents accurately the three simulated scatterers, the similarity between the SRR computed with the measured and with the simulated signals supports the accuracy of the scattering-centre model.

For a small amount of added noise, u_n, the total SNR is thresholded at $SNR_0 \approx 10.5\ dB$ because of the initial component, η_n. Interpretation of the results in this region requires consideration that, for $SNR \gg SNR_0$ the Monte-Carlo analysis has no real effect on the results since the main component of the total noise is constant from test to test. Nevertheless, the results can be considered as representative because the variance is relatively small for high SNR.

The similarity between the results obtained with both measured (blue) and simulated (red) signals supports the above analysis of the SRR. However the ability of the technique to accurately model the deterministic component of the signal, $\hat{\eta} = \eta$, remains an assumption.

We now examine two parameter-estimates, pole-magnitude and pole-angle as a function of the added noise. The first part shows that the number of poles selected that obey the magnitude-one criterion varies with the noise. The second part of the analysis shows that the accuracy of the pole-angle estimates also decreases with the noise. By comparing these observations with the variation of the SRR, some concerns can be raised about the reliance that can be given to the SRR as an indicator of model accuracy.

Figure 4.15 represents the proportion of selected poles whose magnitude falls between $\pm 2\%$ of the unit-radius, that is between $\rho_{min} = 0.977$ and $\rho_{max} = 1.023$. This rate, which is refered as the reliability index, remains constant at 100% for $SNR > -5\ dB$ and drops down to 94.5% for $SNR = -20\ dB$. Although this figure remains high, the susceptibility of the model to pole-magnitude implies that models may be deeply affected by the noise.

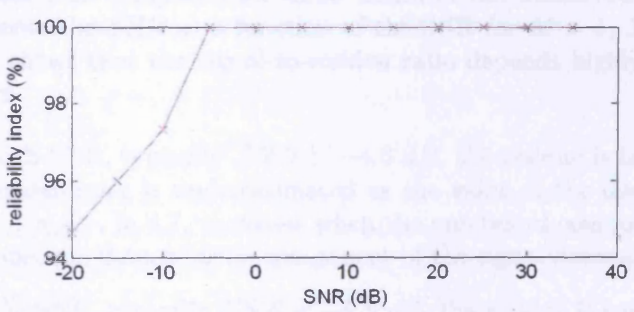

Figure 4.15: Proportion of the poles selected satisfying the magnitude-one criterion as a function of the SNR

Figure 4.16 represents the angles of the three poles selected for various SNR values. The figure shows that, for large SNR, the angles estimated are

very close to their expected values. However, it reveals that the number of spurious poles selected increases when the SNR decreases. As a matter of fact, the poles selected for $SNR = -15\ dB$ can all be considered as spurious poles. This suggests that, for small SNR, the technique may model components that are not those of the deterministic signal but probably those of the noise.

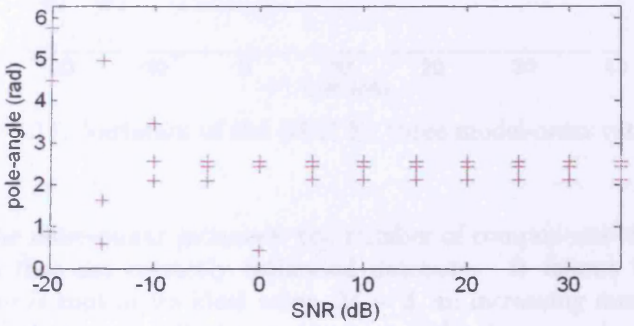

Figure 4.16: Pole-angle as a function of the SNR

Both experiments show that the noise can significantly affect the estimation of the model-parameters. The magnitude and the angle of the poles selected vary from their expected values tosuch an extent that, for low SNR, a large number of poles selected may actually be spurious poles. Nonetheless, it seems from figure 4.14 that the presence of spurious poles does not affect severely the SRR.

In order to determine the effects of the spurious poles on the model error, the SRR has been computed for three values of the model-order. Figure 4.17 represents the SRR as a function of the SNR for $M = 1$, $M = 2$ and $M = 3$. It shows that the signal-to-residue ratio depends highly upon the model-order.

- For high SNR, typically $SNR > -4.6\ dB$, the residue is larger when the model-order is underestimated as the value of the denominator, $< |\hat{s}_n - s_n| >$, in 4.7, increases when the number of components used to model the deterministic component of the signal decreases.
- For low SNR, typically $SNR < -9.5\ dB$, the residue is smaller when the model-order is under-estimated. This is due to the fact that the smaller the model-order, the smaller the number of spurious poles.
- For SNR between $-9.5\ dB$ and $-4.6\ dB$, the smaller error is logically obtained with the intermediate model-order.

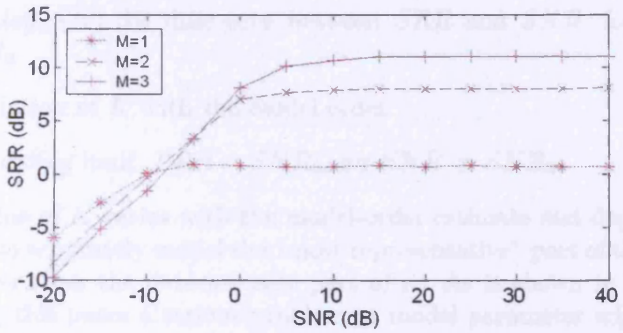

Figure 4.17: Variation of the SRR for three model-order estimates

When the noise-power increases, the number of components of the noise-free signal that are correctly estimated decreases. It follows that if the model-order is kept at its ideal value, $M = 3$, an increasing number of the poles selected may actually be spurious ones. In the case of an extended target such as a Boeing 727 which has tens or hundreds of scatterers and would logically require a very high model-order, a very large number of spurious poles is expected if the SNR is not large enough.

Taking this into account, these experiments reveal some of the problems found in using the SRR as an indicator of model-accuracy. First, for low SNR the maximum SRR is obtained with $M = 1$ component. This clearly indicates that one should not rely on the maximum value of the SRR for estimating the physical model-order. Second, although the value of K seems to vary as a function of the model order, it does not seem straightforward to detect any subspace swaps based on the SRR.

Summary

In this section, models have been estimated from simulated and measured radar signals artificially corrupted by different levels of additive white Gaussian noise. The accuracy of the models has been investigated by computing the signal-to-residue ratio which is based on the distance between the model and a chosen reference signal. For simulated signals, it is possible to compute the residue from the noise-free version of the radar signal. However, in practice, the measured signal is always corrupted by some noise and the SRR is generally computed using a noisy signal as reference, $\tilde{y} = s + \eta$.

When the SRR is described as a function of the SNR computed using the power of the additional noise, u_n, one can expect:

- a pseudo linear relation between SRR and SNR, for $SNR \ll SNR_0$

- a $10.log_{10}(K)$ dB difference between SRR and SNR, for $SNR \ll SNR_0$
- a variation of K with the model order
- a bounding limit, $SRR \approx SNR_0$, for $SNR \gg SNR_0$.

The value of K varies with the model-order estimate and depends upon the ability to accurately model the "most representative" part of the reference-signal rather than the deterministic part of it. As is shown in the following section, this poses a serious problem as model parameter adjustment is achieved by minimizing the SRR.

More critically, this section unveils a serious issue by showing that it is difficult to detect when a model is generated with wrong model-parameter values. It also shows that, for low SNR, the SRR may not be a very good indicator of physical accuracy.

4.3.3 Model-order

The previous section showed that the model-order is a critical parameter for the modelling process. In order to complete this analysis, the following example uses the same measured signal to show the variation of the signal-to-residue ratio as a function of the model-order estimate.

Figure 4.18 represents the signal-to-residue ratios obtained for various model-order estimates between $M = 1$ and $M = 40$. Each value is the mean-value of the SRR obtained for 25 tests using the same signal. The blue solid line and red dashed one represent the results obtained with the measured signal and the simulated signal, respectively.

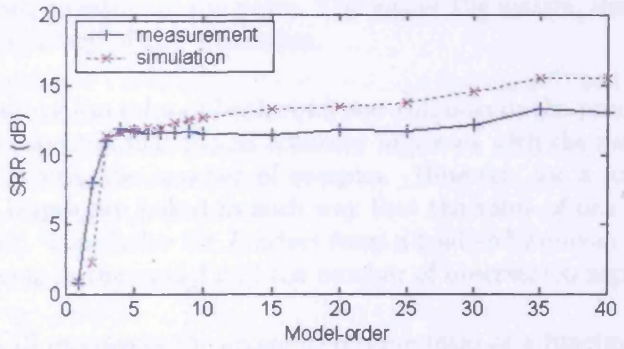

Figure 4.18: Variation of the SRR as a function of the model-order

Based on the number of physical scatterers, the expected model-order is $M = 3$. Under this assumption, the figure shows that under-estimating the model-order causes large model-error. This was expected as each scatterer contributes about one third of the signal power in this case. However, it also shows that over-estimating the order does not result in any significant increase of the residue. In contrary, the SRR seems to increase with the model-order. This result, which was already found with the Boeing 727 in figure 4.6, suggests that, for $M > 3$, the extra-poles are modelling the noise initially contained in the sequence modelled. If the signal is strongly corrupted by the noise, the SRR would be relatively high although the model is highly incorrect. This clearly shows that the SRR can only be used as an indicator of accuracy if the noise contained in the reference signal is low. Moreover, it shows that the model-order may be estimated throughout the transition of signal-to-residue ratio but certainly not from its maximum value.

4.3.4 Matrix proportion

The data set is organised into a quasi-symmetrical matrix whose dimensions constitute one of the degrees of freedom of the technique. This section is interested in the effect of the matrix proportion on the residue.

The matrix width, L, which is the size of the observation-window defines the number of terms that form the auto-regressive equation in 3.19 or equivalently the length of the sequence needed to characterise the physical mechanism observed. The value $L-1$ defines the maximum number of poles that can be estimated from the matrix. It is thus required that the value of L be large enough to retrieve all the scattering-centres.

The matrix length, $N - L + 1$, corresponds to the number of observation-windows used to estimate the poles. The longer the matrix, the greater the statistical accuracy of the estimation.

As a result of the roles of both rows and columns in the processing technique, it is expected that model accuracy increases with the matrix dimension, that is with the number of samples. However, for a fixed dataset, width and length are linked in such way that the value of one has reliance on the other. The choice for L arises from a trade-off between the number of components in the model and the number of observation segments.

Figure 4.19 represents the signal-to-residue ratio as a function of the parameter L expressed here as a proportion of the total number of samples, $N = 128$. The blue solid line and red dashed one represent the results obtained with the measured signal and with the simulated signal respectively.

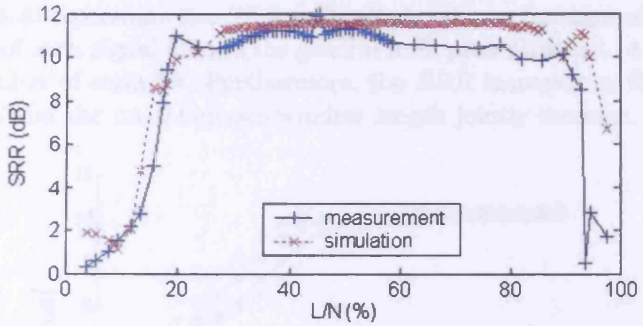

Figure 4.19: Variation of the SRR as a function of the matrix width

The figure shows that the model accuracy depends upon the value of L. For L between 20% and 90% of N, the model accuracy is relatively constant. Beyond those limits, the model accuracy drops significantly for both the simulated and measured signals as expected. The recommendation in [26] is supported as the maximum SRR is obtained for L between $N/4$ and $N/2$ with a maximum at about $L = N/3$.

4.3.5 Number of samples

Introduction

The dataset employed is a complex-valued signal composed of N samples where each sample, s_n, is the base-band response corresponding to frequency $f_n = f_0 + n.\Delta f$. Due to the nature of the technique employed, the accuracy of the model is expected to increase with the amount of information processed, that is with the dimension of the dataset. However, it is not possible to increase the number of samples while keeping both the bandwidth and the frequency-step constant as $B = N.\Delta f$. For this reason, the relation between the number of samples and the model accuracy is investigated in two steps. First, the number of samples is increased while maintaining the frequency-step constant. Second, it is increased while maintaining the bandwidth constant.

Variation of the frequency-step

In the first experiment, the variation of N is achieved by varying Δf while keeping the B constant. Four test signals are constructed by sampling the same signal composed of 128 samples at different rates. The resulting four signals are composed of $N = 16,\ 32,\ 64$ and 128 samples. For each signal, the model is computed using a matrix-width, L, set to $N/3$.

Figure 4.20 represents the SRR for each signal as a function of the SNR. The SRR of each signal follows the general form presented in 4.14 regardless of the number of samples. Furthermore, the SRR increases as the number of samples and the unambiguous window length jointly increase.

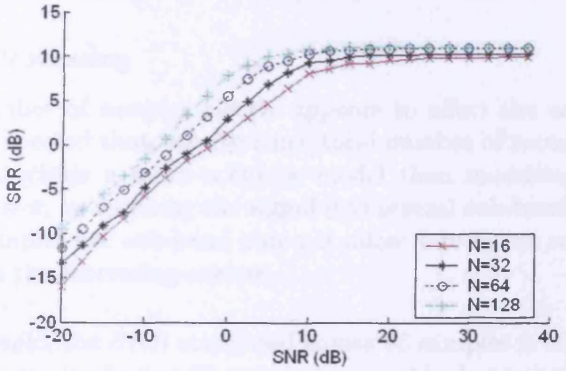

Figure 4.20: Variation of the SRR as a function of the frequency-step

Variation of the bandwidth

In the second experiment, the variation of N is achieved by varying B while keeping Δf constant. Four test-signals are constructed by selecting the first $N = 16,\ 32,\ 64$ and 128 samples of the reference-signal as above. For each signal, the model is computed using a matrix-width, L, set to $N/3$. Figure 4.21 represents the SRR for each signal as a function of the SNR.

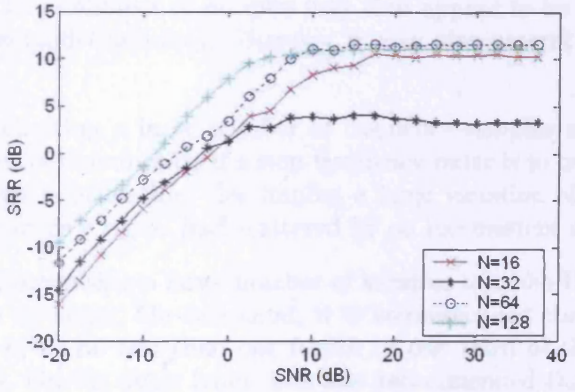

Figure 4.21: Variation of the SRR as a function of the bandwidth

As the results obtained for large SNR are not statistically representative it is prefered to attach more importance to the value obtained for low SNR. Here again, the SRR increases as the number of samples and the bandwidth jointly increase. The particular effect of increasing the bandwidth in comparison to increasing the frequency-step is discussed below.

Sub-band Processing

As the number of samples clearly appears to affect the accuracy of the model, it is expected that, for the same total number of samples, modelling a single band yields a more accurate model than modelling several sub-bands. Moreover, by splitting the signal into several sub-bands, the reduced number of samples per sub-band may not allow L to be set sufficiently high to retrieve all the scattering-centres.

As an example, the SRR computed across 96 samples is $SRR = 13.9\ dB$ for a model determined using 96 consecutive samples but only $SRR = 3.1\ dB$ for a model computed from two sub-bands of 48 samples separated by 32 samples. It is therefore recommended to model a signal defined on a single sub-band in this case. However, processing several sub-bands may yield a more accurate model if bandwidth prediction has to be achieved. In that case the accuracy will obviously depend upon the size of the missing band.

Discussion

All the experiments presented in this section show that the SRR increases with the number of samples, N and more specifically with the number of samples per sub-band. This result was expected as a coherent process is employed. A large number of samples may thus appear to be a solution for enhancing the model accuracy. However it may also present some serious drawbacks.

- First, collecting a large number of frequency-samples may require a long time of illumination if a step-frequency radar is to be used. When the target is in motion, this implies a large variation of aspect-angle and therefore a signal backscattered by an inconsistent target.
- Second, organising a large number of samples into the Hankel matrix may be an issue. On one hand, it is recommended that the matrix width, L, be no less than one fourth or one third of the number of samples. On the other hand, it is also recommended that it be small enough to limit the computational load of the system and to avoid the problems associated with rejecting the $L - 1 - M$ spurious roots. For this reason, depending on the model-order expected, a large number

of samples may not always be an optimal option with the current technique.

- Third, increasing the number of samples may not be desirable as it affects either the frequency-step or the bandwidth. When this is achieved by reducing the frequency-step size, a large number of samples may require such a narrow step-frequency that the target size represents a much smaller ratio of the unambiguous range window. That implies that the fluctuations of phase in the system are relatively greater. Alternatively when the frequency-step is kept constant, increasing the number of samples may require a very large bandwidth. This may not be possible due to hardware limitations, regulations or interference from neighbouring sources. Considering that it is possible to transmit such a wide bandwidth, the scattering mechanisms occuring at the lowest frequency may be different from those occuring at the highest frequency. This problem, encountered with ultra-wide band radar, is likely to characterise targets whose structural components are very different in size and shape. It does also imply that approximations made to enable the modelling of non-linear mechanisms would appear more obviously over a wide bandwidth. In addition, the high-resolution signal may reveal such a large number of small scatterers that the model may not include the desired ones due to limitation of the model-order by the noise for example.

In spite of its many advantages, processing a large number of samples may not always be practical or desirable. The next section shows that if the number of samples is so small that the bandwidth does not enable the scatterers to be resolved, the performance may still be greatly affected.

4.3.6 Spatial distribution

Introduction

Conventionnally, the bandwidth determines the minimal separation between scatterers that allows their resolution in range. Super-resolution techniques can be used to increase the resolution but ultimately the results are limited by the initial bandwidth. The latter is therefore a key factor of the model accuracy. For this reason, a special interest is put into the study of the effects of the bandwidth on the modelling process.

It has been said that varying the bandwidth can be achieved in several ways. One method consists of varying the number of samples, N, but the subsequent modification of the number of Fourier-cells per unambiguous range-window, $R_u = c/(2\Delta f)$, affects the SNR at the output due to the coherent nature of the technique. A second method consists of varying the

frequency-step, Δf, while conserving the same number of samples. This conserves the ratio between the nominal resolution and the unambiguous range window but modifies the ratio between the target size and the unambiguous range window. For the sake of this study, the approach taken in this section consists of downscaling the distance between scatterers. By acting directly on the target, this method keeps the number of Fourier-cells per unambiguous range-window and the ratio $\Delta f / R_u$ constant.

Variation of the scatterers' distribution

The turntable on which the three spheres lay, is rotated by steps of 0.5°. For each position, N narrow band pulses are used to form one range-profile. The rotation modifies the position of the scatterers and subsequently the distribution of the scatterers in range. After a total rotation of 100°, the dataset obtained contains 201 measurement for which the three scatterers have different spatial distributions between each other.

The modelling technique is then applied to these 201 snapshots with L set to $N/3$. The resulting models are then compared with their respective reference-signals. Figure 4.22 represents the SRR for each position of the turntable, and is computed with the models obtained by linear least-squares (top) and by non-linear least-squares fitting (bottom) using the Gauss-Newton algorithm.

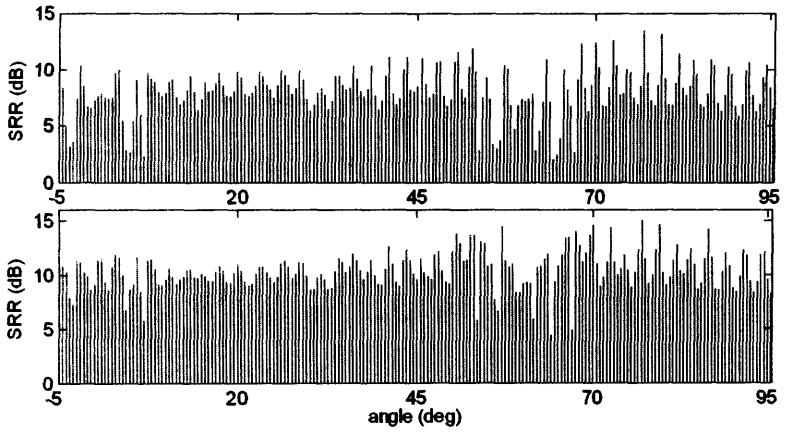

Figure 4.22: Variation of the model-error as a function of the position of the turntable using LLS fit (top) and NLLS fit (bottom)

The figure shows that the model accuracy as defined by the SRR is relatively constant over the 100° rotation of the turntable. On average, the SRR of the models obtained by linear least-squares (top) is about 8.5 dB and

the adjustment by non-linear least-squares enables a gain of about 1.5 dB. Locally, the SRR values drop down by 5 dB in four regions corresponding to positions centred on aspect-angles $\phi = -2°$, 8°, 53° and 63°.

A comparison with the actual position of the turntable shows that the angular regions of poor model-accuracy are those for which the separation between two balls in range is relatively small but not zero. This can be more easily observed in figure 4.23 which shows the pole-angle of the three selected poles for each position of the turntable. The same displaying method is employed ; the poles adjusted by non-linear least-squares fitting using the Gauss-Newton algorithm are represented at the bottom.

Figure 4.23 suggests that when two spheres are closely spaced in range, one pole-estimate is generally a spurious one. For $\theta = 60°$, one pole is associated with the scatterer whose range has the smallest variation, another pole is associated with the two scatterers at similar range, and the third pole is obviously a spurious one.

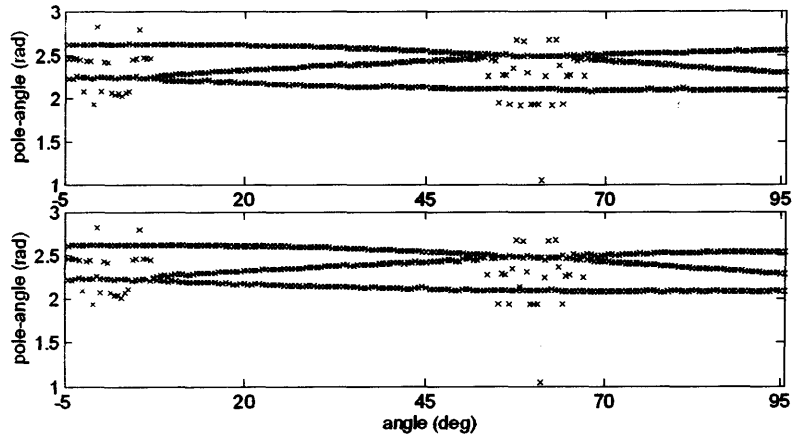

Figure 4.23: Variation of the pole-angle estimates as a function of the turntable using LLS fit (top) and NLLS fit (bottom)

Figure 4.24 represents the amplitude-coefficients determined by linear least-squares (top) and non-linear least-squares fitting (bottom). It shows that some coefficients are subject to rapid variations which may be due to the compensation for the errors on the pole estimate or for multipath effects created by the interactions between scatterers.

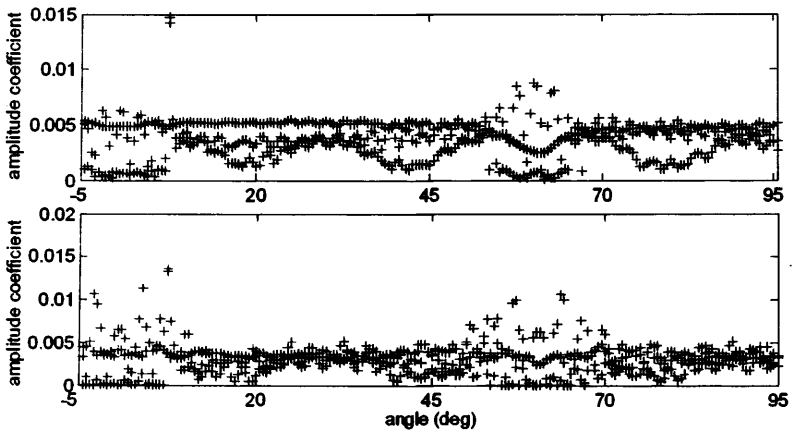

Figure 4.24: Variation of the amplitude-coefficient estimates as a function of the scatterers distribution in range using LLS fit (top) and NLLS fit (bottom)

The effect of a limited bandwidth on the SRR can be explained as follow. When the two scatterers have very similar ranges, the approximation of the return using one single pole with a greater amplitude-coefficient is relatively accurate. This explains why the model error is relatively small for aspect-angles 3° and 58° which are approximately the aspect-angles that correspond to positions where two scatterers have similar range. However, the model-error rapidly increases with the distance between the poles. This explains why the error is much larger for aspect-angles around $-2°$, 8°, 53° and 63°. For the other positions, the distance between scatterers is relatively large with regards to the nominal resolution to enable full resolution. In this case, the three scatterers are accurately represented by three poles and the model-error is relatively small.

4.4 Limitation of the technique

4.4.1 Introduction

In this section, the results from 4.3 are extended and generalised. First, the model accuracy as defined by the signal-to-residue ratio is investigated. It is shown that the results obtained by using this expression must be considered carefully. Second, the case of a deficient model is considered and it is demonstrated that the approximation of several scatterers by a single one could be the principal cause of modelling error.

The analysis provides valuable insight into the method performance. Those results are seen as key because they begin to explain the limitation of the technique not only for the case of the Boeing 727 presented at the beginning of this chapter but also for the more general case of man-made targets composed of a large number of strong scatterers or composed of complex scatterers. It is also extremely relevant as it applies to many areas of radar including imaging, classification and bandwidth extrapolation. It finally opens the way to the classification method called MAUCAZ that is introduced in Chapter 5.

4.4.2 Indicator of accuracy

First let us recall that we have shown that the signal-to-residue ratio, as defined by 4.6, cannot be considered as a robust indicator of physical accuracy. This is supported by two points encountered in the study:

- The SRR generally increases with the model-order estimates because of modelling of the noise contained in the noisy reference-signal by the extra poles. For this reason, the model-order cannot be routinely estimated from the maximum SRR value.
- For low SNR, the most accurate model is found when the model is under-estimated. This is due to the fact that the model contains fewer poles representing the noisy components of the corrupted signal. For medium SNR the most accurate model is obtained with the intermediate model-order, and so on. Here again, the number of scatterers cannot be estimated from the maximum SRR value.

Both points show that the most accurate parameter-estimates cannot always be determined by minimising the residue. In addition, they show that the use of the SRR for measuring the model accuracy may not provide results on which one can rely to decide whether a model can be extrapolated. It follows that models that seem mathematically accurate may not be physically accurate and therefore may not be suitable for extrapolation.

The main problem comes from the fact that the accuracy can only be evaluated if the reference-signal is close to the deterministic form of the signal backscattered by the target and if it exhibits large enough content of information to remove any ambiguity. One could consider that the accuracy of the assessment is limited by the accuracy of the scattering-centre model that could be extracted from the reference-signal.

To illustrate this fact one can consider two range-profiles of two different targets; the first one composed of two close scatterers, the second one composed of one scatterer only. At poor resolution, the range-profiles may appear to be similar. However, for greater bandwidth the profiles would appear to be very different if the scatterers are resolved. It follows that using a low-resolution signal as a reference would not enable a good assessment of the accuracy.

In general, the signal that should be used as a reference is not available and the signal that is used instead is a noisy signal from which can only be extracted the same amount of information as the signal modelled. In practice it may often be the same. This limitation is common to most fitting problems.

In order to obtain a fair estimation of the model accuracy, one would need to compare the model with the reference-signal over a number of samples that is larger than the number of samples which was used for modelling the signal for example.

One obvious solution consists of comparing the extrapolated model with a version of the signal defined across a wider band. In practice, the determination of the model would not make use of all the information collected and such a method could be described as a destructive one. Although this would not be an issue for simple targets because the amount of information needed is relatively small, it would be a serious drawback in the case of extended targets with low signal-to-noise ratio as it has been seen that the greater the number of samples, the greater the accuracy.

Another solution may be to use a reference signal with high signal-to-noise ratio. For targets that are well known and can be experimentally tested before the measurement, it may be possible to determine the reference-signal independently of the measurement either by simulation or measurement. However, the variation between the reference target and the illuminated target would be an issue. If the difference is too large, this method would not allow any actual improvements.

4.4.3 Deficient model

Background

Inspired by the previous experiment, this section considers the case of a signal that is approximated by a deficient model. This situation typically arises because of a wide range of reasons including:

- limited SNR when the model represents the components of the noise rather than the components of the signal,
- limited bandwidth when the model approximates several scatterers by a single one due to lack of resolution,
- incorrect estimation of the model-order when the technique used to estimate the model-order is inaccurate,
- limited number of samples when the maximum model-order allowed by the matrix width is not large enough,
- sources of interference when the presence of interference may prevent the technique extracting some of the scattering-centres, and
- complex scattering mechanisms when a large number of scattering-centres are employed to describe the complex contributions of a single scatterer.

Pole estimation and fitting technique

It is relatively well known that the performance of super-resolution algorithms is limited by the bandwidth. Even with such algorithms, two scatterers closely spaced in range may not be resolved if the bandwidth is not large enough. In this case, limited bandwidth may result in the selection of two poles for which the first is an approximation of the two true poles and the second is therefore the next pole whose magnitude is the closest to one, that is a spurious pole.

When the noise-power is small, the determination of the amplitude coefficients by fitting techniques ensures that the effect of the spurious poles can be neglected. Nevertheless, this may not be the case when the noise-power is high. Moreover, the effect of a deficient model on the model-error may be significant if the scatterers are not close enough to be accurately approximated by one unique pole.

The following experiment shows that linear and non-linear least-squares fits may cause very different model-errors for the very reason that when two scatterers are not closely spaced enough to be properly approximated by one single scatterer, the pole-estimate depends upon the fitting technique employed.

For this, we consider figure 4.25 which represents the real range-profile (solid line) and the model-based range-profile (dashed line) for the signal obtained at aspect-angle $\theta = 45°$ of the turntable. Here, the model-order is set to $M = 1$ instead of $M = 3$. The models are obtained directly by linear least-squares fitting in the first case (top) and after adjustment by non-linear least-squares fitting using the Gauss-Newton algorithm in the second one (bottom).

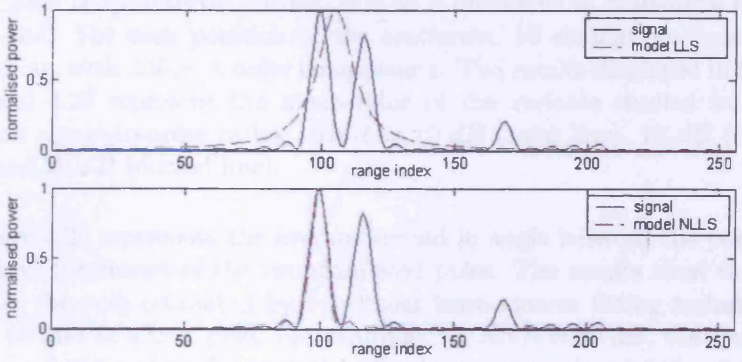

Figure 4.25: Influence of the parameter-adjustment stage on the range-profile of a deficient model

Several observations can be made on this experiment:

- the pole estimated directly by the root-MUSIC algorithm could be described as an approximation of the two closely spaced scatterers. The pole-angle can be approximated by the mean-value of their angles.
- the model undergoes significant changes when the parameters are adjusted by the non-linear least-squares fitting technique. The pole cannot be seen as an approximation of two closely spaced poles but as a very accurate reproduction of one of the scatterers instead. It appears from figure 4.22 that the accurate estimation of a single scatterer generates a smaller model-error than the approximation of two scatterers.

When one pole is used to model two closely spaced scatterers, the pole estimate computed with the linear least-squares fitting technique has a rela-

tively large magnitude. The effect on the range-profile is a wider peak which overlaps with the two true peaks obtained from the signal. This is a key element in the understanding of the problem of stability.

In order to verify that this case is representative of the general phenomenon, a similar experiment has been performed with two simulated point-scatterers. The signal used is computed using expression 4.16.

$$s(n) = 1 + e^{i\frac{2\pi.3m}{13}n} \tag{4.16}$$

where $m = 0...12$ and the total number of samples $N = 128$.

While the first scatterer is maintained at a given position, the second one is moved to 13 different positions linearly shifted from 0 to 3 Fourier-cells. This range-interval corresponds to a difference in pole-angle of 0 to 0.147 *rad*. For each position of the scatterers, 50 simulations have been carried out with different noise components. The results displayed in figures 4.26 and 4.27 represent the mean-value of the variable studied for three different signal-to-noise ratios: $SNR = 10\ dB$ (solid line), 15 dB (dashed line) and 20 dB (dotted line).

Figure 4.26 represents the average spread in angle between the pole estimate and the closest of the two simulated poles. The results show that the angle of the pole estimated by non-linear least-squares fitting technique is closer to that of a true pole. For example, for $SNR = 20\ dB$, the spread is less than 0.017 *rad* in the case of LLS whereas it reaches 0.046 rad in the case of the NLLS.

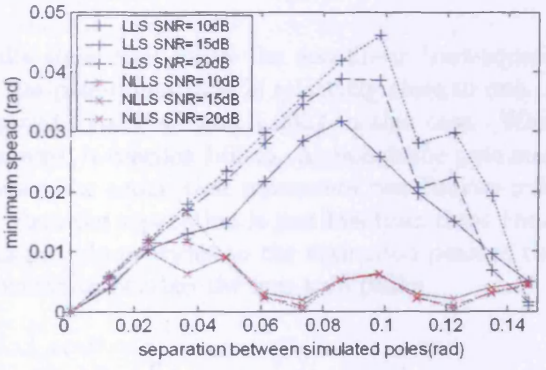

Figure 4.26: Influence of the separation between scatterers on the estimation of the pole-angle in the case of a deficient model

When linear least-squares is used, the spread is about half the value of the separation between simulated poles. That supports the idea that the peak is located half-way between the two true peaks. This is only true for a small separation, typically when the poles are separated by less than two Fourier-cells. Beyond this value, the poles are resolved and the peak associated with the pole-estimate becomes closer to one of the true poles. For a separation equal to three Fourier-cells, the pole-angle estimates obtained using linear and non-linear least-squares fitting are relatively similar and very close to one of the correct values.

The same analysis has been carried out on the pole magnitude parameter. Figure 4.26 represents the values of pole-magnitude obtained as a function of the separation between the scatterers.

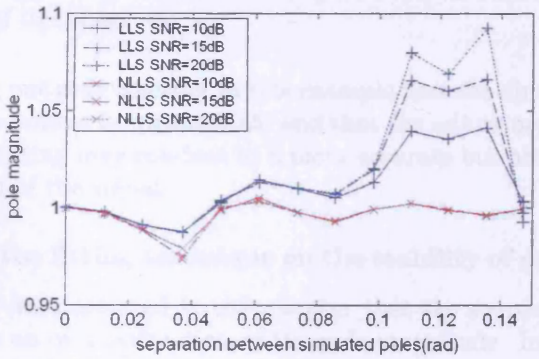

Figure 4.27: Influence of the separation between scatterers on the estimation of the pole-magnitude in the case of a deficient model

These results show that when the non-linear least-squares fitting technique is used, the pole-magnitude is relatively close to one. As a matter of fact, it is bounded by 0.9743 and 1.0052 in this case. When linear least-squares is employed, it reaches 1.0925. Although the pole magnitude is very close to one when the separation represents two Fourier-cells, the greatest error is found when the separation is just less than three Fourier-cells. Such a large pole-magnitude provides to the estimated peak of the range profile the necessary width to overlap the two true peaks.

Limitation

To sumarise the above, model-parameter estimates vary depending on whether they are obtained directly or after adjustment using non-linear least-squares fitting. It was shown that the model may be highly inaccurate

when two scatterers are closely spaced. Both figures 4.26 and 4.27 confirm that the difference of behaviour seen in figure 4.25 is statistically consistent.

For LLS, the difference between the pole-angle estimates is small when the separation between the two scatterers is either very small or very large, typically greater than two Fourier-cells. Similarly, the pole magnitude estimate is found to be greater than one when the separation between the two scatterers is between two and three Fourier-cells.

For NLLS, the solution can be considered as physically more accurate in the sense that the results model one of the scatterers relatively accurately. The pole-magnitude is relatively close to one in this case. However, the experience shows that this is not a general rule as non-linear least-squares fitting may degrade the values of the parameter-estimates for modelling components of the noise.

To simplify, one may consider in this example that the direct estimation of the scattering-centres is approximate and that the adjustment by non-linear least-squares fitting may conduct to a more accurate but obviously deficient representation of the signal.

Influence of the fitting technique on the stability of deficient model

It has been demonstrated in this chapter that the source of the greatest model-error is an over-estimation of the pole-magnitude. In this section, it was shown that this particular problem occurs when models approximate two closely spaced scatterers with a single scattering-centre. Although this point is not stressed in the literature, it is perceived here as a critical one, especially because this problem potentially concerns all complex man-made targets.

For accurate bandwidth extrapolation, the accuracy, the completeness and the stability of the model are necessary conditions. However, there are various factors which may lead to situations where the model cannot be accurately extrapolated. First, whereas a given model may be considered as accurate because it closely matches the signal, it may not be stable due to proximity of two scatterers. Second, one should also consider that a model whose order is sufficiently large may approximate not only the target but also the noise or interference that is contained in the reference-signal. Third, the scattering-centre model is only an approximation of scattering mechanisms that are probably far more complicated. Because of this, the determination of the model-parameters by optimising a corrupted fitting-problem cannot ensure that the solution enables an accurate extrapolation of the model across a wider bandwidth.

Example

To complete this analysis, the initial example using a signal backscatterered by a Boeing 727 and presented at the beginning of this chapter is revisited. The signal-to-residue ratio has been computed for various models as a function of the model-order between $M = 1$ and $M = 23$.

Figure 4.28 presents the results by three pairs of lines. Each couple represents the SRR obtained with two models; one determined using linear least-squares (solid line), the second by non-linear least-squares (dashed line) fitting techniques. The first pair of models are determined by direct reconstruction of the 128 sample-signal. The second pair of models are determined by interpolating the model obtained from the first and the last 48 samples of the signal. The third pair of models are generated by extrapolating the model determined from the first 96 samples of the signal. For each pair of models, the SRR is finally computed across 128 consecutive samples.

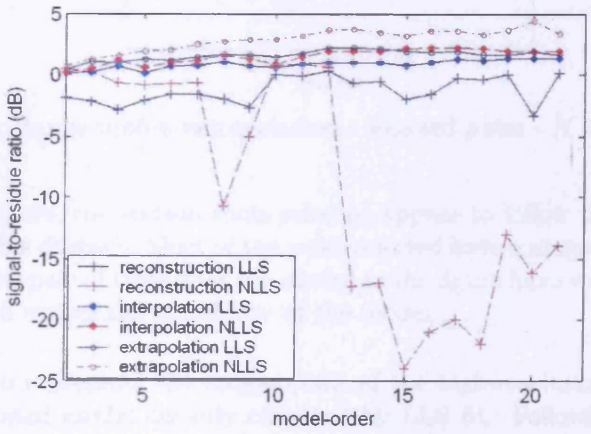

Figure 4.28: SRR as a function of the model-order for direct reconstruction ($N = N' = 128$ samples), interpolation ($N = 2 \times 48$ to $N' = 128$ samples) and extrapolation ($N = 96$ to $N' = 128$ samples)

As shown in this chapter, the SRR globally increases with the model-order and that there is no sharp transition and therefore no element that can be used to estimate the model-order. The figure shows that maximum accuracy is obtained by reconstructing the model using NLLS. The reconstruction by LLS and the interpolation using NLLS are almost as accurate. This may be due to the fact that the missing band only represents 25% of the total band. The extrapolated models are both poorly accurate as the SRR is typically below 0 dB.

The thesis presented in this chapter suggests that the principal source of error comes from the model instability which is linked to the pole-magnitude. In order to illustrate our analysis, the model computed from the first 96 samples for $M = 16$ has been taken as an example. Figure 4.29 represents the selected poles computed by applying the modelling technique to this signal.

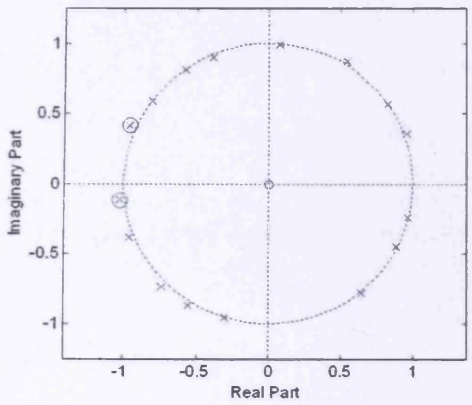

Figure 4.29: Range-profile extrapolation - selected poles - $N = 96$ samples

On the figure, the sixteen roots selected appear to follow the thesis formulated in this chapter. Most of the poles selected have a magnitude greater than one. The pair of them that are circled in the figure have very high magnitude, which causes the instability of the model.

Figure 4.30 represents the range-profile of the high-resolution signal and the extrapolated model directly obtained by LLS fit. Following the zero-padding operation, the poles circled are associated with peaks at range-index 67 and 1006 on the figure.

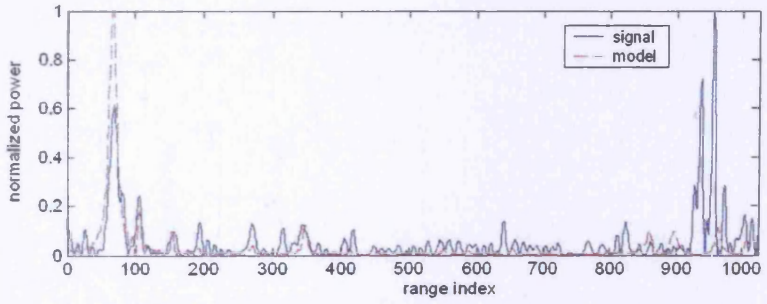

Figure 4.30: Range-profile extrapolation - $N = 96$ to $N' = 128$ samples

The figure confirms that the approximation of several components closely spaced in range by one single pole leads to unstable model that cannot be used to extrapolate the signal. . It is not clear whether this is due to the closeness of several scatterers in range, to the complexity of the scatterers or to the noise but the following clearly shows that it is related to the deficiency of the model.

4.5 Conclusion

4.5.1 Summary

In this chapter, it was shown that the modelling technique does not always perform with great accuracy. Using a signal backscattered by a Boeing 727 as an example, it was shown that when extrapolating the model considered as very accurate, the predicted samples are far from matching the signal. This example is used as the basis for challenging the idea that the modelling technique can be applied to all kinds of man-made targets.

For supporting this position, the model and the modelling technique have been studied extensively. Both simulated and measured signals have been employed in order to determine the sensitivity to their parameters and the limit of utilisation. The parameters investigated include the signal-to-noise ratio, the estimated model-order, the dimension of the matrix, the number of samples, the frequency-step, the bandwidth and the separation between scatterers in range.

Both theoretical and empirical analysis agree with the results found in the literature including the importance of a large signal-to-noise ratio and the recommended value for the matrix width. They have also contributed to understanding the effect of each parameter in the determination of the model parameters. Moreover, it was also shown that the extrapolation is very sensitive to the pole magnitude and that this parameter is estimated with varying accuracy depending on factors such as the target complexity with respect to the signal.

When dealing with extended and complex targets like aircraft, it is very likely that ideal conditions are not met. Therefore, it is important to consider the estimation of deficient models as it seems to be one of the principal sources of large error. The results of this section can be used as a guideline for applications where man-made targets are illuminated. However, amongst all them, the results that are most important to the scope of this thesis are summarised in the following.

4.5.2 Key results

Model accuracy

It has been shown that a model considered as mathematically accurate may be physically inaccurate. Measuring the accuracy of a model is only relevant when the reference model is close to the deterministic form of the signal and when the amount of information that can be extracted from the reference-signal is sufficient. In practice, the reference-signal may often be

the signal modelled, that is a narrow-band signal backscattered by a moving target in motion with risk of interference and low signal-to noise ratio. In this case, the signal-to-residue ratio cannot be considered as a good indicator of model accuracy simply because the reference-signal is of poor quality.

Furthermore, it has been demonstrated that assessing the model accuracy is a complicated task that cannot be based on the value of the residue only. The accuracy has to be assessed with respect to the application of interest. In practice, the decomposition of the signal into a sum of elementary signals is used for data compression but also for data extrapolation, target imaging and target classification. For data-compression, one may consider that the performance can be assessed through the ability to generate a model in which samples are as close as possible to the signal samples. It is also reasonable to assume that, for other applications, the performance depends upon the ability to decompose a signal into a sum of physically accurate elements, that is scattering-centres whose parameters are close to the expected parameters. In this case, optimising the distance between the model and signal is not a primary goal but only a chosen way for both estimating the model parameters and assessing the accuracy of the resulting model. For this reason, it is generally not suitable to rely on the signal-to-residue ratio for estimating whether a model is accurate and can be extrapolated. Moreover, when this is possible, it would be perhaps more suitable to evaluate the accuracy of the model throughout the distance between the parameter-estimates and their expected values. This is the approach chosen for the classification technique presented in the next chapter.

Limitations of the technique

Following the results of the experiments described in this chapter, the technique appears to be limited by several factors including the number of samples, the bandwidth, the interference, the matrix dimensions, the complexity and motion of the target and also by other factors such as noise and interference. A thorough study of the model itself and of the modelling technique have enabled the identification of what is seen here as the principal cause of error. When a single scatterer is used to model two scattering-centres, the solution obtained by the modified root-MUSIC algorithm and linear least-squares fitting is a pole which can be described as a approximation of both poles. On the range-profile, the estimated pole appears as a peak located between the two expected peaks and it is much wider than the peaks, which creates a partial overlapping.

The analysis of the model itself in the first part of this chapter shows that the solution obtained with a deficient model would be responsible for very large errors. First, the pole-angle estimate is actually far from both poles

and, as a matter of fact, we know that the pole-angle affects the results of the extrapolation. Second, and more critically, the large peak which is characteristic of a deficient model is mathematically caused by a pole-magnitude greater than the magnitude of both poles, and typically greater than one. This shows that, for an extended target with a large number of scatterers or with a low signal-to-noise ratio, the pole-magnitude estimates is likely to be incorrectly estimated. More critically, it has also been stressed that, for values greater than one, the larger the magnitude, the greater the instability of the model. This particular problem could be one of the principal causes of the error when modelling and extrapolating the signal backscattered by a Boeing 727 and more generally by real extended targets such as aircraft in non-ideal conditions.

It has been shown that the determination of the model may be improved by using a non-linear least-squares fitting technique. In this case, the pole estimate would be very close to one of the two poles. This result is a partial but physically accurate representation of the initial signal. Because the model is computed by non-linear least-squares, the adjustment of the parameters may often lead to a very erroneous solution. This varies upon the initial estimation by linear least-squares. The main drawback is that this technique can only represent some of the scatterers. When the missing scatterers encompass a large part of the signal, the extrapolation of such deficient model is obviously inaccurate.

The results from this study show that the current technique may be able to model the signals scatterered by an extended target with good accuracy, providing the model-order, the signal-to-noise ratio, the bandwidth and the number of samples, are large enough. However, it is expected that for most real extended or complex targets, the diversity of the scattering mechanisms that are responsible for the received signal cannot be extracted due to the poor quality of the received signal. When the signal is modelled, a large model-order allows the signal to be accurately reproduced. This is a simple mathematical relation. However, the model is not sophisticated and not accurate enough to be extrapolated correctly. This poses serious threats on the capability to enhance the bandwidth as it has been shown that extrapolation is very sensitive to pole magnitude which is the model-parameter approximated and often incorrectly estimated. Based on this analysis, it is proposed to rely on the information that can be correctly estimated or the information that does not need to be correctly estimated to enhance the performance of applications such as target classification.

Chapter 5

TARGET CLASSIFICATION

5.1 Introduction

This chapter is concerned with radar non-cooperative target recognition and target classification. The ability of a radar to perform these tasks is an important requirement for traffic management and security purposes. They are typically achieved by means of a classifier whose role is to associate an unknown target with some others based on similarities in their electromagnetic signatures. The principle of target recognition relies on the fact that the deterministic parts of two radar-signals are similar when the conditions of measurements and the targets are similar. When designing a classifier, it is expected that these conditions and the targets themselves may not be exactly identical. For this reason, it is generally required that the classifier relies on information that makes it more sensitive to the variations of target structure than to other factors such as small variations of aspect-angle.

Amongst all types of signatures that can be employed for target classification, one-dimensional range profiles have been extensively used during the last decades [19], [30], [33], [55], [56]. Compared to more sophisticated types of signatures, they can be seen as a low-cost solution mainly due to the fact that a range-profile can be obtained with a single radar. They are also relatively immune to motion-induced errors due to the limited time on target. This makes it an attractive solution for non-cooperative target recognition. In general, the signal at the receiver is pre-processed so that the comparison is performed on a reduced dataset or features of spectra. Thus, the task necessarilly involves the creation of feature-vectors that contain a limited number of attributes derived from the data. The vectors capture the information that enables target differentiation. It follows that their number is a trade-off between the dimension and the amount of information that unam-

biguously describes the target. Thus, ideally, the features are composed by independent discriminating attributes, which ensure no redundancy.

Once the feature-vectors are formed, they are compared and arranged into classes. The feature-vectors that belong to one class are all different from each other but relatively similar compared to those of other classes. In that sense, classification can be seen as the separation of data based on boundaries defined in the so-called training stage. Common examples of classifiers include correlation-filters, K-nearest-neighbours and neural networks. These techniques have been the subject of extensive studies and continue to attract the interest of many scientists in various areas. For target recognition, the main challenge consists of designing a classifier that performs a high enough rate of correct recognition at low-cost and with an acceptable misclassification rate. More generally, the cost may be thought of being caused by the parameters of the illumination (*e.g.* waveform type, aspect-angle), the capability to remove the undesired contributions (*e.g.* target motion, noise, clutter), the processing time or the creation of a library of templates.

This chapter introduces the use of the scattering-centre model's parameters for target classification. First, basic classification theory is presented. The conventional technique based on correlation of range-profiles is illustrated with an example involving real radar-signals measured on scale-model aircraft. Second, the radar signals are replaced by their corresponding scattering-centre models. Classification results show that the performance is equivalent, which confirms the capability of a scattering-centre model to reproduce the discriminating attributes of a range-profile. In order to enhance the recognition of similar-looking targets, a third experiment involving bandwidth extrapolation is carried out but the performance obtained is poor. These results defend the hypothesis which states that the estimated scattering-centre models are generally deficient, often physically incorrect and therefore cannot be sufficiently accurately extrapolated [8] [9]. As an alternative to the existing techniques, a novel type of classifier has been designed based on the results of investigations presented in the previous chapter.

The eventual technique for target recognition proposed in this chapter relies on a novel feature-based classifier which operates directly in the z-plane. Instead of comparing the signals directly, this technique processes the information related to the poles of the scattering-centre model. This information is extracted from a complex-valued radar signal and used to form feature-vectors that are stored in a library. A similar operation is performed on the test-signal. The classifier attributes a class to the target by comparing these feature-vectors. Similar techniques have been presented by Xun in

1997 [54] and by Hussain in 2001 in [20]. In the first case, the M strongest scatterers were used while all the poles were used in the second one. The originality of the algorithm presented here lies in the fact that the poles compared are those that maximise the likelihood function. It is a matching algorithm using a clustering approach in the z-plane (MAUCAZ). After applying the different classifiers to the same radar data, the results reveal that MAUCAZ has a good overall performance and, more importantly, performs better than traditional correlation-based techniques for a sufficiently high signal-to-noise ratio.

5.2 Principle of classification

5.2.1 Basics

Classification is a typical processing stage for non-cooperative target recognition. It consists of dividing data into categories or classes. For recognition, classifiers operate on back-scatterered signals which vary with the type of target illuminated and the aspect-angle of the target during the measurement. A classifier is trained with radar signals that can be labelled using these parameters. In practice, a classifier attributes a class to signals which share common properties. In radar, the reflectivity functions retrieved from the backscattered signals are commonly used to classify the targets. The methods used are said to achieve a supervised classification because they rely on pre-defined categories. They are employed in many applications including non-cooperative aircraft recognition since they allow classification of targets to be carried out remotely.

A complete recognition system generally consists of four stages: data acquisition, pre-processing, feature-extraction and classification. This framework is represented by figure 5.1.

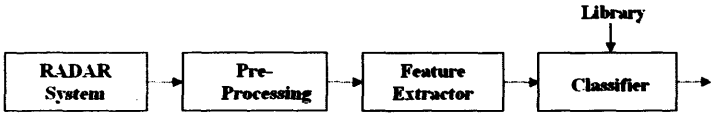

Figure 5.1: Principle of target classification

The acquisition of data is carried out by a radar-system measuring the signal returned by an airborne target. The signal collected at the receiver contains the information related to the target but also related to additional elements such as clutter and noise. A pre-processing stage, dedicated to preparation of the data for feature-extraction, can thus be employed to eliminate some of these undesired contributions. The signal supposedly cleaned from external contributions is then formatted to correspond to the standard required for feature-extraction. The latter stage consists of selecting the data that are appropriate for classification. A feature-vector can be formed by observable attributes, such as peak-amplitude, peak-width or distance between peaks. Feature-vectors can also be formed using the envelope of a range-profile. In this case, one refers to a model-based classifier. Finally, the classifier itself is designed using training sets of exemplar signals. For aircraft recognition, it is common to build a library of measured range-profiles. Recent works concern the design of a classifier using aircraft range-profiles simulated by electromagnetic prediction-codes [16] [55]. We now consider these aspects of classification in more detail.

5.2.2 Correlation filter

Correlation filters have been widely used for comparing aircraft signatures [19],[27], [28]. Essentially, the cross-correlation of two radar signals is used to quantify the degree of similarity between the reflectivity functions of two targets; the maximum value, one, being obtained for two identical range-profiles.

Let us consider a sampled signal, $s(n)$, composed by a complex-valued radar-signal defined for N values of the frequency-index, n. The range-profile, S, defined for R values of the range-index, r, is obtained by computing the DFT of s and squaring the magnitude of the result.

The value of the discrete cross-correlation between the real-valued vectors S and Y corresponding to the range-profiles of s and y is given by R_0 in 5.1.

$$R_0 = \frac{1}{R}.S * Y = \sum_{r=0}^{R-1} S(r).Y(r) \tag{5.1}$$

Due to the properties of the inner product, any variation of the conditions of measurement may affect the performance of the classifier. This is especially true when the target motion causes range-cell migration (RCM).

5.2.3 Target rotation

Let us consider an aircraft placed on a turntable facing a monostatic[1] radar. A rotation of the turntable by the angle $\Delta\theta$ causes a rotation of the target and simultaneously a variation of range of the scatterers. Two scatterers falling within the same range-bin could move in opposite direction when the table rotates. Beyond a given angle, these scatterers would migrate to different neighbouring range-bins. This effect is known as rotational range-cell migration (RRCM) [30]. The condition on $\Delta\theta$ to avoid RRCM is given by 5.2.

$$\Delta\theta < \frac{\Delta r}{D} \tag{5.2}$$

where Δr is the range resolution and D is the target dimension in m.

Let us consider a radar with a nominal range-resolution, $\Delta r = 2\ m$. The maximum rotation corresponding to a Rafale aircraft, whose length is $D = 15.3\ m$, is given by $\Delta\theta_{max} \simeq 0.13\ rad$. In this case, the classification would typically require templates measured for aspect-angles separated by no more than 5°. Considering the symmetrical structure of the target, 36 signatures would be required to achieve recognition of targets on a turntable.

[1] radar where the receiver at the same location as the transmitter

The conditions on $\Delta\theta$ have been experimentally examined by illuminating a model of a Rafale aircraft at scale 1:48 with a 3.2 GHz waveform at ENSIETA [38]. A library of range-profiles, Y_i, was formed with high-SNR measurements obtained at different aspect-angles, θ_i. A test-profile, S_{971} obtained by adding noise to the template obtained for $\theta_{971} = 5°$ is compared with the templates in library.

Figure 5.2 represents the correlogram, that is the set of coefficients of cross-correlation between this profile and the template range-profiles obtained at aspect-angles $\theta_{950} = -5°$ and $\theta_{1140} = 95°$. It shows that the maximum correlation is obtained with the template corresponding to the test-signal as expected. It also shows that the results of the cross-correlation obtained with measurements carried out at similar aspect-angles are close to one. The template-profiles present a high correlation with the test-profiles for indices between 955 and 975, that is for an angular interval, $\Delta\theta = 5°$ in line with expectation.

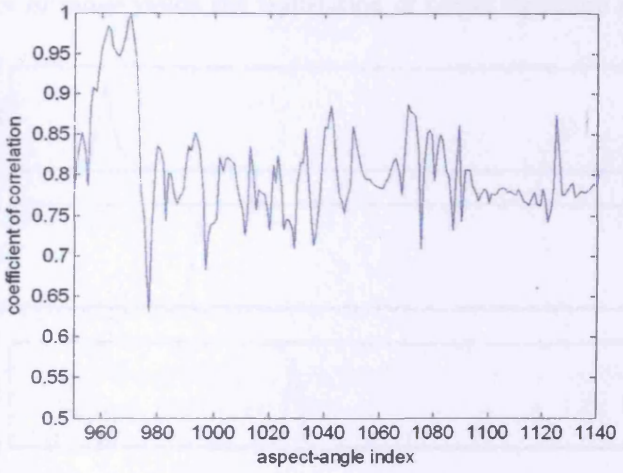

Figure 5.2: Correlogram - template profile $\theta_{971} = 5°$, test-profiles $\theta_{950} = -5°$ to $\theta_{1140} = 95°$, $\Delta\theta = 5°$ - scale-model Rafale

Although the variability of range-profiles with aspect-angle could be used for classification, it is seen as a drawback due to the cost of collecting and processing such a large library. This characteristic may be taken into account by introducing the index m for differentiating the range-profiles obtained at different aspect-angles. The modified expression of the cross-correlation function is given in 5.3.

$$R_m = \frac{1}{R} S * Y_m = \sum_{r=0}^{R-1} S(r).Y_m(r) \tag{5.3}$$

5.2.4 Target translation

Target classification is often achieved by comparing the reflectivity of different sections of the targets of interest. However, these signatures seen as the projections of the target reflectivity functions along the line of sight, are sensitive to target translation. High-resolution range-profiles, which provides a high level of detail, especially suffer from the so-called translational range-cell migration (TRCM). The latter occurs when the translation of a scatterer results in a shift of its reflectivity function in range by more than the nominal range-resolution.

The effect of TRCM is illustrated by the following example which involves a single corner-reflector illuminated by a 1 GHz-waveform at the experimental facility STATIC (CSIR) described in Chapter 2. Figure 5.3 represents five range-profiles obtained by Fourier transforming the complex-valued radar data measured for five different locations of the target: 1 m, 2 m, 3 m, 4 m and 5 m from a reference range. It shows that the translation of the target in range yields the translation of target signature in range.

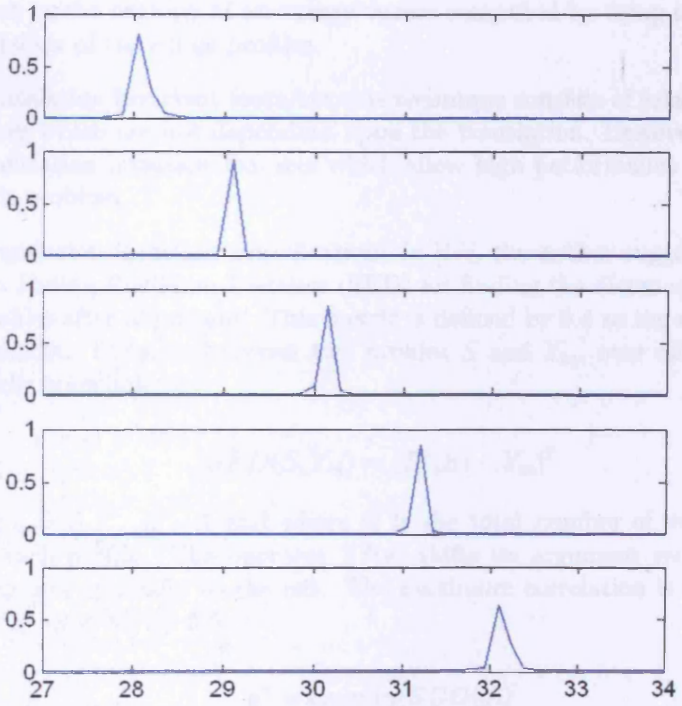

Figure 5.3: Range-profiles of a corner-reflector located at various ranges - the range-windows represented (27 m to 34 m) are aligned

Regarding classification, this example shows that different signatures of the same target may not be aligned despite being generated from mutually-coherent measurements. This occurs when the target-range changes between measurements. It obviously makes pointless the direct comparison of measurements of moving targets such as aircraft. In addition, a similar effect to TRCM affects range-profiles obtained with radar that are not mutually coherent. This happens when the reference-phase varies from one measurement to another.

Several methods exist for minimizing the effect of TRCM on the classification [30], [55].

- Relative alignment: it is common to achieve alignment by translating successive profiles with respect to the previous one. This technique, known as relative alignment, is efficient but has a severe drawback. If one profile is misaligned, the error propagates through the chain of profiles.
- Absolute-alignment: one technique consists of using absolute criteria such as the entropy of an energy vector computed by using translated versions of the range-profiles.
- Translation invariant features: this technique consists of selecting features which are not dependent upon the translation. However finding translation-invariant features which allow high performance is a difficult problem.
- Translation invariant classification: In [16], the author suggests using the Sliding Euclidian Distance (SED) for finding the distance between profiles after alignment. This metric is defined by 5.4 as the minimum Euclidian distance between two profiles S and Y_m, over all possible cyclic translations:

$$SED(S, Y_m) = |\mathcal{T}^q(S) - Y_m|^2 \tag{5.4}$$

for $q = 0, \ldots, Q-1$ and where Q is the total number of range bins in each profile. The operator $\mathcal{T}^q(\bullet)$ shifts its argument vector by q elements cyclically to the left. The maximum correlation is obtained for q^* as given by 5.5.

$$q^* = argmin(SED(q)) \tag{5.5}$$

5.3 Correlation-based classification

5.3.1 Signal-based approach

This section presents a basic translation-invariant classification technique for achieving alignment and comparison of range profiles using a correlation filter. The system diagram is represented in figure 5.4.

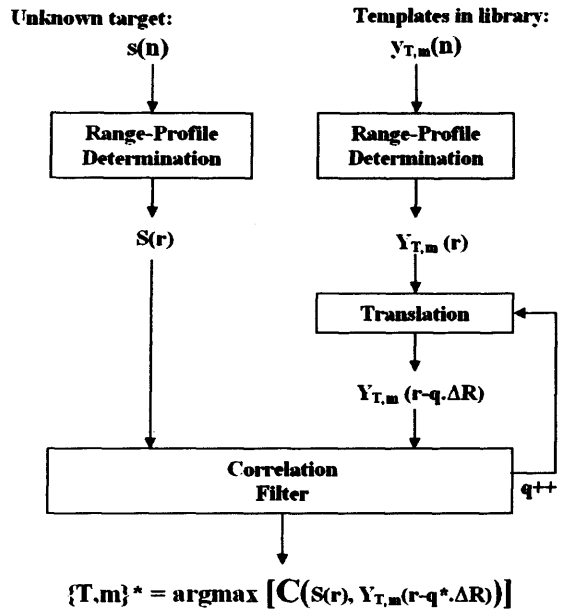

Figure 5.4: Structure of a correlation-based classifier using I/Q radar signals

The first stages compute the range-profiles, S and $Y_{T,m}$, of the test-signals s and the templates $y_{T,m}$. For each template, the subscript designates the target index and the aspect-angle index, respectively. The translation of the profiles is achieved by the operator $T^q(\bullet)$ which sequentially shifts the templates in the range. Then the computation of the circular cross-correlation function, $R(q)$, in 5.6, is achieved for each template.

$$R_m(q) = S * T^q(Y_{T,m}) \quad q = 0, 1, \ldots Q-1 \tag{5.6}$$

For a given profile, the maximum value of Q is bounded by the periodicity of $R(q)$ imposed by the periodicity of the operator that is needed to simulate phase wrapping. Alignment is achieved for the index q^* corresponding to the peak of $R(q)$. The peak-values, $C(T,m)$, obtained for various types of aircraft and various aspect-angles are then reported in an array. Once the profiles are aligned, classification is achieved by identifying the index of the template corresponding to the maximum value of $C(T,m)$.

5.3.2 Model-based approach

In this section, the radar signals, s and y, are replaced by their models, $\hat{s}$ and $\hat{y}$, in order to benefit from noise removal and resolution enhancement allowed by the super-resolution methods. First, the scattering-centre parameters of the signal in the library, $y_{T,m}$, are computed using the same parameters L and P for both. The corresponding models are reconstructed using the technique presented in the previous chapters. Here the bandwidth can be artificially enlarged by increasing the number of frequency indices used. Then the same process is applied to the measured signal. Finally, the profiles are aligned and compared by cross-correlation.

Figure 5.5 represents the system diagram of the model-based classification technique. It also relies on cross-correlation of test- profiles and template-profiles but uses high-resolution range profiles obtained by determining the scattering-centre models.

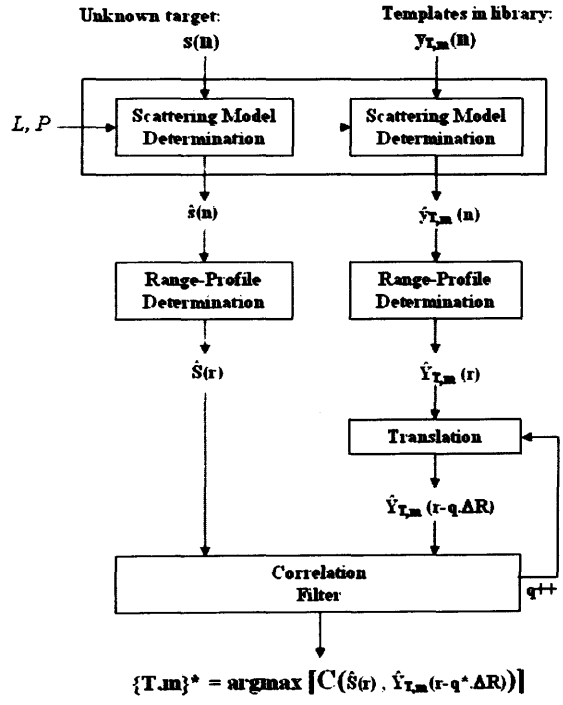

Figure 5.5: Structure of a classifier using scattering-centre models.

Depending on the accuracy of the model, the extrapolation of the original radar signals, s and $y_{T,m}$, is expected to create improved information that results in classification performance enhancement.

5.3.3 Example

Principle

In this example, a virtually noise-free profile has been cross-correlated with 1337 test-profiles obtained by illuminating seven targets under various aspect-angles. The indices are as follow: (1-191) correspond to target T_1, (192-382) correspond to target T_2, and so on. For each target, the indices are sorted by increasing aspect-angles where θ is increased from $-5°$ to $95°$.

The test-measurements are deliberately corrupted by an AWGN with $SNR = 20\ dB$. The template-profile chosen is again that of a scale-model Rafale aircraft (T6) at an aspect-angle $\theta = 5°$ The most similar conditions are those of measurements 970 and 972 obtained with the same target and at aspect-angles $\theta_{970} = 4.5°$ and $\theta_{972} = 5.5°$, respectively.

The template profile has been compared with the 1337 test-profiles. The following figures present the coefficients of correlation obtained using the two techniques presented earlier. The x-axis corresponds to the index of the test-profiles. The conditions of this experiment are fully detailed in the classification experiment.

Results

- Regular correlation

Figure 5.6 shows the coefficients of correlation between the various profiles mentioned above. The results are discussed below.

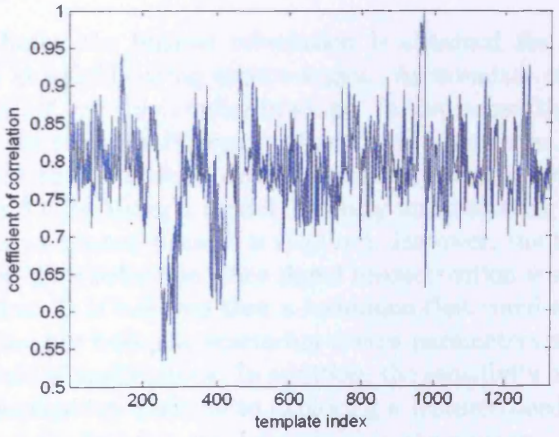

Figure 5.6: Correlogram - signal-based approach, $SNR = 20\ dB$

- Model-based correlation

Figure 5.7 represents the same graph but using the model-based approach described by the diagram 5.5. The complex-valued signals are replaced by their corresponding scattering-centre models constructed using the root-MUSIC algorithm and Linear Least Squares fitting. The parameters are $N = 64$ samples, matrix width $L = 23$, and model-order $P = 6$. It is assumed that the information contained in 6 poles is sufficient to discriminate between targets.

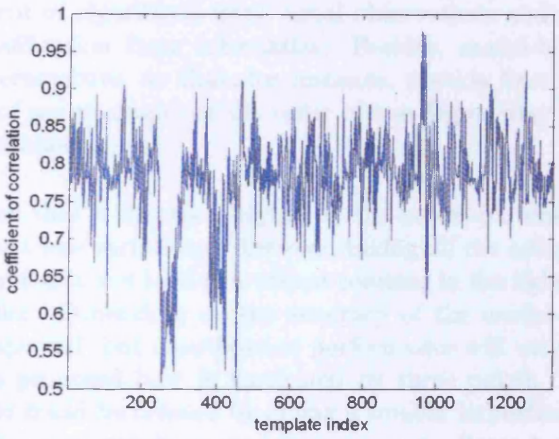

Figure 5.7: Correlogram - model-based approach, $SNR = 20\ dB$

Discussion

For both methods, the highest correlation is obtained for measurements of target (T6) at neighbouring aspect-angles. As a matter of fact, the two graphs, 5.6 and 5.7, are very similar in shape. In that sense, the model-based classifier may not perform differently than signal-based ones. Nevertheless, considering that this technique performs similarly with a scattering-centre model of order 6 only, using a model is clearly an interesting choice for applications where a limited dataset is required. However, the technique does not fully exploit data reduction since signal reconstruction is still needed before classification. It is believed that a technique that could achieve similar performance directly from the scattering-centre parameters would be more valuable in terms of applications. In addition, the sensitivity of the model to errors on its parameters leads us to exploring a feature-based classification technique where the features are determined in the z-plane.

5.4 Z-domain classification

5.4.1 Introduction

In this section, the principal results established previously are exploited for designing a feature-based classifier that uses the parameters of the scattering-centre model. The principal motivation for adopting a feature-based approach comes from the fact that model-based classifiers generally operate on large datasets which are not intuitively meaningful. On the contrary, exploiting features that are visibly related to the target structure makes easier the development of algorithms from visual observations and opens the way for target-classification from schematics. Besides, model-based classifiers are often hypersensitive, so that, for instance, speckle fluctuations caused by variations of aspect-angles of the order of one degree may be responsible for poor performance.

It is expected that a classifier relying on the model-parameters would be less sensitive to these variations. However, taking all the estimated parameters into account may not lead to a robust solution in the light of the results presented earlier. Depending on the accuracy of the model-estimates employed, it is expected that classification performance will vary considerably. The technique proposed here is motivated by three points. First, a more robust classifier could be created by giving a smaller importance to the contribution of the most sensitive model-parameters. Second, it is expected that using reduced but more accurate data provides enough information to achieve better classification. Third, the fact that the set of potential targets is limited intuitively calls for the introduction of *a priori* information in the modelling process.

Classification techniques rely on the idea that different measurements share common features if the subjects of measurements are similar. For radar-signals, such similarities exist when targets and aspect-angles are similar. As a matter of fact, they are actually exploited by correlation based-techniques. In this section, another type of technique is chosen. It consists of extracting from the signal the features that reveal the similarities between the targets compared. In particular, it is proposed to rely on information presented in the scattering-centre model. Mathematically, the scattering-centre model is a decomposition of the signal at the receiver into a sum of complex exponentials. Physically, it derives from the high-frequency approximation which stipulates that the radar signal back-scatterered by a target can be approximated as a coherent sum of scaled and delayed versions of the transmitted signal. The fact that complex exponentials can be related to an individual scatterer is exploited for classification purposes.

Earlier in this thesis, it was shown that the modelling techniques depend upon parameters related to the radar, number of samples and bandwidth, to the target structure, mainly the number, the distribution, and the physical properties of the scatterers, and to external factors such as the noise. This dependence has reliance on the modelling performance which can be affected by the differences that exist between the theoretical problem and the actual one. In the first case, the signal is composed by the coherent sum of elementary signals from a limited number of non-interacting point-scatterers in additive white Gaussian noise. In the second case, the signal may be generated by interacting scatterers exhibiting complex scattering mechanisms, multipath-phenomenon and possible clutter.

The poor capability of the technique to accurately extrapolate the radar signal which has been observed with complex targets is apparently due to errors that propagate through the different stages of the modelling process. In the end, the estimated model typically suffers from significant errors that are accentuated by the ill-posed nature of the least-squares fitting stage. For this reason, it is preferred not to rely on the fitting technique for aircraft classification. That implies discarding the amplitude-coefficients as a source of information. This decision has a direct consequence on the design of a classifier since it also implies that the feature-vectors must contain a sufficient amount of information needed for the classification.

The classification technique introduced in this chapter is based on the idea that the poles of the model parameters are less sensitive to noise and small variation of aspect-angles than the reconstructed model. It reveals that radar-measurements involving similar targets and similar perspectives should present similarities that can be observed in the pattern of poles expressed in the z-plane. As this is a key requirement for classification, it is believed that a signal could be classified by comparing its pattern of poles with other pole template-patterns in library. Physically each measurement is classified based on the probability that the target shares a common arrangement of scatterers in range with other targets in library.

This section presents the principle of classification of targets based on the pattern of poles. It refers to the conventional stages including pre-processing, feature-selection, and classification. Several issues that are specific to this comparative approach are addressed in this chapter. They include the way to measure the similarity between patterns of poles, the features to use for the comparison, the differentiation between true poles and extraneous poles, whether the latter are due to the noise, to the technique, or even to extra-scatterers on the target. Finally, the problem of alignment, which is common to most classifiers is taken into account.

5.4.2 Principle

In order to present the principle of this classifier, let us start by considering two true poles, z_k and z'_m on the test-pattern and the template-pattern, respectively. Assuming that the patterns are aligned, the pole-angles correspond to the same absolute time-delay. One can thus estimate that these poles are associated with two scatterers that induce the same time-delay if the interpole-distance, $d(z_k; z'_m)$ is null.

By extension, if two patterns of K true poles can be perfectly overlaid, one may consider that K scatterers of the test target induce the same time-delays as K scatterers of the template target. Classification consists of associating the measurements that reveal at least K scatterers which induce the same time-delays. Statistically, the probability that two patterns of K true poles be perfectly overlaid in a representative library decreases when K increases. By setting a value of K large enough, it is possible to create some classes of template-measurements populated by a single element only. Recognition could thus be achieved by applying such a classifier to the test-pattern with the correct value for K.

Considering that the poles chosen are directly related to the location of the scatterers, one can consider that the classification technique proposed is strongly based on the spatial arrangement of the scatterers on the target. In other words, the technique relies on the assumption that similar arrangements of the scatterers on the targets yield similar arrangements of the true poles in the z-plane. For two successive measurements of the same target, it is expected that some elements of the pole patterns coincide. However, perfect superposition of the scatterers is not likely to occur in practice:

- the values of the estimated poles, z_k and z'_m, vary from their expected values because of the noise. For additive white Gaussian noise, the probability that two given poles have the same expected value, $< z_k > = < z'_m >$, increases with the proximity of the poles.
- the variation of the scene between the two compared measurements can cause two poles associated with the same physical scatterer have slightly different expected values as, for instance, the template-target used to build the class is not exactly identical to the test-target.
- small variations of aspect-angle may be responsible for speckle fluctuations which have direct effects on the pole estimation.

- large variations of aspect-angle may change the radar-cross-section of the target. Depending on the target, it may affect the position and even the presence of a pole. This phenomenon is emphasized with scatterers that have complex geometries and that are not independent.
- limited bandwidth and limited number of samples cause inter-dependence between poles. As a result, presence of clutter, for instance, may cause small variations on the other pole-estimates.
- incorrect calibration of the initial phase creates a constant shift between the pole-angle estimates and their expected values. For the test-pattern and the template-pattern, the shifts can be different.

This list reveals that the design of the "optimal classifier" from statistical information may require knowledge of a high number of parameters related to the target structure and motion as well as external factors such as statistical properties of the noise. Instead, it is preferred to draw the lines of a relatively simple prototype classifier, whose design could be empirically improved.

The technique proposed for classifying targets is a matching algorithm using a clustering approach in the z-plane (MAUCAZ). Signals are classified by comparing their patterns of poles with templates in a library. A limited number of clusters are formed by associating two poles, one from the test-pattern and the other from the template-pattern, supposedly related to the same physical scatterer on the target. The similarities between two patterns are quantified by means of a mathematical expression that increases with the distance between corresponding poles. This method enables the classifier to take into account the variations of the poles mentioned above. This cost-function is calculated for each pattern in the library, that is, for measurements involving various types of aircraft and various aspect-angles. Assuming that the minimal distance corresponds to the maximum similarly, it is expected that the best match corresponds to the minimum value of the cost function.

5.4.3 Pre-processing

Introduction

Z-plane classification is achieved by comparing radar-signals based on features that are visible in the pattern of poles in the z-plane; the latter being related to the scattering function. In the pre-processing stage, data are prepared for feature-selection. Figure 5.8 represents the system diagram leading to the determination and selection of the poles using both the test-signal and the templates in library.

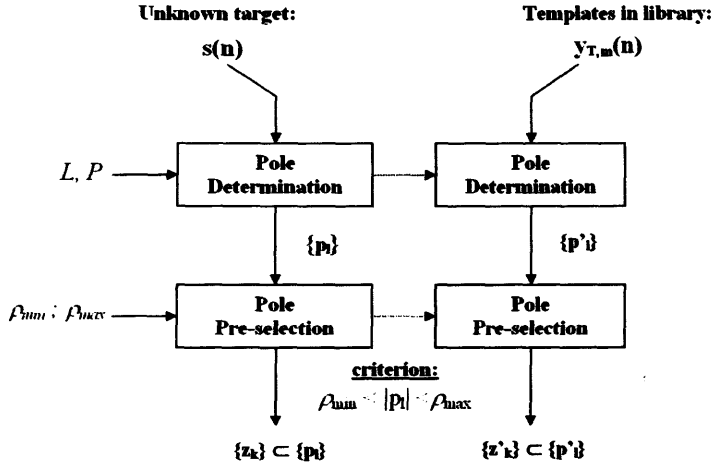

Figure 5.8: MAUCAZ system diagram - pre-processing stage

Pole determination

The first stage consists of computing the patterns of poles, $\{p\}$ and $\{p'\}$, for the test-signals and for the signals in library, respectively. This can be done by using super-resolution techniques such as root-MUSIC or Matrix Pencil algorithms. This operation requires the setting of the size of the observation-window, L, and the model-order, P. Information on this subject can be found in Chapter 3.

The number of poles computed, $L-1$, is directly related to the size of the observation-matrix. One generally considers that the poles determined by these methods can be divided into "true poles" related to physical scatterers, and "extraneous poles" created by the mathematical technique employed and considered as artefacts.

Pole pre-selection

Although the whole pattern of poles represents a source of information, it is chosen to focus on the poles that correspond to physical scatterers. The first reason comes from the fact that these poles contain the information that can be directly related to the target property. The second reason is that they vary with the technique employed. The third reason is that they are smaller in number, which can be an issue for real-time processing. It is believed that by taking enough poles into account, their values can provide sufficient information to distinguish between the limited number of potential targets. The principal task of feature selection is to identify the poles that are relevant for classification. It consists of separating the elements, called true poles, which are related to physical scatterers, from the other elements considered as artefacts.

For a target composed by P scatterers, removing the extraneous poles is conventionally achieved by keeping the P poles that are the closest to the unit-circle. In this case, all the filtered patterns would have the same number of poles. However, it has been shown in the previous chapter that true poles tend to move outwards for low SNR so that some extraneous poles may appear as better candidates for pole selection.

Instead of using a single criterion based on the pole magnitude, it is suggested that the selection be made using *a priori* information. At this stage, the poles are only pre-filtered using the criterion proposed by Carriere and Moses and reported in 3.66. This operation is achieved by keeping all the poles whose magnitude lies within fixed boundaries, ρ_{min} and ρ_{max} defined in 5.7.

$$\rho_{min} < |p_l| < \rho_{max} \tag{5.7}$$

One approach for fixing the boundaries consists of using the indicative values suggested by in 3.66. It is also desired that the number of poles remaining, M, be greater than the number of poles considered for classification, K. Another approach consists of setting the limits, ρ_{min} and ρ_{max}, so that no filtered pattern contains less than M poles. The value of K is discussed later in this chapter.

These boundaries define a selective filter whose transfer function can be represented as a ring in the z-plane. Figure 5.9 shows the principle of pole pre-selection. The figure on the left-hand side represents the $L-1$ poles in the z-plane. The poles selected by the filter belong to the area represented in blue. The figure on the right-hand side represents the resulting pattern of poles as it appears in the feature-selection stage.

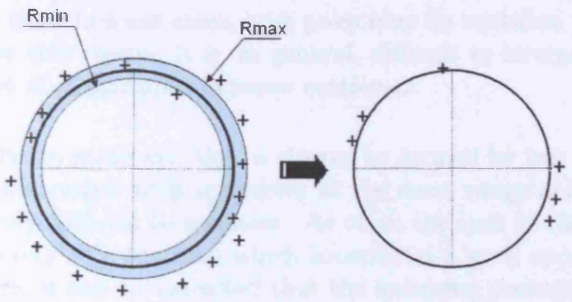

Figure 5.9: Concept of pole pre-selection

5.4.4 Feature extraction

Pole Similarity

Let us designate by the term cluster, an association of two poles, $z_k = \rho_k.e^{i.\theta_k}$ from the test-pattern and $z'_m = \rho'_m.e^{i.\theta'_m}$ from a template-pattern. The proposed classifier relies on the assumption that true poles and scatterers are related in such a way that the closer the poles, the greater the probability that they are associated with two scatterers inducing the same time-delay, or for the simplest case, with scatterers at the same range.

For simplicity, let us address the case of poles lying on the unit-circle first. The problem is thus limited to one dimension, only. For two aligned patterns, the probability, $p(\Theta)$, that two poles are related to scatterers at the same range is an even function of the difference between angles, $\Theta = \theta'_m - \theta_k$. It has a maximum for $\Theta = 0$, a minimum for $\Theta = \pm\pi$, and, for a given value of Θ, it increases with the variance of the noise. Therefore when samples are added, the signal-to-noise ratio increases and the variance of the poles estimates decreases. It results that for a given value of Θ, the probability, $p(\Theta)$, increases with the nominal range-resolution.

Let us now introduce a second dimension by considering the pole magnitude. Let us recall that the latter is related to the spatial distribution of the scatterer, that is to the spread of energy in range, which depends upon the geometry of the scatterers. It can be assumed that the probability, $p(\Delta\rho)$, that two poles are related to scatterers with geometries leading to similar damping factors is an even function of the difference between their magnitudes, $\Delta\rho = \rho'_m - \rho_k$ with a maximum for $\Delta\rho = 0$. Therefore, providing this parameter is accurately estimated, it could be used for classification. However, it is now known that the pole magnitude can vary in large proportion when the signal-to-noise decreases. As a matter of fact, the variation can be

so significant that, in some cases, true poles may be mistaken with extraneous poles. For this reason, it is, in general, difficult to interpret physically the differences of magnitudes between scatterers.

The probability, $p(\Delta\rho, \Theta)$, that a cluster be formed by two poles, z_k and z'_m, that are associated with scatterers at the same range and same geometry is relatively difficult to estimate. As often the case in classification, it is common to rely on a function which constitutes a good approximation of $p(\Delta\rho, \Theta)$. Here, it can be expected that the unknown probability function, $p(\Delta\rho, \Theta)$, depends upon the difference between their angles and their magnitudes, Θ and $\Delta\rho$. Assuming the variation of pole-angle and the variation of magnitude are independent, $p(\Delta\rho, \Theta)$ can therefore be modelled by a function of $\Delta\rho$ and Θ describing a three-dimensional surface with a maximum value and an axial symmetry at (0,0).

As an example, an elliptical Gaussian function has been used to represent $p(\Delta\rho, \Theta)$ in 5.10.

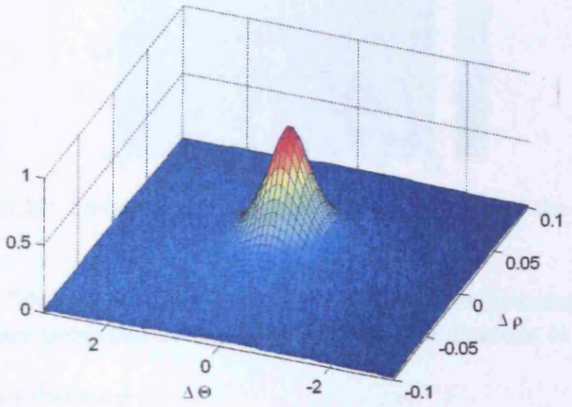

Figure 5.10: Bi-variate Gaussian function used for $p(\Delta\rho, \Theta)$

Assuming the probability function has an axial symmetry, one can transform the two-dimensional probability function, $p(\Delta\rho, \Theta)$, into a function of one variable, d. In other words, the function computed is defined as a function of d, which has, on the one hand, a common value for the locus of equi-probable poles and, on the other hand, different value for the loci of points having different probabilities. Due to the properties of the probability function, the transformed function is a monotonic function. For an elliptical Gaussian function, this function is a Gaussian and the variable is directly obtained from the equation of the ellipse. It is given in 5.8

- Elliptic distance:

$$d_e(z_k; z'_m) = \sqrt{\left(a.\Delta\rho\right)^2 + \left(\Theta\right)^2} \tag{5.8}$$

Figure 5.11 represents the values of d as a function of $z_k = x_k + i.y_k$ for $z'm = 1$ and $a = 1$. For each point of the Argand diagram, the colour of the pixel indicates the distance between the corresponding pole, z_k, and the pole $z'_m = 1$. Considering that $p(k, m)$ decreases with d, figures 5.11 shows that there is a small probability that two poles located in two different half-planes can be associated with two scatterers at the same range. For reducing the computation time, the number of clusters to consider can be reduced by half at least.

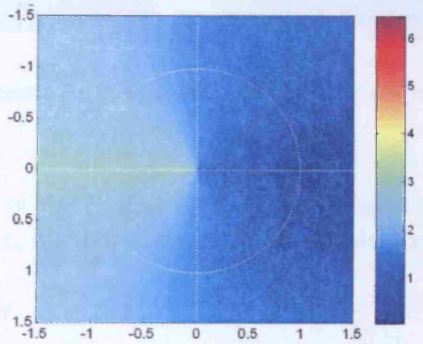

Figure 5.11: Distance: $d_e(z, 1)$ as a function of z in the z-plane

The term "distance" often refers to a different expression. Expressions 5.9 and 5.10 are proposed as an alternative to the distance in 5.8.

- Euclidian distance:

$$d_E(z_k; z'_m) = \sqrt{\rho_k^2 + \rho_m'^2 - 2\rho_k\rho'_m cos\Theta} \tag{5.9}$$

- Z-plane distance:

$$d_z(z_k; z'_m) = \left| \frac{1}{2K} \left[u + \frac{sinh(2u)}{2} \right]_{u_k}^{u'_m} \right| \tag{5.10}$$

where $u_k = asinh(K.\rho_k)$, $u'_m = asinh(K.\rho'_m)$ and $K = \Theta/\Delta\rho$.

Figure 5.12 is a representation similar to 5.11 using the expression of the distance in the Euclidian plane, d_E, in 5.9 (left) and the expression of the distance in the z-plane plane, d_z, as proposed in 5.10 (right).

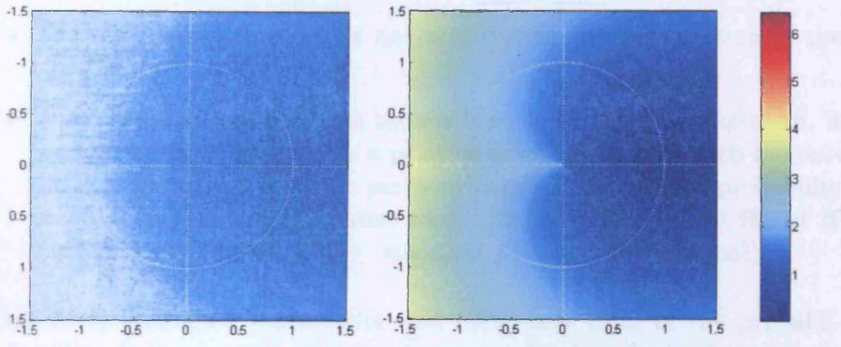

Figure 5.12: Distances: $d_E(z,1)$ (left) and $d_z(z,1)$ (right) as a function of z in the z-plane

The comparison of the figures 5.11 and 5.12 shows that the expressions of the distance in 5.8, 5.9 and 5.10 are locally equivalent.

Pattern Similarity

The previous section addresses the problem of estimating the probability, $p(\Delta\rho, \Theta)$, that one cluster be formed by two poles, z_k and z'_m, that are associated with scatterers at the same range and having similar geometry-based scattering behaviours. In order to quantify the similarity between patterns, it is proposed to consider this probability in the case of several clusters. In the following, it is considered that a given set of K clusters has been formed using the poles from the test-pattern and from the template-pattern. Because poles and scatterers are associated in a one-to-one relationship (bijection), the same pole cannot be used in two different clusters.

The function chosen to quantify the similarities between a test-pattern and a template-pattern arises from considering the case of two measurements carried out on the same target and at similar aspect-angles. Assuming that the K clusters of true poles corresponding to scatterers with similar properties could be identified, several observations can be made:

- The probability, $p(K)$, that K poles of the test-pattern and K poles of the template-pattern forming K clusters, describe the same K scatterers depends upon the probability, $p(k,m)$, that the poles of each cluster are related to scatterers with similar properties. The probability, $p(K)$, is thus a function of the K inter-pole distances, d, as

represented in 5.11

$$p(K) = p(d_1, d_2, \ldots, d_K) \tag{5.11}$$

where d_k, is the inter-pole distance of the k^{th} cluster.

- The probability function is not sensitive to the permutation of the clusters.
- When the scatterers of both targets have an identical arrangement, it is expected that there exists a position of alignment for which the patterns of true poles could be perfectly overlaid. Hence, the probability function, $p(K)$, is a maximum when the probability, $p(\Delta\rho, \Theta)$, of K clusters are all maximal (*i.e.* when the distances are minimal).

Due to the assumed symmetries and monotonic form of the probability function, it is expected that the latter can be described using a single variable, D, in such way that the probability function increases when D decreases. For pattern recognition, it is common to use such variables as a measure of the dissimilarity between groups of numerical variables.

Various expressions can be used to evaluate the degree of similarity between two sets of K poles [51]. They include 5.12, 5.13 and 5.14.

- City-block distance

$$d_{CB} = \sum_{i=1}^{P} |d_i| \tag{5.12}$$

- Euclidian distance:

$$d_{Eu} = \left(\sum_{i=1}^{P} d_i^2 \right)^{1/2} \tag{5.13}$$

- Chebyshev distance:

$$d_{Ch} = max\Big(|d_i|\Big) \tag{5.14}$$

where d_i is the inter-pole distance corresponding to a cluster C_i.

City-block and Euclidian distances are also known as the Minkowski distances of the first and second order, respectively. City-block distance is directly related to the mean value, so that it is a linear expression of the inter-pole distances. In the contrary, the Euclidian distance, whose contours of equal value define hypersheres, gives greater emphasis to larger values of the inter-pole distances. Chebyshev distance is entirely defined by the largest value of the inter-pole distances. This expression does not enable differentiation of sets that have the same maximum value. However, it can be used as an approximation for decreasing the processing time.

5.4.5 MAUCAZ

Principle

The classifier is based on the principle that two targets sharing similar arrangements of scatterers also share similar arrangements of the poles in the z-plane. Classification can thus be described as gathering the template-patterns whose K poles have a high probability, $P(K) \gg P_K$, to correspond to K scatterers related to K poles of the test-pattern. Identification is achieved when a class is populated by one template only.

It appears that the arrangement of poles into clusters is an important aspect of the classification. However, for a given template, there is *a priori* no robust rule stating what are the couples of poles that should be combined to form clusters.

Assuming that there exists in the library a measurement carried out on the same type of target and at similar aspect-angle as the test-measurement, it is expected that most true poles of the test-pattern coincide with the true poles of the template-pattern since they are associated with the same scatterers. The problem of recognition consists of finding, in each pattern, the arrangement of K pairs of poles that "match" each other.

The first stage consists of computing the inter-pole distance for all possible clusters, $C_{k,m}$, whose poles, z_k and z'_m, are obtained from the test-pattern and from the template-pattern, respectively. Figure 5.13 represents the array containing the interpole distance, $D(k,m)$, obtained using one of the expressions proposed. Each row corresponds to a pole, z_k, in the test-pattern and each column to a pole, z'_m, in a template-pattern

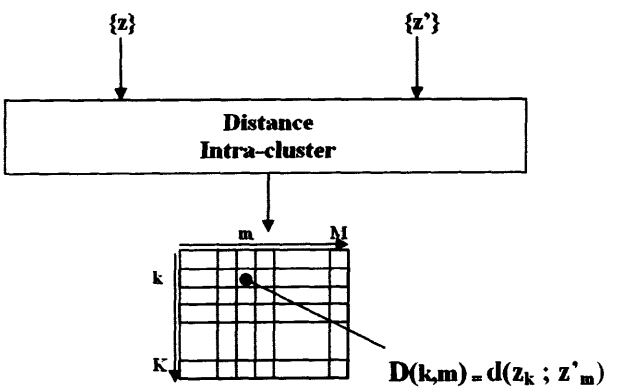

Figure 5.13: MAUCAZ: computation of the inter-pole distances

The second stage involves comparing the levels of similarity between the test-pattern and the templates patterns in library. The 'best-matching pattern' is not found by computing the probability itself but using the expressions of the distance between patterns proposed. The minimum distance is expected to occur when the selected clusters are formed by poles that correspond to the same scatterer as it is the most likely solution.

Since the corresponding poles cannot be easily identified, it is proposed to consider all the possible combinations of poles that can be used to create K clusters. For each, it is proposed to find the arrangement of K clusters that has the highest probability that the K clusters be formed by poles associated with scatterers at the same range and with geometries leading to the same energy spread in the range.

Cluster Selection

For two patterns of M and M' poles, the total number of different clusters is $M.M'$. For two patterns of M true poles, the number of possible unsorted arrangements of M clusters is $M!$ but more likely, the number of arrangements that make physical sense is smaller. For example, it can decrease if:

1. the patterns contain spurious poles that were not rejected by the filter
2. the patterns contain true poles that do not appear on both due to small variations of the conditions of measurements

The total number of possible unsorted combinations of K clusters is given by $N_{comb}(K)$ in 5.15

$$N_{comb}(K) = \frac{1}{K!}\frac{M!M'!}{(M-K)!(M'-K)!} \tag{5.15}$$

where $(K < M)$ and $(K < M')$.

For reducing the computation time, a number of combinations can be discarded based on the fact that some combinations of poles and some combinations of clusters are not likely to correspond to physical situations. For instance, poles that are located in different half-planes are not likely to correspond to the same scatterer. Mathematically, this can be regarded as the rejection of the clusters which by themselves would increase the distance between patterns beyond any typically acceptable limits. Similarly, since the target is assumed to be rigid, poles ordered by increasing angles are not likely to correspond to poles that are not.

Figure 5.14 illustrates the clustering approach using a combination of three pairs of poles obtained for $M = 5$ and $M' = 6$. The poles are represented by different markers: $(\times)$ for the test-pattern and $(+)$ for the template-pattern. This combination of three dipoles is only 1 out of the 1200 that the 30 possible clusters authorize.

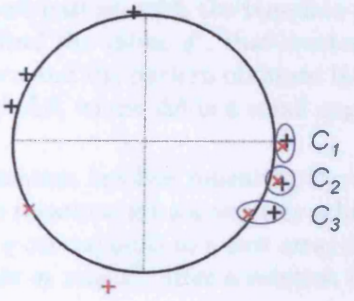

Figure 5.14: Concept of pole clustering for $K = 3$, $M = 5$ and $M' = 6$

Number of clusters

The number of clusters to take into account is an important issue. The minimum value of K should allow classification whereas the maximum value should be such that the selected clusters include no more poles than the true poles associated to the scatterers that appear on both patterns. For real systems, the optimum value may be driven by issues related to the computing-time required for the analysis.

In order to reduce the computation time, it is possible to decrease the number of combinations of clusters studied by decreasing K. However, decreasing K yields an augmentation of the population of the classes. In other words, target recognition requires K to be set at a high enough value in order to obtain a class populated by a single element.

Considering the case of scatterers occupying the spatial extent corresponding to a range bin, the total number, $N_{arr}(K)$, of different unsorted spatial arrangements of K scatterers in N range bins is given by 5.16.

$$N_{arr}(K) = \frac{N!}{K!(N-K)!} \tag{5.16}$$

The best matching pattern is found by computing the distance between patterns for a potentially large number of arrangements indeed. It is suggested that several values of K should be tested and compared in order to achieve recognition.

Pattern alignment

The problem of translational range-cell migration (TRCM) that characterises range-profiles exists in the z-plane too. Whereas translation of the target in range appears as a translation of the envelope of the range-profile, it is manifested by a rotation of the poles in the z-plane. In order to achieve the alignment of the test-pattern with the template-pattern, it is proposed, for each template, to find the value, q^*, that creates the highest similarity between the test-pattern and the pattern obtained by rotating the template-pattern by the angle $q^*.\Delta\theta$, where $\Delta\theta$ is a small angular-step.

Basically, the modification involves repeating the clustering process after each rotation. Here the rotations are successively achieved by iteration of the index q. Each value of q corresponds to a new array containing the distance, $D_q(k,m)$, between poles z_k and z'_m after a rotation of the template-pattern by $q.\Delta\theta$.

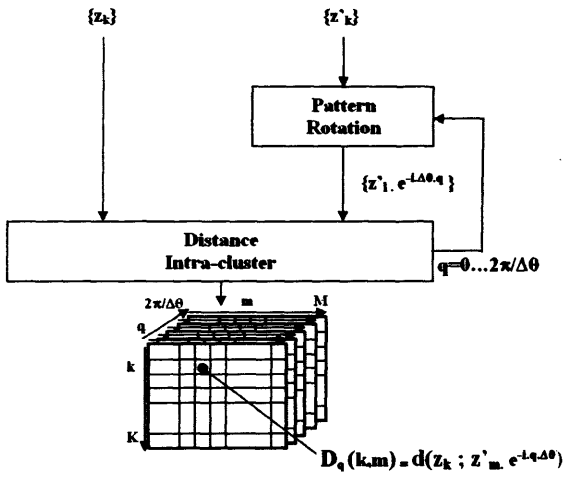

Figure 5.15: System diagram - alignment 1/2

For each array containing the inter-pole distances, $D_q(k,m)$, one computes a single value $C_{alignment}$, which is a measure of the similarity between the test-pattern and the template-pattern after rotation by the angle $q.\Delta\theta$.

The values of $C_{alignment}(q)$ depend upon the number of clusters, K, that are taken into account. This is due to the fact that the distance between subsets of $\{z\}$ and $\{z'\}$ varies with the dimensions of the subsets. At this stage, the choice of K remains an issue. For this reason, it is suggested to compute the values $C_{alignment}(q)$ for various values of K. Because the cost-function depends upon the number of patterns and the number of clusters

taken into account, the number of arrays to conserve is equal to the product of the number templates by the number of values that K can take.

Alignment of the closest template-pattern is achieved by rotating the template-patterns by the value $q^*.\Delta\theta$ where q^* is the value that minimises the cost-function, $C_{alignment}(q, K)$. Once the value q^* is estimated, one can discard all the array of distances, $d_q(k, m)$, but those corresponding to the rotation-index q^*. Fine alignment requires small rotation-steps, $\Delta\theta$, which increases the maximum value of q needed.

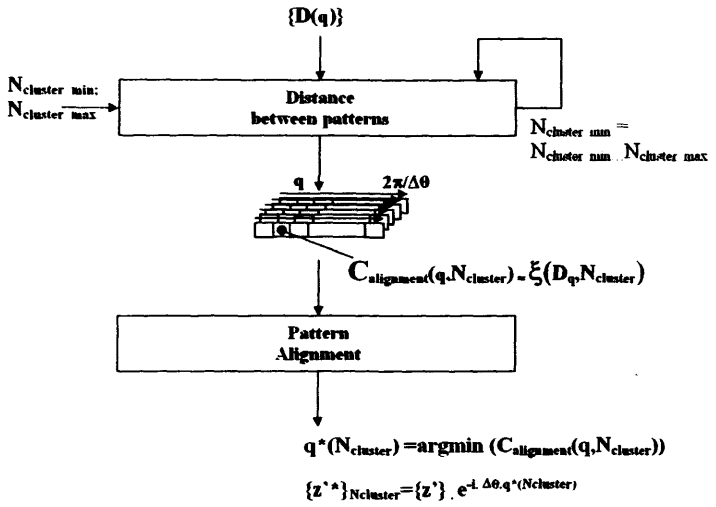

Figure 5.16: System diagram - alignment 2/2

The cost-function gives a physically meaningful result if each cluster selected is formed by a pair of true poles that can be associated with the same scatterer. However, true poles can be divided into three categories:

1. true poles that exist in the template-pattern only,
2. true poles that exist in the test-pattern only, and
3. true poles that exist in both the template-pattern and the test-pattern.

Unfortunately, the poles of the third category are unknown and so is the number of clusters that must be considered for alignment, K. For this reason, setting a value to K remains an issue, which is investigated in the following example.

5.4.6 Example

Principle

A measurement of the scale-model Rafale aircraft (T6) at aspect-angle $\theta = 45°$ is compared with the measurements of the same target for aspect-angles $\theta = -5°, 4.5°, \ldots, 95°$. The test-measurements represented by index 1 to 201 are corrupted by an AWGN with $SNR = 30\ dB$. The comparison is achieved using the distance between patterns obtained with the MAUCAZ algorithm whose the system diagram is represented in figure 5.17

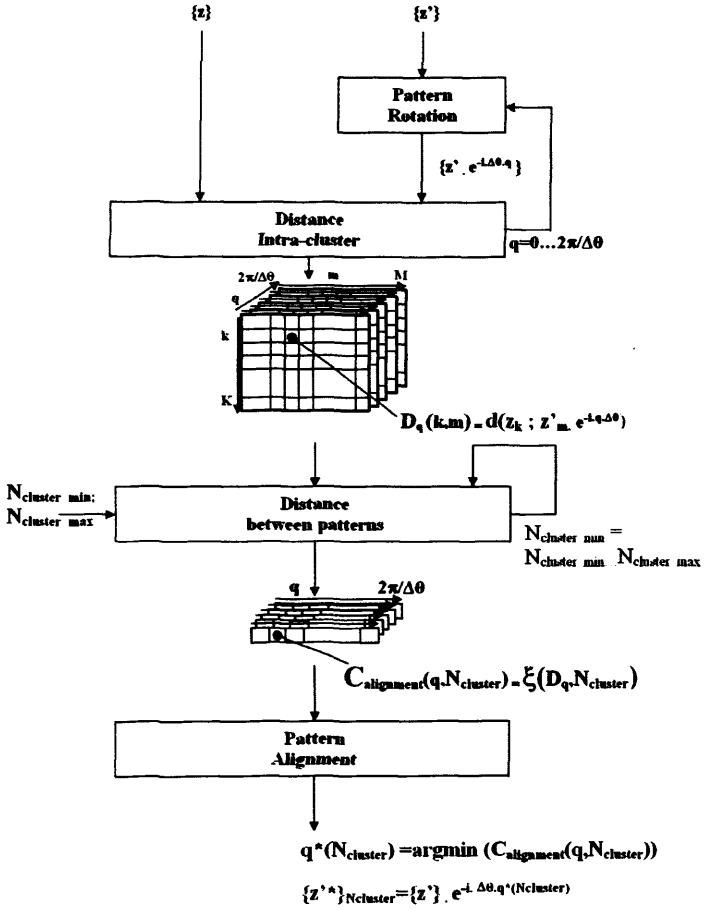

Figure 5.17: System diagram - alignment

In this example, the function chosen for the inter-pole distance is the Euclidian distance, d_E. The function chosen to compute the distance between patterns is the City-Block distance, d_{CB}, with $K = 4$. The parameters used to compute the patterns are $M = 6$, $P = 5$, $L = 23$.

Distogram

The first example illustrates the variations of the distance when the aspect-angle varies. By analogy with a correlogram, let us call the graph representing the distance between patterns, a distogram. Figure 5.18 represents the distogram of a template-pattern and 201 test-patterns aligned by MAUCAZ. The x-axis corresponds to the index of the test-profiles. The y-axis represents the distance between the test-patterns and a given template-pattern. As small values are synonymous to high similarity, the y-axis is limited to 0.1 for convenience of the display. The maximum similarities are found for pattern-index 101 and 116, which correspond to aspect-angles 45.5° and 53°.

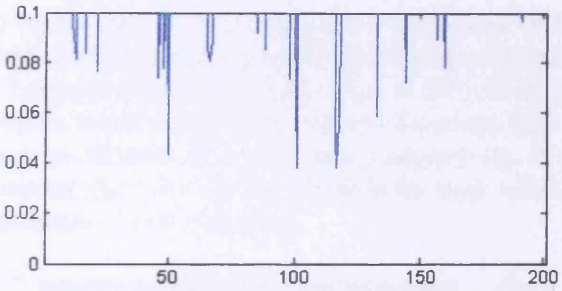

Figure 5.18: Distogram - $SNR = 30\ dB$, index 100 (Rafale aircraft - 45°) - x-axis: $T_6 \times (-5°, \ldots, 95°)$

The second example illustrates the variations of the distance when both the aspect-angle and the target vary. Here, seven targets are involved, yielding 1407 measurements. Figure 5.19 represents the distogram where the index (1-201) corresponds to target T_1 at aspect-angles $\theta = -5°, 4.5°, \ldots, 95°$, (202-402) correspond to target T_2 at the same aspect-angle, and so on. Many patterns of targets T_6 and T_7 are similar to the pattern used (1106).

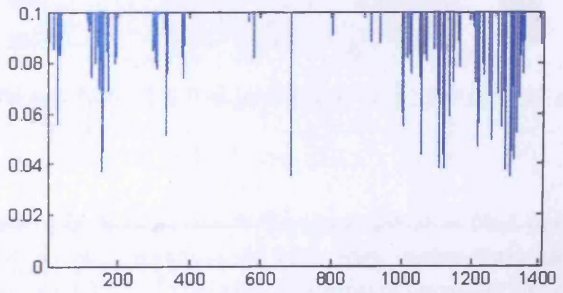

Figure 5.19: Distogram - $SNR = 30\ dB$, index 1106 (Rafale aircraft - 45°) - x-axis: $(T_1, \ldots, T_7) \times (-5°, \ldots, 95°)$

Two-dimensional distogram

For training a classifier with a given dataset, it can be useful to compute the distances between the measurements and their noisy versions. The results can be stored in a square matrix that can be displayed as a two-dimensional image where each line represents a distogram as mentioned above.

This example uses the set of 201 measurements obtained by illuminating the scale-model Rafale aircraft under 201 different aspect-angles $\theta = -5°, 4.5°, \ldots, 95°$.

Figure 5.20 represents the two-dimensional distogram of these 201 measurements. Both axes represent the index of the measurements by increasing aspect-angles bounded by $\theta_1 = -5°$ and $\theta_{201} = 95°$. Each pixel spans the distance between a template-pattern and a test-pattern that can be identified by the pixel coordinates, in x and y axis, respectively. A scale of colours is used to represent the value of the distance for each pixel. Dark colours are used for indicating small distances.

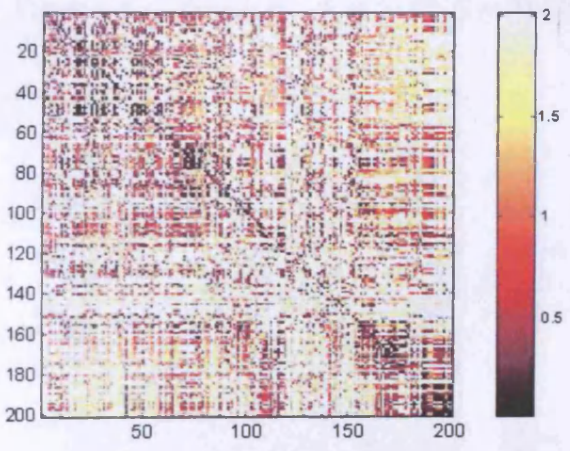

Figure 5.20: Cost matrix for $P = 4$, $SNR = 30\ dB$

On this image, the dark pixels of the diagonal show that patterns obtained from the radar measurements and from their noisy-versions are relatively similar. The small width of the dark diagonal is cause by the high variability with aspect-angle. Ideally the diagonal should be large in order to limit the volume of the library, and the dark pixels should be limited to the measurements of a single target, in order to avoid incorrect classification.

The following illustrates the effect of increasing the value of K on the distogram. For this experiment, the set of seven targets mentioned earlier and described in figure 5.24 is used to create a 1407x1407 distogram.

Figure 5.21 represents the distograms for K=2.

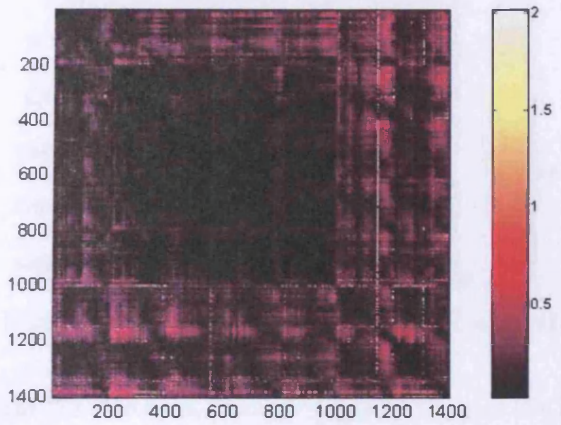

Figure 5.21: Distogram - $K = 2$, $SNR = 30\ dB$

Figure 5.22 represents the distograms for $K = 3$.

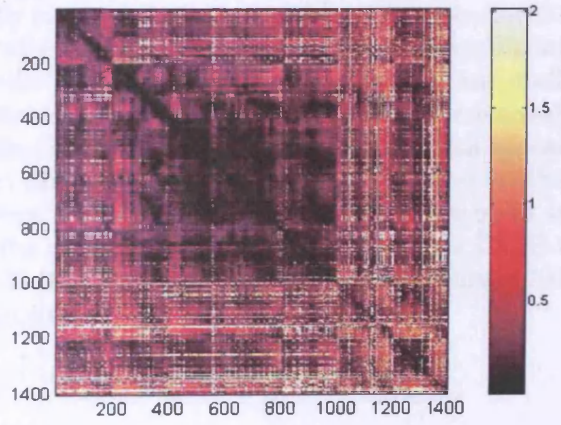

Figure 5.22: Distogram - $K = 3$, $SNR = 30\ dB$

Figure 5.23 represents the distograms for $K = 4$.

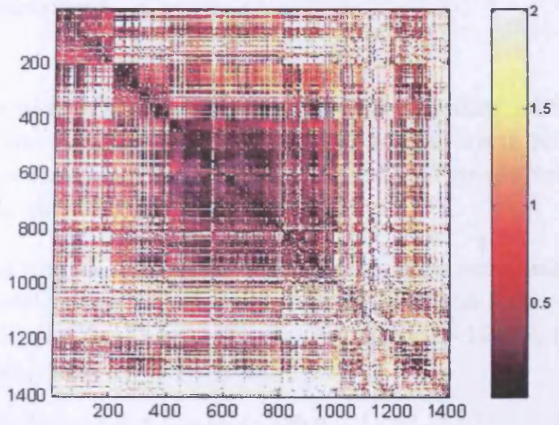

Figure 5.23: Distogram - $K = 4$, $SNR = 30\ dB$

Although the 2D-distograms are averaged because of the resolution, the principal features can be observed in these figures. For $K = 2$, the dark diagonal cannot be obviously noticed as there exist many combinations of clusters that can generate an arrangement of two poles that is similar to those in the test-patterns. As the number of satisfying combinations decreases with the number of poles taken into account, the distance between patterns greatly increases with K. This basic principle described by equation 5.16 explains why the two-dimensional distogram becomes brighter when K increases. As the distance between a given pattern and itself remains null, or at least relatively small, the diagonal becomes increasingly visible. For $K = 4$, this effect is emphasized and the dark diagonal appears clearly. The dark square in the area bounded by indices 400 and 900 implies that the distance between the pole-patterns of these mesurements are similar. In other words, the information extracted from targets $T3$ (F-14 scale-model aircraft), $T4$ (F-16 scale-model aircraft) and $T5$ (Mirage 2000 scale-model aircraft) are similar.

5.5 Classification performance

5.5.1 Experiment

Principle

The classification framework chosen consists of finding a library template whose profile has maximum similarity with an unknown test-profile. The dataset used for the experiment is composed by 1407 measurements collected at the anechoic chamber of ENSIETA.

- the set of targets, represented in figure 5.24 is composed by seven 1:48 scale-model aircraft that are coated with a conductive paint. They include T_1 (DC3), T_2 (F-117), T_3 (F-14), T_4 (F-16), T_5 (Mirage 2000), T_6 (Rafale), and T_7 (Tornado).
- the 201 aspect-angles available are $\theta \in \{-5°, -4.5°, \ldots, 95°\}$; the position $\theta = 0°$ corresponding to the aircraft nose facing the radar antenna.

Radar measurements are obtained by illuminating the targets with a 3.2 GHz stepped-frequency waveform formed by 64 ultra-narrow band pulses whose carrier-frequency is successively shifted by 50 MHz steps. The polarisation is HH. The 1407 measurements have been ordered by increasing target-index and by increasing aspect-angle, the first 201 measurements corresponding to target T_1

Ten measurements per target have been extracted from the dataset at regular aspect-angles, θ_L, given by 5.17

$$\theta_L = \{-5°, 5°, 15°, 25°, 35°, 45°, 55°, 65°, 75°, 85°, 95°\} \tag{5.17}$$

The resulting set of 70 measurements serves as a library for the classification. The remaining 1337 measurements are used as test-measurements after a White Gaussian noise had been added. For statistical analysis, each of the 1337 test-profiles is individually cross-correlated with the 70 template-profiles.

For each test-profile, the class attributed is the class $C \in \{C_{T1}, C_{T2}, \ldots, C_{T7}\}$ of the target corresponding to the template-profile that has the maximum correlation with the test-profile.

The classification is said to be forced. When the estimated class is the class of the target, the recognition is correct, otherwise it is not. By repeating the classification for all the 1337 test-targets, it is possible to assess the performance of the classifier by computing the rate of correct classification.

Prediction

Classification and recognition are almost achieved continuously by most of us. For instance, reading this sentence would not be possible without this ability as it involves the recognition of the letters and words that compose it. Similarly, a simple look at the picture 5.24 may be sufficient to many pilots to recognize the targets below. For individuals less familiar with aeronautics, this may not be the case. Nevertheless, little *a priori* knowledge is needed to state that all these targets are aircraft and that T_1, T_2 and T_3 have a unique shape, whereas the targets T_4 to T_7 may have more common features since they are all jet-fighters with similar designs. For this reason, the rate of correct classification is expected to be higher for targets T_1 (DC-3), T_2 (F-117) and T_3 (F-14) than for the other targets.

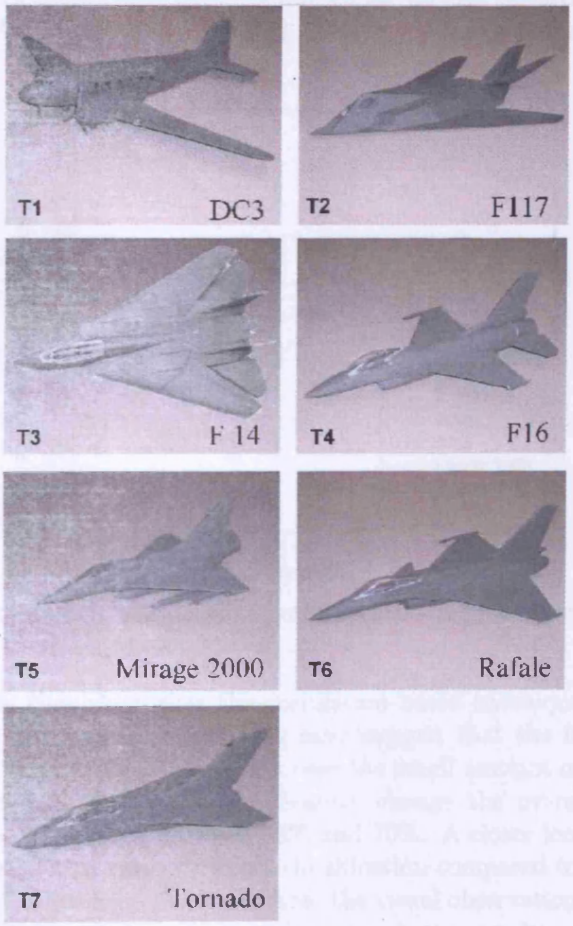

Figure 5.24: Scale-model targets used for classification

5.5.2 Performance

Classification techniques

In this section, the same set of radar data is applied to four different classification techniques in order to compare their performance. The techniques tested include correlation of regular range-profiles, correlation of range-profiles obtained from scattering-centre models, correlation of range-profiles obtained from extrapolated scattering-centre models, and the proposed matching algorithm using clustering approach in the z-plane (MAUCAZ).

Regular correlation

Several experiments have been conducted for various levels of added noise: $SNR = [10\ dB, 15\ dB, 20\ dB, 25\ dB]$. The results are represented in figure 5.25.

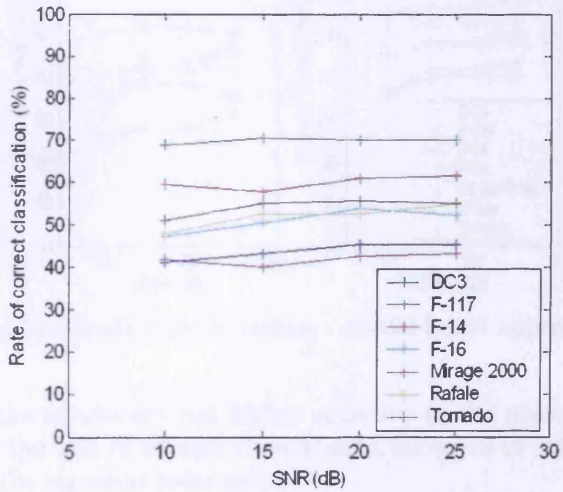

Figure 5.25: Classification performance - regular approach

The results here show that the correlation-based technique is relatively insensitive to the added noise. This may suggest that the initial SNR is actually smaller than 10dB, in which case the small amount of noise added for the experiment would not significantly change the overall SNR. The performance are bounded between 38% and 70%. A closer look shows that T_2 and T_3 have a high rate of correct classification compared to targets such as T_4 to T_7. This has been predicted from the visual observation of the target geometries. T_1 constitutes an exception since better results were expected as the Douglas DC3 is a propeller-driven transport-aircraft that has a very different shape than the other targets in the set.

Model-based correlation

The same experiment is conducted using the model-based approach described in 5.4. The scattering-centre models are extracted by using the following parameters: $L = 21$, $N = 128$, $P = 6$. Figure 5.26 represents the rate of correct classification obtained with range-profiles computed from the scattering-centre models obtained by Linear Least-Squares fit (left) and after ajdustment by Non-Linear Least-Squares fit (right) using the Gauss-Newton algorithm.

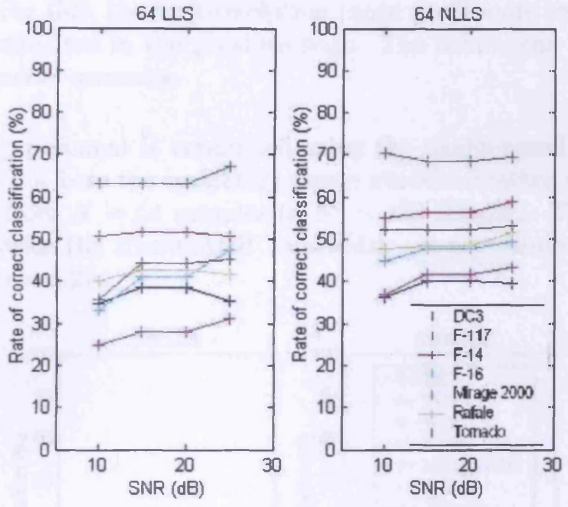

Figure 5.26: Classification performance - model-based approach ($N = 64$)

Globally the results are not highly sensitive to the noise, although for some targets, the rate of correct classification increases in rather large proportion with the signal-to-noise ratio.

The results obtained using the model ajusted by non-linear least-squares fitting are relatively better than those obtained directly using linear least-squares fitting. The performances are bounded within 25% to 70% in the first case, and within 35% to 70% in the second one. These figures are similar to those obtained with the direct signal, which shows the capability of the method to accurately reconstruct a signal.

For both techniques, the performance obtained with the various targets roughly follow the same order and are similar to the order obtained by using the direct signal. By decreasing performance, the targets can be sorted as follow: T2 (F-117), T3 (F-14), T7 (Tornado), T6 (Rafale), T4 (F-16), T1

(DC3) and T5 (Mirage 2000). For non-linear least-squares fit, the performance associated with the DC3 are the lowest, which is unexpected.

Extrapolated model-based correlation

According to classification theory, using a higher number of discriminating attributes should enhance the performance obtained with similar-looking targets. For radar measurements, a common solution consists of improving the range resolution by transmitting a larger bandwidth. Here, target classification is carried out using range-profiles enhanced by bandwidth extrapolation. For this, the high-resolution range profiles are computed using the models estimated in the previous page. The results can be seen as an indicator of model accuracy.

The same experiment is conducted using the model-based approach described in 5.4 but here the scattering-centre models obtained previously are extrapolated from $N = 64$ samples to $N' = 128$ samples. The results obtained with twice the transmitted bandwidth are represented in a similar manner in figure 5.27.

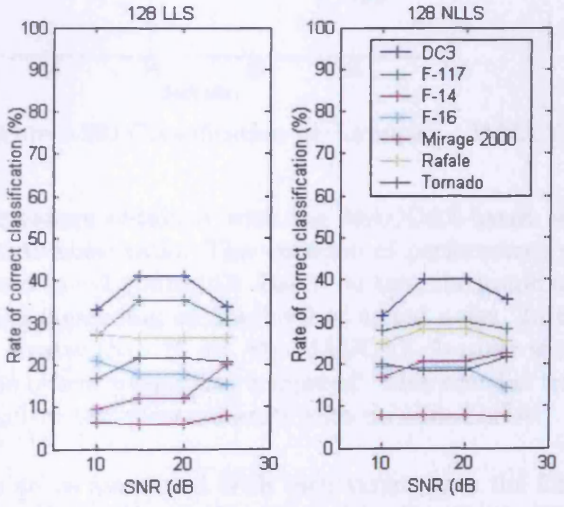

Figure 5.27: Classification performance - extrapolated model-based approach ($N = 128$)

The results obtained with linear and non-linear least-squares fits are both bounded within 5% to 40%. These figures, 30 points lower than any of those obtained with other correlation-based techniques, seem to confirm the incapability of the model to be accurately extrapolated.

Matching algorithm using clustering approach in the z-plane

The classification is now performed using the MAUCAZ algorithm. Here, the poles have been computed using the same parameters as in the previous section, $N = 64$, $L = 23$ and $P = 6$. The pre-processing stage selects the $P = 5$ poles that are the closest to the unit-circle. The number of clusters used for computing the distance is $K = 4$. The performance of the classifier can be summarised by figure 5.28.

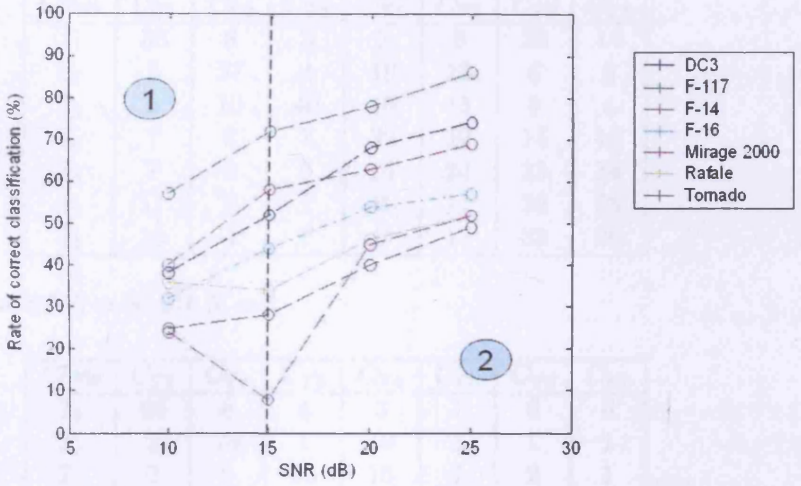

Figure 5.28: Classification performance - MAUCAZ

The performances obtained with the MAUCAZ-based technique vary with the signal-to-noise ratio. The variation of performance with the SNR can be estimated as +2 points/dB. Based on this, the graph can be divided into two regions depending on the level of added noise. In the region defined by SNR greater than 15 dB, the MAUCAZ classifier start performing better than the others techniques compared. This remains true even if the correlation involves test-measurements with no added noise.

The performances associated with each target have the following order: T2 (F-117), T1 (DC3), T3 (F-14), followed by T4 (F-16), T6 (Rafale), T5 (Mirage 2000), and T7 (Tornado). These two groups of targets are in perfect agreement with the order intuitively expected based on visual observations of the target geometry, which supports the idea that classification can be performed based on the location of the physical scattering-centres.

The classification has been carried out for various levels of added noise in order to estimate the susceptibility of the classifier. For $SNR = 30\ dB$, the rate of correct-classification associated with the F-117 reaches 90%.

In order to trace the sources of classification error, confusion matrices may be used. The following tables are the confusion matrices computed for three levels of noise. Each row corresponds to the real class, whereas each column corresponds to the estimated class.

- $SNR = 10\ dB\ K = 4$

Class	C_{T1}	C_{T2}	C_{T3}	C_{T4}	C_{T5}	C_{T6}	C_{T7}
T_1	38	8	3	5	8	20	14
T_2	5	57	4	10	12	6	3
T_3	3	10	40	16	15	8	4
T_4	7	6	7	32	19	15	10
T_5	7	6	8	15	24	23	14
T_6	11	7	1	6	11	36	25
T_7	10	4	7	5	12	33	25

- $SNR = 20\ dB\ K = 4$

Class	C_{T1}	C_{T2}	C_{T3}	C_{T4}	C_{T5}	C_{T6}	C_{T7}
T_1	68	8	4	3	1	6	6
T_2	2	78	1	10	3	1	1
T_3	2	6	63	16	7	2	1
T_4	2	3	15	54	14	5	2
T_5	10	7	13	12	45	7	3
T_6	6	2	5	10	13	46	16
T_7	5	5	3	3	7	34	40

- $SNR = 30\ dB\ K = 4$

Class	C_{T1}	C_{T2}	C_{T3}	C_{T4}	C_{T5}	C_{T6}	C_{T7}
T_1	71	14	4	3	2	2	3
T_2	2	90	2	3	1	0	0
T_3	2	5	69	16	5	0	0
T_4	0	7	18	58	10	4	0
T_5	1	6	11	14	59	4	2
T_6	3	5	2	6	13	43	25
T_7	3	9	5	5	7	23	44

5.5.3 Discussion

The results show that whereas the performance of the correlation-based classification technique obtained using the signals reconstructed with low-order models is similar to that obtained using the raw signals, the perfor-

mance obtained using the extrapolated models are much lower. It is especially poor for models whose parameters are adjusted by non-linear least-squares fitting.

By using the model parameters directly expressed in the z-plane, the classifier MAUCAZ is less sensitive to errors on the parameter-estimates than correlation-based techniques. This can be explained by the fact that the errors on the pole magnitude have a small influence on the function chosen to measure the distance between patterns. This may also be due to the reduction of the speckle effect. The sensitivity to the noise that is observed in figure 5.28 suggests that the model parameter-estimates are however sensitive to the noise.

Considering the apparent sensitivity of the MAUCAZ algorithm to the noise, the small variation of the performance of the correlation-based classification technique with increasing noise is relatively surprising. One reason for this may be that the initial SNR of the measured-signal used as a template, is actually relatively low (*i.e.* $SNR_0 < 15\ dB$). Let us remember that although unknown, the signal-to-noise ratio for the three metal spheres was estimated to be $SNR \approx 10.5\ dB$ in Chapter 4. In that case, the noise added to the test-signals would not have much effect on their total SNR.

The initial presence of strong noise may explain the robustness of the classification technique to the added noise. However, it would then be expected that the results obtained using MAUCAZ be relatively constant too. Instead, the MAUCAZ technique appears to be strongly sensitive to the noise. This may be explained by the fact that some of the clusters that were used for the classification are actually formed by poles that are different from those chosen for building the model. Additional experiments are needed to fully understand the nature of this problem.

5.6 Conclusion

In this section, four techniques for classification have been presented and compared using radar signals scattered by seven scale-model aircraft on a turntable. The techniques include correlation of direct signals, correlation of low-order models, correlation of the extrapolated low-order models, and the novel feature-based method called MAUCAZ.

The performance obtained with the model and the raw data are similar. This implies that the model can be a mathematically close representation of the modelled signal which contains the information used in the correlation-based classification. This subsequently confirms that the scattering-centre model can be efficiently used for data-compression. Nevertheless, the extrapolated models do not appear to be suitable representations that exhibit the information needed for correlation-based classification. This also confirms that the model is often not a complete and physically accurate representation of the target.

In comparison, the novel classification technique which is proposed here can perform better than the others providing the SNR is sufficiently high (*i.e.* 15 dB or higher). The classification performance shows that the technique makes better use of the information captured in the scattering model at a cost of relatively large computation. However, the computation time can be greatly reduced using parallel processing techniques and smart algorithms.

The fact that the classification technique relies on the cumulative probability that couples of poles, one in the test-patterns and another in the template-pattern, correspond to the same physical scatterers, opens the door to classification of targets that have a varying configuration. If the target is not perfectly rigid, the position of the poles may be affected. Moreover, if peripheral components such as missiles are added to the main body, they would modify the pattern of poles too. They may be strong scatterers which would generate new poles, hide other scatterers which would remove poles or modify the pattern of interaction between scatterers which would modify the pattern of poles and subsequently confuse the classifier.

It would be useful to examine the variation of the pattern of poles of an aircraft with varying configuration in order to identify the core-poles that are associated with physical scatterers on the stationary structure and the additional poles that are associated with scattering elements whose presence or position may vary on the target. It may also be useful to study the effect of rotation and translation of a real target on the composition of the clusters.

Chapter 6

CONCLUSION

6.1 Key point

In this thesis, the principle of bandwidth extrapolation for radar signals has been revisited and the technique proposed by Cuomo *et al.* investigated for the case of man-made targets. A strong motivation behind this work comes from the growing need for high-resolution images requiring wideband waveforms and the increasing use of the electromagnetic spectrum by the communication industry. The conclusion of this thesis is that the estimation of the model which relies on bandwidth extrapolation may not be sufficiently accurate to allow accurate signal prediction in all circumstances. The principal causes of error are the following:

1. the limited segment of a corrupted signal generally available does not allow reconstruction of the accurate information to form the complex model describing the scattering mechanims of the target alone, and

2. the scattering centre model is not sophisticated enough to describe the rather complicated scattering mechanisms that characterise man-made targets such as aircraft.

Whereas the second hypothesis has been recently investigated by Rihaczek [41] and Guerci [35], no real investigation has been carried out to support the first one. In that context, this thesis contributes improving the state of the art of processing techniques for high range-resolution radar.

6.2 Summary

This work started by reproducing an experiment found in the article written by Cuomo *et al.* [12] in which the authors propose to use a model computed using model-order estimators, super-resolution and least-squares model-fitting algorithms for predicting the radar signal outside the modelling band and subsequently improving the image resolution. The technique used to model the radar signal has been implemented and tested using simulated and real scatterers. Relying on the quadratic-error as an indicator of accuracy, the experiments reveal that although the determination of the model-order and the selection of the true poles remain an issue, the signal-to-residue ratio of the reconstructed signal is relatively good and improves with the model-order. This supports the suitability of the technique for data compression.

In detail, the experiment shows that although the Matrix-Pencil algorithm may present better results with very simple point-scatterers, the modified root-MUSIC algorithm [4] seems to be a more robust algorithm. This shows the limitation of the technique when employed for modelling complex targets. The comparison of the least-squares techniques reveals that the non-linear least-squares algorithm (Gauss-Newton) very often provides the model with smallest SRR and that, when it does not, the model is so obviously incorrect that it is not difficult to notice the error. This is not always the case for the linear least-squares technique as wrong models may be difficult to spot.

By using data supplied by an independent source (Dr Victor Chen - Naval Research Laboratory - USA), the potential of this algorithm for radar imaging is demonstrated further. However, attempts to predict the radar signal for a real Boeing 727 failed. Based on the theoretical framework proposed in Chapter 3, it is proposed as an explanation that the estimated model is not a physically accurate representation of the scattering mechanisms that characterise this aircraft. This result constitutes a basis for challenging the capability of the algorithm to perform with complex targets such as aircraft. Additional reasons making the algorithm unsuitable to bandwidth extrapolation are then identified through a sensitivity analysis of the technique.

Firstly, this work has clearly revealed that errors may not be detected by using the quadratic-error. The latter does not appear to be a valid indicator of model accuracy. Secondly, such type of errors may typically happen when the model-order is wrongly estimated, when the target exhibits scattering behaviours that are more complex than a set of independent spheres, or when the bandwidth or the signal-to-noise ratio is so low that the model

parameters cannot be accurately estimated. In these cases, the contribution of the target to the signal cannot be properly captured in the model.

The examination of this hypothesis is then investigated using simulated and real measurements. In order to limit the field of this work to the sole task of verifying that the deficiency of the model imposed by the relative poor quality of the received signal may be responsible for incorrect modelling, the technique is tested using a target composed of three spheres in the anechoic chamber of ENSIETA. These highly controlled conditions ensure that poor results would not be due to target complexity, target motion, or clutter. The results proved that, even when using such simple targets, the extrapolation technique is limited by the initial resolution, which is therefore highly dependent upon the spatial distribution of the scatterers, the noise and the bandwidth.

Both simulated and real measurements show that when it is not possible to retrieve the model-parameters from the signal, the technique generates an approximated model whose accuracy cannot be determined from the quadratic error. Due to the method itself, we know that the value of the parameter-estimates is driven by the minimisation of the quadratic-error across the sole modelling band. Because this does not necessarily yield models that are accurate on other parts of the spectrum, the capability to accurately extrapolate or interpolate a model across a wide bandwidth cannot be pre-determined based on the quadratic-error computed across the modelling band.

Considering the sensitivity of the model to errors on the pole-magnitude, the forward extrapolation in the frequency domain of a poorly accurate model, is characterised by large amplitude excursions. Alternatively the interpolation of the model can be seen as a safer option as this instability is prevented by the fact that the signal is also fitted in the sub-band at high frequencies. However, this does not provide a more accurate model. On the contrary, the separation of a large band into two sub-bands of half-the-bandwidth each reduces by half the maximum model-order allowed.

A different attempt to show that the extrapolation of the model does not necessarily provide improved information that could enhance non-cooperative target classification techniques has been performed by comparing the classification results obtained for various signals including raw signals, models and extrapolated models using real turntable-measurements of seven scale-model aircraft in the same anechoic chamber. First, the results have shown that raw data and models provide similar results, which again supports the suitability of the technique for data compression. Second, the classification

results obtained with the extrapolated model are very poor, especially those computed using non-linear least-squares. This confirms that the model estimated is often deficient or badly estimated and cannot be always used for radar applications such as imaging or classification.

In order to enhance the high-resolution range-profile based classification technique, a novel method has been proposed. It is based on limited but reliable information that can be extracted from the signal, and does not suffer from the hyper-sentitivity to the pole-magnitude. To meet such requirements, a feature-based approach has been chosen and the parameter-estimates that may be incorrectly estimated to compensate for incorrect estimation of others have been discarded. The resulting method achieve target classification based on the information contained in the pole-estimates only. Similarly, to avoid the risk of incorrect pole-selection, the technique is not based on criteria such as closeness to the unit circle. Instead, pole-selection is performed based on *a priori* information using the likelihood that a set of poles from the test pattern describes the same physical features as another one in a pattern in the library.

The technique created is called a Matching Algorithm Using Clustering Approach in the Z-plane (MAUCAZ). The results obtained using this technique are very promising, especially for high signal-to-noise ratio, typically greater than 25 dB. It is shown that the representation in the z-plane provides various advantages and that the comparison of the signatures is less sensitive to variation, for example, of aspect-angle. It is currently being investigated for SONAR applications.

6.3 Future work

This thesis like most research works has probably opened more questions than it has solved. For the continuation of this work, three principal directions can be pursued. The first one concerns the modelling technique and the understanding of its limits, the second one concerns the development of a more complex model, and the third one concerns the potential use of the MAUCAZ algorithm for target classification.

The modelling technique has proved to be a relatively good extractor of features. This thesis has demonstrated that the limited segment of corrupted signal generally available may not allow reconstruction of the complete information needed to form an accurate model describing the scattering mechanims of the target. It would be useful to investigate further the limits of the technique in order to determine whether it is possible to improve the extraction of a greater number of features.

As important as the above would be the migration from the scattering-centre model towards a more sophisticated model. A model that could capture the complex scattering mechanisms characterising man-made targets such as aircrafts would certainly contribute to enhance classification performance. In that aim, it would be appropriate to test the algorithm using simple-geometry objects such as cylinders, plates and trihedrals and to observe how the interactions between them may affect the current model.

Finally, the proposed MAUCAZ algorithm could be developed further and employed with burried targets. Because of the relatively simple geometry of land-mines, it may be possible to detect the principal scattering-centres and distinguish them from large stones. Assuming that the separation of the clutter from the actual target is possible, the joint use of the Scattering-centre extraction algorithm and the MAUCAZ algorithm would probably provide excellents results.

Bibliography

[1] T. M. Aiello. *SAR Imagery http://www.sandia.gov/RADAR/imagery.html.* Sandia National Laboratory, Albuquerque, NM, US, 1995.

[2] SIRPA AIR. *http://defense.gouv.fr/air.* Ministère Francais de la défense, Paris, France, 2003.

[3] J.T. Ascroft. *Project AY4490 - A study into techniques for improving radar spectrum utilisation.* Ofcom, 2004.

[4] A. Barabell. Improving the resolution performance of eigenstructure-based direction-finding algorithms. In *ASSP-83 Proc.*, volume 8, pages 336–339, 1983.

[5] G. Bienvenu. Influence of the spatial coherence of the background noise on high resolution passive methods. In *ASSP-79 Proc.*, volume 4, pages 306–309, 1979.

[6] B. Borden. *Radar Imaging of Airborne Targets.* Institute of Physics, London, 1999.

[7] H. Borrion, H. Griffiths, P. Tait, D. Money, and C. Baker. One-dimensional model-based approach for isar imaging. In *Geoscience and Remote Sensing Symposium 2005, IGARSS-2005 Proc.*, volume 1, 2005.

[8] H. Borrion, H. Griffiths, P. Tait, D. Money, and C. Baker. Scattering centre extraction for extended targets. In *Radar 2005, IEEE Int. Conf.*, pages 173–178, 2005.

[9] H. Borrion, H. Griffiths, P. Tait, D. Money, and C. Baker. One-dimensional model-based approach for isar imaging (2). In *Geoscience and Remote Sensing Symposium 2006, IGARSS-2006 Proc.*, volume 1, 2006.

[10] R. Carriere and R. L. Moses. Autoregressive moving average modeling of radar target signature. In *Radar Conference 1988,IEEE Proc.*, pages 225–229, 1988.

[11] V. C. Chen. *http://airborne.nrl.navy.mil/ vchen.* U.S. Naval Research Laboratory, Washington DC, SW, US, 2003.

[12] K. M. Cuomo, J. E. Piou, and J. T. Mayhan. Ultra-wideband coherent processing. *Lincoln Laboratory Journal*, 10(2):203–222, 1997.

[13] R. de Prony. Essai expérimental et analytique sur les lois de la dilatabilité des fluides élastiques et sur celles de la force expansive de la vapeur de l'eau et de la vapeur de l'alkool, à différentes températures. *J. de l'Ecole Polytechnique*, 1:24–76, 1795.

[14] W. F. Gabriel. Improved range superresolution via bandwidth extrapolation. In *Radar Conference 1993,IEEE Proc.*, pages 123–127, 1993.

[15] H. Gernsback. *Ralph 124c 41+.* Modern Electrics, 1911.

[16] R. Van Der Heinden. *Aircraft Recognition with Radar Range Profiles.* Thesis, University Van Amsterdam - WINS, The Netherlands, 1998.

[17] Y. Hua and T. K. Sarkar. Matrix pencil method for estimating parameters of exponentially damped/undamped sinusoids in noise. *Acoustics, Speech, and Signal Processing, IEEE Trans.*, 38(5):814–824, 1990.

[18] Y. Hua and T. K. Sarkar. On SVD for estimating generalized eigenvalues of singular matrix pencil in noise. *Circuits and Systems, 1991., IEEE International Symposium on*, 5:2780–2783, 1991.

[19] D. Hudson and S. Psaltis. Correlation filters for aircraft identification from radar range profiles. *Aerospace and Electronic System, IEEE Trans.*, 29(3):741–748, 1993.

[20] M.G.M. Hussain and Y.A. Safar. Pole patterns of radar-target scattering model based on ultra-wideband gaussian pulses. In *Radar 2001, IEEE Int. Conf.*, pages 483–487, 2001.

[21] M. R. Inggs, M. W.Van Zyl, and A. Knight. A simulation of synthetic range profile radar. In *COMSIG'92, Proc*, pages 1–16, 1992.

[22] S. M. Kay. *Modern spectral estimation: theory and application.* Prentice-Hall, Englewood Cliffs, NJ 07632, 1988.

[23] E. F. Knott, J. F. Shaeffer, and M. T. Tuley. *Radar Cross Section.* Artech House, 685 Canton Street Norwood MA 02062, 1993.

[24] A. C. Kot, S. Parthasarathy, D. W. Tufts, and R. J. Vaccaro. The statistical performance method of state-variable balancing and prony's method in parameter estimation. In *ICASSP-89, IEEE*, volume 4, pages 2286–2289, 1989.

[25] S. Y. Kung, K. S. Arun, and D. V. Bhaskar Rao. State-space and singular-value decomposition-based approximation methods for the harmonic retrival problem. *J. Opt. Soc. Am.*, 73(12):1799–1811, 1983.

[26] S. Lang and J. McClellan. Frequency estimation with maximum entropy spectral estimators. *ASSP, IEEE Trans.*, 28(6):716–724, 1980.

[27] R. Lengenfelder and M. R. Inggs. Extended database of synthetic range profiles of commercial aircraft. In *COMSIG'97, Proc.*, pages 81–82, 1997.

[28] H.-J. Li. and S.-H. Yang. Using range profiles as feature vectors to identify aerospace objects. *Antennas and Propagation, IEEE Trans.*, 41(3):261–268, 1993.

[29] L. Mandel. Interpretation of instantaneous frequencies. *Am. J. Phys.*, 42(6):840, 1974.

[30] X. Mengdao and B. Zheng. The properties of range profile of aircraft. In *Radar Conference 2001,CIE Proc.*, pages 1050–1054, 2001.

[31] G. J. Meyer. *Classification of Radar Targets Using Invariant Features.* Air Force Institute of Techology, 2003.

[32] T. G. Moore, B. W.Zuerndorfer, and E. C Burt. Enhanced imagery using spectral-estimation-based techniques. *Lincoln Laboratory Journal*, 10(2):171–183, 1997.

[33] C. Nieuwoudt and E. C. Botha. Relative performance of correlation based and feature-based classifier of aircraft using radar range profiles. In *Pattern Recognition, 1998 Proc., 14th Int. Conf.*, volume 2, pages 1828–1832, 1998.

[34] A. Paulraj, R. Roy, and T. Kailath. Estimation of signal parameters via rotational invariance techniques- esprit. In *Circuits, Systems and Computers, 19th Asilomar Conf.*, volume 8, pages 83–89, 1985.

[35] S. U. Pillai, H. S. Oh, D. C. Youla, and J. R. Guerci. Optimal transmit-receiver design in the presence of signal-dependent interference and channel noise. *Information Theory, IEEE Trans.*, 46(2):577 – 584, 2000.

[36] L. C. Potter, D.-M. Chiang, R.Carriere, and M. J.Gerry. A gtd-based parametric model for radar scattering. *Antennas and Propagation, IEEE Trans.*, 43(10):1058–1067, 1995.

[37] L. C. Potter and R. L. Moses. Attributed scattering centers for sar atr. *Image Processing, IEEE Trans.*, 6(1):79–91, 1997.

[38] A. Quinquis, E. Radoi, and F.-C. Totir. Some radar imagery results using superresolution techniques. *Antennas and Propagation, IEEE Trans.*, 52(5):1230–1244, 2004.

[39] M. A. Rahman and K.-B. Yu. Total least squares approach for frequency estimation using linear prediction. *ASSP, IEEE Trans.*, 35(10):1440–1454, 1987.

[40] Q. S. Ren and A. J. Willis. Fast root music algorithm. *Electronics. Letters*, 33(6):450–451, 1997.

[41] A. W. Rihaczek and S. J. Hershkowitz. Man-made target backscattering behaviour: Application of conventional radar resolution theory. *Aerospace and Electronic System, IEEE Trans.*, 32(2):809–824, 1996.

[42] J. Rissanen. Modelling by the shortest data description. *Automatica*, 14:465–471, 1978.

[43] G.F. Ross. A time domain criterion for the design of wideband radiating elements. *Antennas and Propagation, IEEE Trans.*, 16(3):355, 1968.

[44] T. K. Sarkar and O. Pereira. Using the matrix pencil method to estimate the parameters of a sum of complex exponentials. *Antennas and Propagation Magazine, IEEE*, 37(1):48–55, 1995.

[45] R. Schmidt. Multiple emitter location and signal parameter estimation. *Antennas and Propagation, IEEE Trans.*, 34(3):276–280, 1986.

[46] M. I. Skolnik. *Radar Handbook.* Artech House, 685 Canton Street Norwood MA 02062, 1993.

[47] K. Suwa and M. Iwamoto. A bandwidth extrapolation technique for polarimetric radar data and a recursive method for polarimetric linear prediction coefficient estimation. In *Geoscience and Remote Sensing Symposium 2003, IGARSS-2003 Proc.*, volume 1, 2003.

[48] S. Swords. *Technical history of the beginnings of RADAR.* IEE, 1986.

[49] D. W. Tufts and R. Kumaresan. Estimating the frequencies of multiple sinusoids: making linear prediction perform like maximum likelihood. *Proc. IEEE*, 70(9):975–989, 1982.

[50] M. Wax and T. Kailath. Detection of signals by information theoretic criteria. *ASSP, IEEE Trans.*, 33:387–392, 1985.

[51] A. Webb. *Statistical Pattern Recognition.* Arnold, 338 Euston Road, NW13BH London, 1999.

[52] R. D. Wehner. *High Resolution Radar.* Artech House, 685 Canton Street Norwood MA 02062, 1994.

[53] A. J. Wilkinson, R. T. Lord, and M. R. Inggs. Stepped frequency processing by reconstruction of target reflectivity spectrum. In *COMSIG'98, Proc.*, pages 101–104, 1998.

[54] Z. Xun, Z. Zhaowen, and Guo Guirong. Hrr target recognition using the geometry information of scattering centers. In *National Aerospace and Electronics Conf. 97, IEEE Proc.*, volume 2, pages 936–940, 1997.

[55] R. Zwart. *Aircraft Recognition with Radar Range Profiles.* Thesis, University Van Amsterdam - WINS, The Netherlands, 1998.

[56] A. Zyweck and R.E. Bogner. Radar target recognition using range profiles. In *ICASSP-94, IEEE*, volume 2, pages 373–376, 1994.